Fabrication and TCAD Simulation of TiO_2 / ZnO Nanorods Electron Transport Layer based $CH_3NH_3PbI_3$ Perovskite Solar Cell

Thesis submitted in partial fulfillment for the Award of Degree

Doctor of Philosophy

By

Deepak Kumar Jarwal

DEPARTMENT OF ELECTRONICS ENGINEERING
INDIAN INSTITUTE OF TECHNOLOGY
(BANARAS HINDU UNIVERSITY)
VARANASI – 221005
INDIA

ROLL NO: 15091004 **2021**

CERTIFICATE

It is certified that the work contained in the thesis titled **“Fabrication and TCAD Simulation of TiO_2 / ZnO Nanorods Electron Transport Layer based $CH_3NH_3PbI_3$ Perovskite Solar Cell”** by **“Deepak Kumar Jarwal”** has been carried out under our supervision and that this work has not been submitted elsewhere for a degree.

It is further certified that the student has fulfilled all the requirements of Comprehensive, Candidacy and SOTA for the award of Ph. D. Degree.

(Prof. S. Jit)
Supervisor
Department of Electronics Engineering
IIT (BHU), Varanasi

Bratindranath
Mukherjee

(Dr. Bratindranath Mukherjee)
Co-Supervisor
Department of Metallurgical Engineering
IIT (BHU), Varanasi

DECLARATION BY THE CANDIDATE

I, Deepak Kumar Jarwal, certify that the work embodied in this thesis is my own bonafide work and carried out by me under the supervision of Prof. Satyabrata Jit and Dr. Bratindranath Mukherjee from "21/07/2015" to “27/01/2021”, at the Department of Electronics Engineering, Indian Institute of Technology (BHU), Varanasi. The matter embodied in this thesis has not been submitted for the award of any other degree/diploma. I declare that I have faithfully acknowledged and given credits to the research workers wherever their works have been cited in my work in this thesis. I further declare that I have not will fully copied any other's work, paragraphs, text, data, results, *etc*., reported in journals, books, magazines, reports, dissertations, theses, *etc*., or available at websites and have not included them in this thesis and have not cited as my own work.

Deepak

Date: 27/01/2021 **Signature of the Student**
Place: Varanasi **Deepak Kumar Jarwal**

CERTIFICATE BY THE SUPERVISOR

It is certified that the above statement made by the student is correct to the best of my knowledge.

Bratindranath Mukherjee

(Prof. S. Jit)
Supervisor
Department of Electronics Engineering
IIT (BHU), Varanasi

(Dr. Bratindranath Mukherjee)
Co-Supervisor
Department of Metallurgical Engineering
IIT (BHU), Varanasi

Signature of Head of Department
"SEAL OF THE DEPARTMENT"

COPYRIGHT TRANSFER CERTIFICATE

Title of the Thesis: **Fabrication and TCAD Simulation of TiO_2 / ZnO Nanorods Electron Transport Layer based $CH_3NH_3PbI_3$ Perovskite Solar Cell**

Name of the Student: **Deepak Kumar Jarwal**

Copyright Transfer

The undersigned hereby assigns to the Indian Institute of Technology (Banaras Hindu University), Varanasi all rights under copyright that may exist in and for the above thesis submitted for the award of the Doctor of Philosophy.

Deepak

Date: 27/01/2021 **Signature of the Student**

Place: Varanasi **Deepak Kumar Jarwal**

Note: However, the author may reproduce or authorize others to reproduce material extracted verbatim from the thesis or derivative of the thesis for author's personal use provided that the source and the Institute's copyright notice are indicated.

ACKNOWLEDGEMENT

First and foremost, I want to dedicate my honest prayer to Pujya Gurudev who has given me the strength, knowledge, ability and opportunity to undertake this research study and to complete it satisfactorily. I am humbled and exceedingly joyful as a witness to his countless blessings.

First of all, I would like to express my immense gratitude and sincere thanks to my supervisor Prof. Satyabrata Jit and Co-supervisor Dr. Bratindranath Mukherjee for their continuous support, motivation and valuable guidance. Their immense knowledge and guidance helped me a lot to carry out my research work. Without their precious and whole hearted support the successful completion of this research work would have not been possible. The insightful discussions with them always provided me great enthusiasm.

I wish to extend my sincere gratitude towards my research programme committee (RPC) members Prof. V. N. Mishra, Dr. Bholanath Pal, and all the Departmental Research Committee (DRC) members for their valuable suggestions and fruitful discussions during the entire period of my research. A vote of thanks from the bottom of my heart goes to the Head of Electronics Engineering Department, IIT (BHU), Varanasi for providing me all of the necessary tools and lab facilities to conduct my research work. I would also like to thank all the faculty members, laboratory staff, librarians and office staff for their kind cooperation and encouragement during this journey.

My thanks and deep appreciations also go to all staff members of CRME lab, Department of Electronics Engineering, especially to Mr. M. K. Saxena, Mr. S. C. Yadav, Mr. Sanjeev Srivastava, Mr. Shyam Narayan, and Mr. Vinay Srivastava for their kind co-operation.

I would like to express my special thanks to my seniors Dr. Gopal Rwat, Dr. Hemant Kumar Bhatt, Dr. Yogesh Kumar, Dr. Chandan Kumar, Dr. Kunal Singh, Dr. Sanjay Kumar, Dr. Balraj Singh, Dr. Sweta Chander, Dr. Ekta Goyal, Mr. Lalit Chandra, Mr. P. K. Sahu, Dr. Subhiman Chatterjee, Dr. Gaorav Modanwal for their constant encouragement and suggestions.

I have great pleasure in acknowledging my colleagues and fellow Mr. Kamlaksha Baral, Mr. Ashwini Kumar Mishra, Mr. Amit Kumar, Mr. Smriti Ratan, Mr. Prince Kumar Singh, Mr. Rishibrind Upadyay, Mr. Abhinav Pratap Singh, Mr. Deepchand Upadyay, Mr. Abhisekh Kumar, Mr. Ashutosh Dixit, Mr. Jogendra Singh Rana, Mrs Sikha Singh for their motivation, support, and encouragement. I wish to extend my special thanks to all of them for providing a nice, friendly and peaceful research environment.

I am very much thankful to many research scholars Mr. Prabhakar Tripathy, Mr.Akash Prajapati, Mr. Vinit Singh, Mr. Mumtaj Ali Ansari, Mr. Aman Sikri, Mr. Rahul Pal, and Mr. Arjun Yadav for their fruitful suggestions.

My thanks and sincere appreciations also go to my friend, especially to Mr. Sunil Kumar, Mr. Amit Kumar Soni, Mr. Kaushal Kishor Gupta and Mr. Yash Sukla for their constant support.

I would like to express my heart-felt gratitude to my beloved parents Shri. Ramswaroop Jangid and Smt. Shushila Devi for their constant support and love throughout my life. I am always indebted to my grandparents for their eternal blessings.

At this very special moment, however no words will be enough but I heartily express sincere thanks to my sisters Mrs. Archana Jangir and Dr. Nisha Jarwal. They are the source of moral and emotional strength in my life. I have a sincere appreciation for my sister in law Mrs. Anjali Baberwal for giving us sparkles like Aayush Jarwal and Aayan Jarwal.

My most profound appreciation towards my brothers Mr. Arvind Jarwal and Mr. Vikash Jarwal for their continuous support and encouragement. They are the source of strength and remain an invaluable asset to me.

It is a privilege to express my sincere regards and love for my fiancé Miss Deepika Jangid for her constant support, unconditional love, faith, and encouragement.

Finally, I heartily express sincere thanks to my Jarwal family and especially to Mr. Jitendra Kumar Jangir for their extreme patience and constant support over the years. They provided me strength and confidence to attain this task.

Above all, I thank Lord Vishwanath for providing me strength and courage in completing the work.

Deepak

Date: 27/01/2021 ***(Deepak Kumar Jarwal)***

DEDICATED TO MY
BELOVED
PUJYA GURUDEV

CONTENTS

LIST OF FIGURES

LIST OF TABLES

LIST OF ABBREVIATIONS

Abbreviation	**Details**
PV	Photovoltaic
LED	Light Emitting Diode
P3HT	Poly(3-hexylthiophene)
HOMO	Highest Occupied Molecular Orbital
LUMO	Lowest Unoccupied Molecular Orbital
PEDOT	Poly(3,4-ethylenedioxythiophene)
PCE	Power Conversion Efficiency
AM	Atmospheric Mass
SPM	Scanning Probe Microscopy
AFM	Atomic Force Microscopy
STM	Scanning Tunnelling Microscopy
GaAs	Gallium Arsenide
HRSEM	High Resolution Scanning electron microscopy
EDX or EDS	Energy dispersive X-ray spectroscopy
TEM	Transmission Electron Microscopy
SAED	Selected Area Electron Diffraction
XRD	X-ray Diffraction
CIGS	Copper Indium Gallium Selenide
UV-Vis	Ultraviolet-Visible
PL	Photoluminescence
ZnO	Zinc Oxide
PET	Polyethylene Terephthalate
CdTe	Cadmium Telluride
CdS	Cadmium Sulphide
TiO_2	Titanium dioxide

Au	Gold
Ag	Silver
Al	Aluminum
MoO_3	Molybdenum Trioxide
RMS	Root Mean Square
ITO	Indium-Doped Tin Oxide
FTO	Fluorine Doped Tin Oxide
TCAD	Technology Computer Aided Design
EPBT	Energy Pay Back Time
PCBM	[6,6]-phenyl C_{61} butyric acid methyl ester
QDs	Quantum Dots
DSSCs	Dyed Sensitized Solar Cells
PSC	Perovskite Solar Cell
ETLs	Electron Transport Layers
HTLs	Hole Transport Layers
$MAPbX_3$	Methyl Ammonium Lead Halides
$CsPbX_3$	Caesium based Lead Halides (Cl, Br, I)
VB	Valence Band
CB	Conduction Band
Pb	Lead
eV	Electron Volt
PTAA	Poly(triaryl amine)
TCO	Transparent Conducting Oxide
FF	Fill Factor
SRH	Shockley Read Hall
PVD	Physical Vapour Deposition
DMF	Di-Methyl Formamide
DMSO	Di-Methyl Sulfoxide

GBL	g-Butyro- Lactone
NMP	N-Methyl-2-Pyrrolidone
Al_2O_3	Aluminium Oxide
PECVD	Plasma Enhanced Chemical Vapor Deposition
CBD	Chemical Bath Deposition
AC	Alternating Current
P3HT	Poly(3-Hexylthiophene)
CuSCN	Copper(I) thiocyanate
HTM	Hole Transport Material
ETM	Electron Transport Material
ZNRs	ZnO Nanorods
C_{60}	Fullerenes
PCBM	Phenyl-C61-butyric acid methyl ester
TNRs	TiO_2 Nanorods
ZrO_2	Zirconium dioxide
SnO_2	Tin(IV) oxide
ALD	Atomic Layer Deposition
$TiCl_4$	Titanium Tetrachloride
TTIP	Titanium Iso-propoxide
HI	Hydrogen Iodide
RPM	Rotation Per Minute
DOS	Density of State

LIST OF SYMBOLS

Symbol	**Details**
λ	Wavelength
θ	Diffraction angle
T	Transmittance
A	Absorbance
I-V	Current-voltage
CV	Capacitance-voltage
μ_e	Electron mobility
μ_h	Hole mobility
V_T	Thermal voltage
I_{SH}	Current through Shunt resistance
I_{PH}	Photo generated current
I	Current
I_S	Reverse Saturation Current
B	Ratio of photo-generated current to the light intensity
N_t	Defect Density
N_A	Doping concentration of Acceptor
$\mathrm{N_D}$	Doping concentration of Donor
P	Power Density
R_S	Series Resistance
E_G	Energy Band Gap
R_{SH}	Shunt Resistance
FF	Fill Factor

J_{SC}	Short Circuit Current density
η	Power Conversion Efficiency
J	Current Density
V	Voltage
X	Electron Affinity
N_C	Density of states of the Conduction Band
N_V	Density of states of the Valence Band
$h\upsilon$	Photon Energy
P_T	Theoretical Power
I_{sc}	Short Circuit Current
P_{in}	Incident Optical Power Density
P_{mpp}	Maximum Power Density
J_{mpp}	Maximum Current Density
V_{mpp}	Maximum Voltage
V_{OC}	Open Circuit Voltage
n	Concentration of Electrons
p	Concentration of Holes
R	Recombination Rate
G	Generation Rate
γ	Recombination Coefficient
n_i	Intrinsic Carrier Concentration
R_{SRH}	Rate of SRH combination
V	Voltage
τn	Electron Lifetime
τp	Hole Lifetime
E_C	Energy of Conduction band
E_V	Energy of valence band

keV	Kilo Electron Volt
C	Capacitance
C_p^A	Constant
C_n^A	Constant
V	Voltage
ε_o	Vacuum Permittivity
ε_r	Relative Permittivity
$\Phi(x)$	Electrostatic Potential
e	Electric Charge
J_n	Current Density due to Electrons
J_p	Current Density due to Holes
ρ_d	Defect Charge Density

PREFACE

The worldwide increase in energy consumption has motivated scientists to explore the potential of solar energy. At present, solar energy harvesting is carried out mostly (more than 90%) by the inorganic crystalline silicon (Si) solar cells. Moreover, Si-based solar cells are now approaching their maximum theoretical limiting efficiency of ~29.43%. The latest advancements in technology and materials have led to the development of novel photosensitive materials that enabled the fabrication of low cost and highly efficient photovoltaic devices. The state of the art growth in various perovskite materials like inorganic ($CsPbX_3$: X=I, Cl, Br) and hybrid (ABX_3; A= organic compound, B= inorganic compound, and X= halides) have attracted huge interest among the researchers. Recently, methylammonium lead halides ($CH_3NH_3PbX_3$) have shown highly encouraging photosensitive for photovoltaic application, which gained immense research attention since its discovery and has boosted hopes for new photovoltaic technologies.

Typically, the optical and electrical characteristics of photovoltaic devices depend upon the device design, fabrication procedures, semiconductor/active material, etc. The different synthesis and deposition techniques may be used for the tuning of the electronic and optical properties of as-grown thin films. Additionally, the low-dimension nanostructures such as nanorods or nanowires that offer large surface-to-volume ratios are mostly used for the charge transport layer in perovskite solar cells (PSC). From this perspective, the present thesis deals with the TCAD simulation, fabrication, and characterization of TiO_2/ZnO nanorods electron transport layer (ETL) based hybrid perovskite ($CH_3NH_3PbI_3$) solar cells. In PSCs' design, the PTAA/Spiro-OMeTAD polymer is employed as hole transport material where small molecule materials (Li-TFSI and TBP) are used as doping elements to enhance the conductivity of the hole transport layer (HTL).

The primary focus of this thesis is to explore the performance parameter of PSC by means of the synergic effects of the modified synthesis process for ETL through optimized doping in HTL. The uniformly distributed and vertically aligned TiO_2/ZnO Nanorods have been grown on FTO substrates by the hydrothermal method, whereas both HTL and absorber layers are deposited via spin-coating techniques. Later, the optical and electrical properties of TiO_2/ZnO Nanorods have been explored in detail. The thesis consists of six chapters, which are briefly outlined as follows:

Chapter-1 introduces the hybrid perovskite material's optoelectronic properties, thin-film synthesis process, and the working principle of perovskite solar cells. A brief introduction about device models and thin film characterization techniques have been discussed. Finally, a detailed literature survey, motivation, and scope of the thesis have been presented.

Chapter-2 presents TCAD simulation and fabrication of hybrid perovskite solar cells. The electrical and optical characterization has been investigated for the device structure Pd/PTAA/hybrid perovskite ($CH_3NH_3PbI_3$)/TiO_2 Nanorods (TNRs) grown on an FTO coated glass substrate. The TNRs layer is synthesized by a low-cost hydrothermal process and acts as the ETL, whereas the PTAA acts as the HTL. The solar cells are optimized, fabricated, and characterized for different TNRs thickness and then several device performance parameters such as short circuit current density (J_{SC}), open-circuit voltage (V_{OC}), fill factor (*FF*), and power conversion efficiency (*PCE*) and etc. are studied. The *Solar Cell Capacitance Simulator-One Dimensional* (SCAPS-1D) is used to simulate the proposed solar cell structure and validated via our experimental results. The effects of thickness variation of ETL on the solar cell parameters have been investigated by solving the drift-diffusion model. The measurements show that the efficiency of the solar cell is decreased with the increase in ETL thickness, which is attributed to higher trap sites in the active layer and ETL. The maximum optimized efficiency of 15.04% is obtained for ETL thickness of 500 nm. On the other hand, the simulated results are in close resemblance to the experimental results, having an efficiency of 15.69%.

Chapter-3 reports the efficiency improvement of perovskite solar cells (PSCs) by solvothermal etching and $TiCl_4$ treatment of TNRs based ETL. The TiO_2 NRAs have been explored for the ETL due to their better direct carrier transportation over other TiO_2 nanostructures. The solvothermal etching of TiO_2 NRAs enhances the surface-to-volume ratio of the ETL, which, in turn, enhances the power conversion efficiency (PCE) of the PSCs. All the measurements have been performed at room temperature and high humid (with ~65% humidity) conditions to demonstrate the performance of the PSCs under normal environmental conditions. A noteworthy efficiency of 15.16% with an improved fill factor (FF) and short circuit current density (J_{SC}) has been reported in the proposed PSCs. The PSC performance is further improved by the $TiCl_4$ treatment of the solvothermally etched TiO_2 NRs as the ETL in the device.

Chapter-4 discusses the effect of the seed layer, which directly affects the growth of the ZnO Nanorods (ZNRs) and related photovoltaic parameters of the hybrid perovskite solar cell. Four different types of ZnO seed layer samples have been synthesized using four methods, namely: ZnO drop-cast, ZnO nanoparticles (NPs), ZnO quantum dots (QDs), and ZnO solvothermal on the FTO substrate. ZnO drop-cast results in less density, tilted, and non-uniform deposition of the nanorods. But uniform coverage, high volume to the surface, and vertical direction growth of ZNRs are observed in the ZnO QD seed layer sample compared to the other three samples. Morphology and crystalline structure were analyzed with HRSEM, TEM, and XRD, whereas optical absorption, emission, and transmittance are recorded using UV-Visible, and Photoluminescence, respectively. Subsequently, the electrical characterization reveals that the optimum photovoltaic parameters are obtained on the seed layer of ZnO QD, which leads to the power conversion efficiency of 10.69% for ZnO NR based perovskite solar cell structure (FTO/ZNRS/$CH_3NH_3PbI_3$/PTAA/Au).

Chapter-5 presents the simulation, fabrication, and characterization of ZnO Nanorod (ZNRs) based PSCs under ambient air conditions. The proposed PSC structures use a $CH_3NH_3PbI_3$ hybrid perovskite-based active layer sandwiched between a ZnO Nanorods (NRs) ETL and a Spiro-OMeTAD (undoped and doped) HTL. The ZnO NRs are grown using a low-cost solvothermal process at relatively low temperature. The performance of fabricated PSCs is analyzed for both the undoped and doped (with TBP and LiTFSI) spiro-OMeTAD based HTLs. All the solar parameters, namely, short circuit current density (J_{SC}), open-circuit voltage (V_{OC}), fill factor (FF), power conversion efficiency (PCE), and external quantum efficiency (EQE), are calculated from experimentally measured current density versus voltage (J-V) and wavelength transient characteristics in ambient condition. The maximum PCE of 10.18% is obtained for the doped HTL, whereas 9.51% for undoped HTL. The improved performance due to HTL doping is attributed to the enhanced charge transportation of the HTL. The experimental results obtained from the fabricated PSCs are also compared with the SetFos^{TM} TCAD simulation data using the drift-diffusion model. The simulated results are observed to be well matched to the experimental data.

Chapter-6 includes the major findings of the thesis along with a brief outline for the future scope of research related to the present thesis.

----XXX----

CHAPTER 1

Introduction and Scope of the Thesis

Contents

CHAPTER 1

Introduction and Scope of the Thesis

1.1 Solar Cell

Modernization and urbanization of societies and industries have significantly increased the use of energy in everyday life. Over the past several years, increased consumption of non-renewable resources like coal, petroleum, and gases will exhaust all the available natural sources [1]. The limited resources of fossil fuels and environmental pollution caused by the burning of fossil fuels have primarily encouraged the researchers for clean and green energy harvesting through renewable energy sources to meet the high demand for energy in the various electrical and electronic applications [2]. The major non-renewable and renewable sources are shown in Figure 1.1.

Solar energy is considered one of the most important renewable sources to solve the present and future energy problems because of its abundant availability and pollution-free generation [3]. Solar energy is converted to electrical energy by a typical solar cell, which has the edge of resolving large energy demand, less effect on climate change, control global warming, clean and unlimited energy source [3]. Various types of solar cells are fabricated using different photoactive materials, namely silicon, germanium, gallium arsenide, cadmium telluride, dyes, conducting polymers, perovskites, etc. [4]. The power conversion efficiency (PCE) of the solar cell primarily depends on photoactive materials and the device structures.

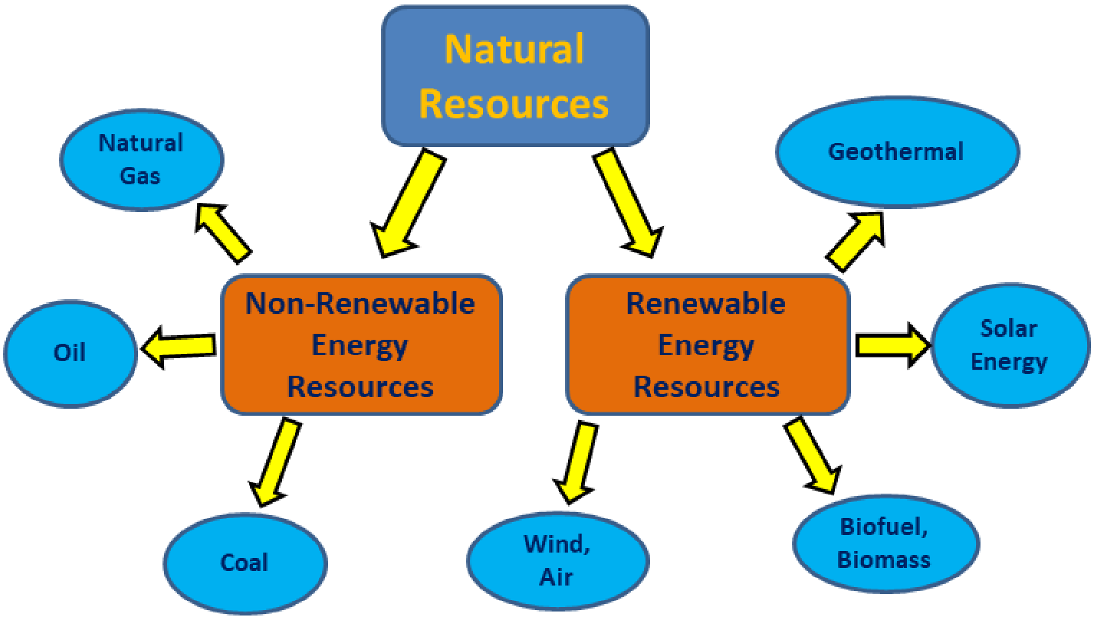

Figure 1.1: Various non-renewable and renewable energy sources.

1.1.1 Origin of Solar Cells

The Concept of the photovoltaic effect was first experimentally discovered by French physicist Edmond Becquerel in 1839 [5]. Later, Willoughby Smith passed an electric current through selenium and found the effect of light on electric current in 1873 [6]. He described that the light is striking a photosensitive semiconductor material result in electrical energy. This remarkable discovery is considered as the beginning of the new era for the conversion of solar energy into electrical energy using a solar cell [7]. In 1883, Charles Fritts invented the first solid-state photovoltaic (solar) cell using the thin film coating of gold on light-sensitive material selenium to form the junctions [8]. Although this device had only 1% efficient, it paved the way for future solid-state photovoltaic devices [8]. In 1905, Albert Einstein proposed a new theory of quantum physics and described the photoelectric effect [9]. The research on photovoltaic cells was revolutionized after experimental validation of Einstein's photoelectric theory in 1916 and the Nobel Prize to Albert Einstein in 1921 [9].

Further, p-n junction based solar cells using Cu_2O and Ag_2S was reported by Vadim Lashkaryoy in 1941. The modern device structure of the junction based solar cells was proposed by Russell Ohl [10] in a patent filed in 1946. The first commercial standard solar cell having 6% power conversion efficiency (PCE) was developed using inorganic materials by Daryl Chapin, Calvin Fuller, and Gerald Pearson in Bell Laboratory in 1954 [11]. Later, the production of solar cells was started for commercial use. The first silicon-based solar cell panel was incorporated into US satellite Vanguard 1 in 1958 [Internet Source]. Several satellites such as Explorer III, Vanguard II, and Sputnik-3 were launched with solar cell-powered system onboard in the next few years.

1.1.2 Generation of Solar Cells

Silicon (Si) is the most widely used material in the electronic industry for the last seven decades. Fabrication of Si-based solar cells requires high-temperature processing and various sophisticated requirements, including nanofabrication facilities, ultra-high vacuum deposition process, etc. Further, the preparation of Si from silica is a high energy draining method, which makes very low energy payback time (EPBT) of the silicon-based solar cells. Moreover, the management of extremely large e-wastes resulting from the worldwide use of solar cells made of Si and other inorganic semiconductors have become a challenge for environment and water management systems. Thus, rigorous research is focusing on developing organic and hybrid semiconductors for environment-friendly and low-cost solar cells. The organic material was first introduced in the solar cell by Calvin in the 1960s [12]. The idea of a multi-junction solar cell came in 1970, and the layer of different semiconductor material was used in a solar cell to absorb a broad spectrum. The real breakthrough in the field of photovoltaic devices came with the introduction of two different photosensitive semiconductors instead of one semiconductor material by Tang in 1986 [13]. The German and French scientists built a multi-junction solar cell and recorded 46% power conversion efficiency in 2014 [14]. The solar cell development using various types of material in the different periods is categorized into four generations of the solar cells, as illustrated in Figure 1.2.

The present day's solar market is dominated by the first two generations [15], [16]. The first generation includes eminent and medium-cost technologies (i.e., mono or polycrystalline Si and GaAs based solar cells), which results in moderate yields. The second-generation mainly comprises thin film (TF) technology-based solar cells that are cheaper to manufacture but have lower efficiency [16]. Copper Indium Gallium Selenide (CIGS) and CdTe/CdS based solar cells are examples of the second generation. Then, the third-generation solar cells are very efficient but expensive as they explore the usage of novel materials and the variability of designs [17]. They involve technologies based on newer compounds, stacked or tandem multilayers of III-V materials (inorganics based), Quantum Dots (QDs), Dyed Sensitized Solar Cells (DSSCs), etc.

Finally, the fourth generation is currently under investigation and is also recognized as "Inorganics-in-Organics". It mainly syndicates the flexibility or low cost of polymer TFs with the efficient and stable novel inorganic nanostructures (such as metal oxides and nanoparticles) along with organic-based nanomaterials (like graphene or its derivatives, carbon nanotubes) [18]. The recent development in solar cell manufacturing includes solar cells made of several organic, inorganic, and organometallic halide perovskite materials. The exceptional improvement in the power conversion efficiency from 3.8% to 25.2% in the perovskite solar cell (PSC) has been observed in a very short span of time. Moreover, the cost to manufacture a perovskite solar cell is a fraction of the cost of other thin-film technology with almost equivalent performance. Although PSC has lower stability over time, it has several advantages, such as low-temperature solution processing and the ability to produce a flexible solar cell. All these advantages and the availability of a wide range of perovskite materials can be used to fabricate more exciting and appropriate solar cells.

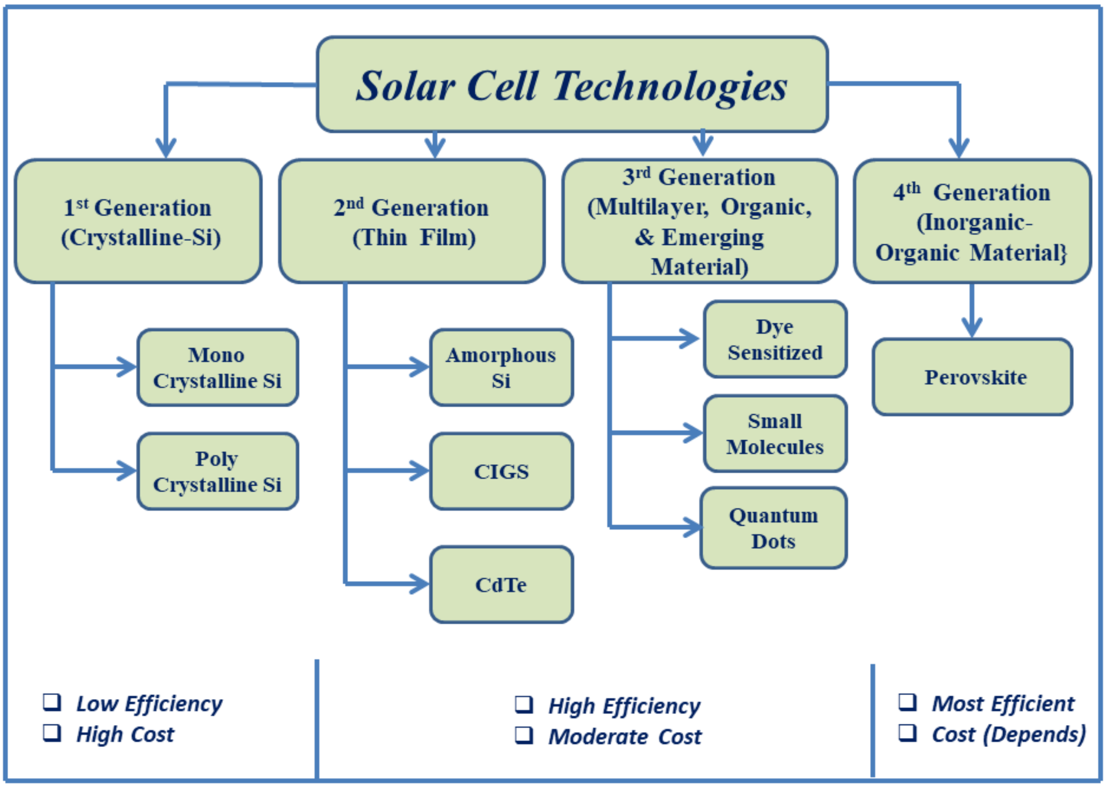

Figure 1.2: Different generations of solar cells.

1.2 Perovskite Solar Cell

Perovskite solar cell comes under the most recent generation of the solar cell. It has the inherent advantage of high efficiency, low cost, and easy fabrication process. The PSCs are made using perovskite structured material as photoactive. The efficiency of the PSC depends mainly on the perovskite material used. The achieved efficiency for perovskite solar cells is comparable to the Si and other materials-based solar cells' efficiency, as shown in Figure 1.3. The improvement in the PCE has been achieved by optimizing the thin-film processing technology and bandgap engineering of the perovskite film in the solar cells [19]. Efficiency has also been enhanced by choosing a suitable wide bandgap organic or inorganic material for electron transport layers (ETLs), hole transport layers (HTLs), and bandgap alignment in the device structure. Moreover, the defects such as pinholes and grain boundaries created during the fabrication process and the material properties such as extinction coefficient, carrier mobility, diffusion length, bandgap, etc., affect the PCE of the solar cells.

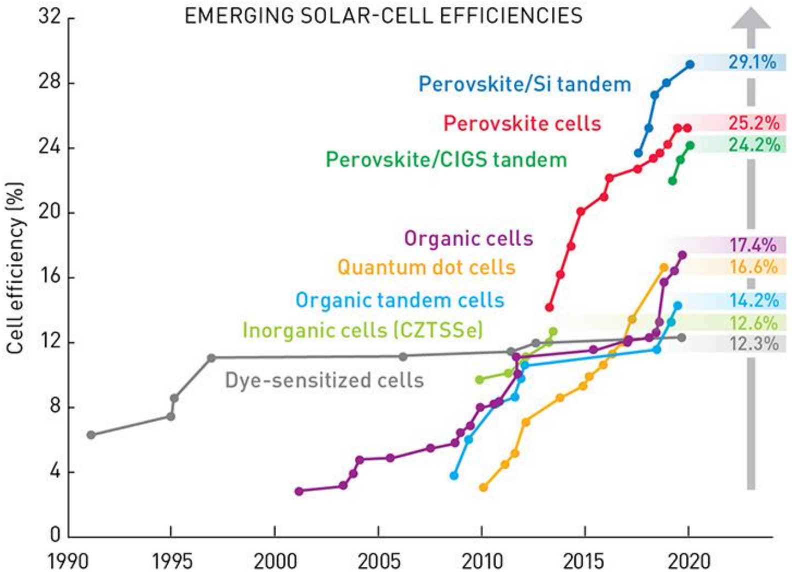

Figure 1.3: Comparative rapid growth in PCE for perovskite-based solar cells [20].

1.2.1 Perovskite Material

Perovskite material was first discovered by the Russian mineralogist Gustav Rose in 1839 in a piece of chlorite rich skarn. The mineral was $CaTiO_3$, named after the legendary Russian mineralogist Count Lev A. Perovskiy [21]. Later, the name perovskite was also referred for the three-element metal oxides such as $PbTiO_3$, $BiFeO_3$, $BaTiO_3$, etc., having a perovskite structure with the formula ABO_3. These metal oxides find use in several ferroelectric, dielectric, pyroelectric, and piezoelectric applications. Nowadays, the name perovskite does not only refer to metal oxides but also to halides, which have halide anions (F^-, Cl^-, Br^-, I^-) in place of oxide anions (ABX_3; A = cation, B = divalent metal cation, X = halogen anion). The halide perovskite was discovered by Well et al. in 1893 during their experiments on the synthesis of cesium-based lead halide compounds, $CsPbX_3$ (X = Cl, Br, I) [22]. The real breakthrough for the perovskite occurred in 1957, when C. K. Møller, a Danish researcher, reported that $CsPbCl_3$ has the perovskite structure [23].

The first three-dimensional organic-inorganic hybrid perovskite was discovered by replacing cesium in $CsPbX_3$ (X = Cl, Br or I) with methylammonium cations (MA = CH_3NH_3+) by Dieter Weber in 1978 [24]. The organic-inorganic hybrid perovskite ($CH_3NH_3PbI_3$) is most commonly used as photoactive material for making highly efficient photovoltaic and optoelectronic devices. The lead halide perovskite materials possess unique and much suitable semiconductor properties such as high absorbance coefficient, direct bandgap, large diffusion length, etc., which allow them to manifest into efficient photovoltaic cells and other optoelectronic applications such as light-emitting diodes (LEDs), photodetectors, X-ray detectors, and so on. Despite their eccentric electronic and optoelectronic properties, the two major issues are that stability and toxicity of the perovskite materials have held up their commercial applications in the current scenario. In this thesis, 3D organic-inorganic lead halide perovskites have been analyzed for photovoltaic applications.

1.2.1.1 Crystal Structure

The crystal structure of hybrid perovskite compounds is similar to $CaTiO_3$ or in more general form ABX_3. Typically, the ‘A’ atoms are larger than the ‘B’ atoms. The ‘A’ and ‘B’ cations coordinate with 12 and 6 ‘X’ anions, respectively, to form cuboctahedral and octahedral geometries, as shown in Figure 1.4.

Table 1.1: Comparison of optical properties of perovskite with other materials.

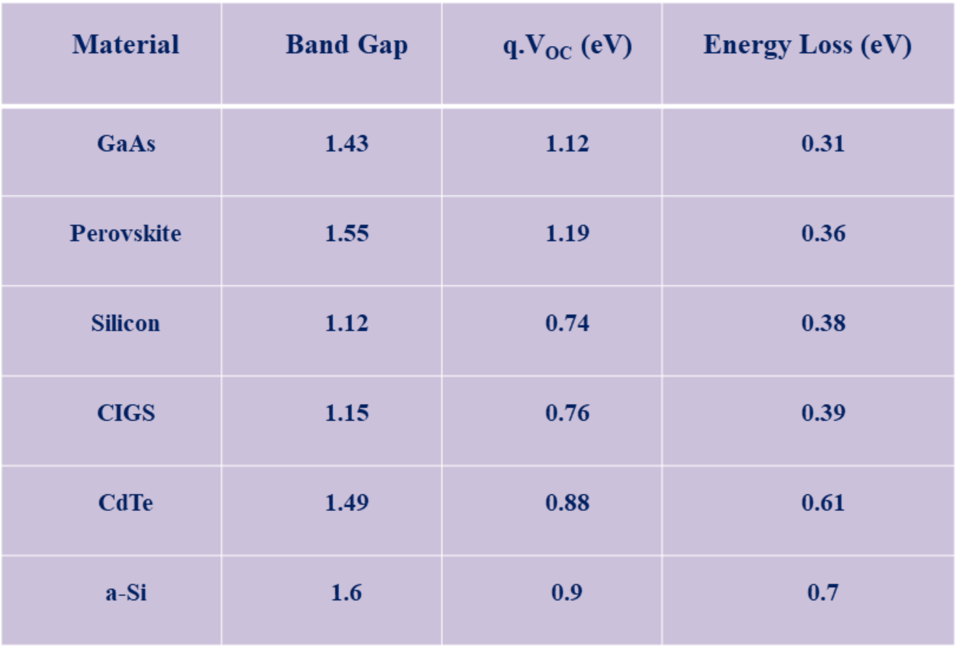

Material	Band Gap	$q.V_{OC}$ (eV)	Energy Loss (eV)
GaAs	1.43	1.12	0.31
Perovskite	1.55	1.19	0.36
Silicon	1.12	0.74	0.38
CIGS	1.15	0.76	0.39
CdTe	1.49	0.88	0.61
a-Si	1.6	0.9	0.7

The halide perovskites have semiconducting properties that are highly desirable for photovoltaic (PV) and other optoelectronic applications. The essential parameters of perovskite are compared with other common materials used for solar cell fabrication and listed in Table 1.1.

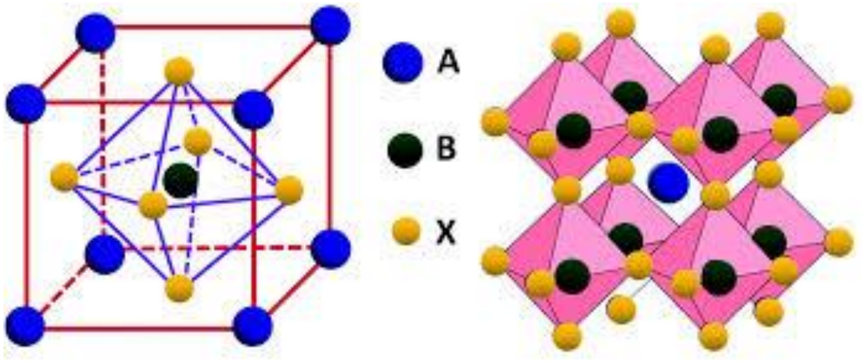

Figure 1.4: (a) Structure of ABX_3 perovskite (b) Cubic unit cell of $CH_3NH_3PbI_3$ [25].

1.2.1.2 Optoelectronic Properties

The ionic nature of organic-inorganic halide perovskite materials and their semiconducting properties, i.e., allow a free tuning of absorption edge wavelength (bandgap) and optical absorption by varying or combining halide ions (Cl, I, Br), thereby developing mixed-halide solid solutions. Methylammonium lead iodide ($MAPbI_3$) is a unique intrinsic semiconductor [26] showing superior mobility of both photogenerated holes and electrons. Figure 1.5 illustrates the band diagram for $MAPbI_3$, where the valence band (VB) incorporates nearly ~25% Pb $6s^2$ orbitals (lone pair) and 70% I 5p orbitals, while the conduction band (CB) contains a mixture of $6p^2$ orbitals of Pb and several other orbitals. In such a case, there exists strong coupling in VB orbitals between I 5p orbitals and Pb lone-pair $6s^2$ [27]. The structure of $MAPbI_3$ is highly symmetric, which results in the direct bandgap in this material. Moreover, Pb s orbital lone pair enables p-p electronic transitions from VB to CB. Therefore, the combination of these factors imparts extraordinarily high optical absorption coefficients to $MAPbI_3$ (~10^5 cm^{-1}) [28]. The acclaimed defect tolerant properties of perovskite material are credited to its ionic characteristics, strong I p-Pb s anti-bonding coupling, and weak I p-Pb p coupling [27]. This property is replicated by the $MAPbI_3$ having large carrier diffusion lengths. Moreover, as $MAPbI_3$ is an intrinsic semiconductor, it has ambipolar carrier mobility owing to its ionic crystal. On a final note, recombination between electrons and holes is suppressed in halide perovskites due to a charge-screening effect against Coulombic interaction, which is assisted by the high ionic density of the perovskite.

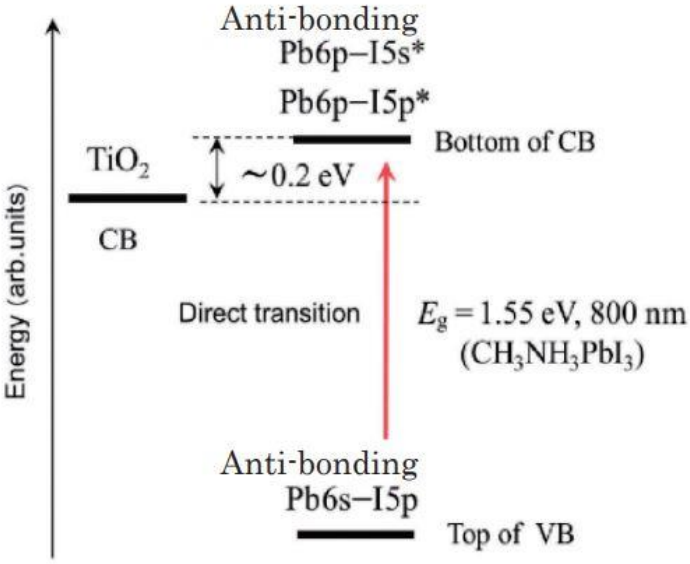

Figure 1.5: Band structure of $MAPbI_3$ [29].

The optical bandgap of the hybrid perovskite material can be tuned by the changing in “A” site cation and “B” site cation [30]. Perovskite quantum dots (QDs) offers tunability with size, which can be controlled using changing the concentration of the capping agents or surfactants (octyl amine and oleic acid) [31]. $CH_3NH_3PbI_3$ also has the ability to be used in photodetector because it shows the high gain of the photoinduced current, which exceeds 100%. Nowadays, perovskites have potential use for color image sensors in digital cameras. The perovskite-based color sensors and photodetectors take advantage of the low-cost and printable semiconductors and are expected to be commercialized soon. Perovskites are also used for the detection of X-

Rays in the medical diagnosis. It works well because lead-based perovskites have high absorption coefficients for X-ray radiation. Samsung's research group and Park et al. reported the detection of an actual X-Ray image by using a 2D patterned image sensor [32]. Organic lead halide perovskite-based optoelectronic semiconductor devices may also be used as radiation sensors for space explorations owing to their high defect tolerance nature.

1.2.2 Working Principle of Perovskite Solar Cells

The perovskite-based solar cells are commonly made in p-i-n structure, as shown in Figure 1.6. The organic-inorganic hybrid perovskites (i.e., $CH_3NH_3PbI_3$, $CH_3NH_3PbBr_3$, $CH_3NH_3PbI_3$, etc.) are used as intrinsic (i) layer and work as photoabsorber. The wide bandgap conducting polymers (i.e., spiro-OmeTAD, PTAA, etc.) and metal oxides (i.e., TiO_2, ZnO, etc.) are used for the p and n layer, respectively. The photovoltaic operation in the p-i-n structured perovskite solar cell is based on three basic concepts: (a) Generation of charge carrier in absorber (i) layers, (b) Separation of charge carrier by transport (p and n) layers, and (c) Collection of charge carrier at electrodes. When the solar cell is illuminated with sunlight having photon energy (hv) greater than the bandgap (Eg), the photon is absorbed by the absorber layer, and the charge carrier is generated. Due to the internal electric field, the electron-holes pair are separated by consecutive electron and hole transport layers. If these charge carriers are not separated, they will recombine shortly. Finally, the charge carrier is collected by the top and bottom electrodes of the solar cell and creates the photovoltage across the device. The polarity of the output voltage is the same as the "forward bias" direction of the device, but the photocurrent is opposite to the direction of the forward current through the device under dark condition.

Solar light causes a current (I) to flow from the solar cell to the load. The magnitude of this current (I) is the algebraic sum (without sign) of generated current (I_{PH}), the current flowing in the non-linear junction (I_D), and the current passing through shunt resistance (I_{SH}). The equivalent electrical circuit of the solar cell has been shown in Figure 1.7. The I-V characteristics equation for the equivalent electrical circuit of the solar cell under illuminating condition is given as,

$$I = I_{PH} - I_S \left[exp\left(\frac{V + I \times R_S}{V_T} \right) - 1 \right] - \frac{V + I \times R_S}{R_{SH}}$$

where I_{PH} is photogenerated current, I_S is reverse saturation current, and V_T is the thermal voltage.

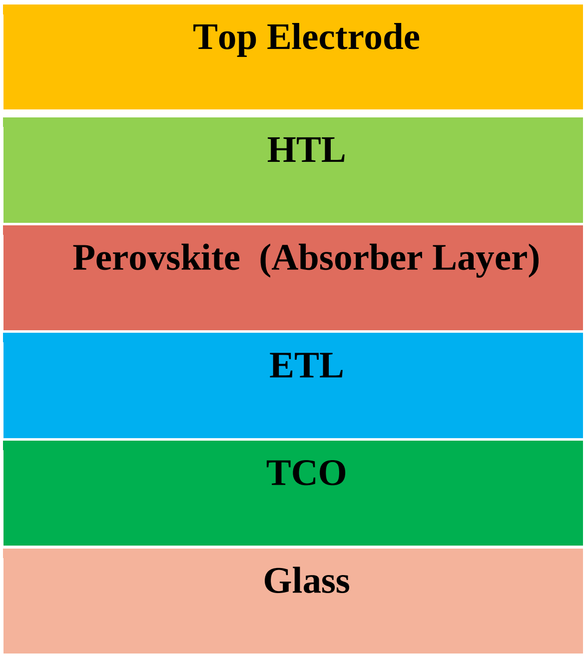

Figure 1.6: General structure of perovskite solar cell.

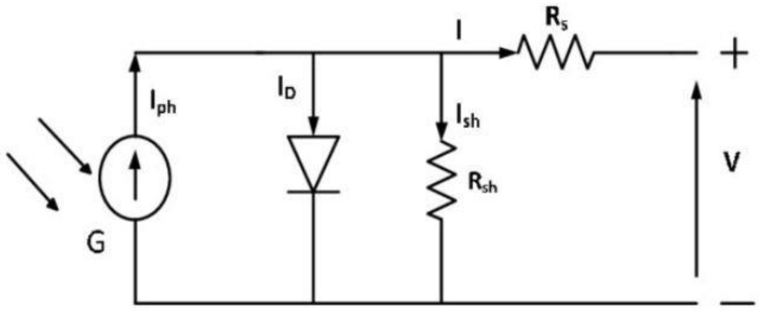

Figure 1.7: Electrical equivalent model of the perovskite solar cell [16].

It is evident from the I-V characteristic equation that solar cell parameters are greatly affected by series and shunt resistance. The impact of series resistance and shunt resistance on solar cell parameters are analyzed by the equivalent circuit shown in Figure 1.7. The series resistance R_S, represented in the equivalent circuit, can arise due to the contact resistance, resistance of semiconducting layers, and the contact resistance of electrodes. The shunt resistance, R_{SH}, can similarly be caused by various factors, such as surface leakage along the edge boundaries, crystal defects, or pinholes in the surface. The thickness of the different layers is also a factor that changes the resistance of the device and affects the performance of the solar cell. It can be observed that the zero value of R_S and the infinite value of R_{SH} gives the best performance (ideal case).

The performance of the solar cell is specified using four main solar cell parameters, namely open-circuit voltage (V_{OC}), short circuit current (J_{SC}), fill factor (FF), and power conversion efficiency (η). The electrical equivalent model, shown in Figure 1.7, and the current density-voltage (J-V) curve, shown in Figure 1.8, are used to analyze these characteristics of the solar cell. For all the values of J and V, the product of these two quantities gives the power density (P=J×V), and the product has a maximum value (called Pmpp) at a particular current and voltage value (called Jmpp and Vmpp). The short circuit current density and open-circuit voltage are described as:

$I\ (at\ V=0) = I_{SC}\ and$

$V\ (at\ I = 0) = V_{OC}$

Or

$I_{SC} = I_m = I_\ell$ *and* $V_{OC} = V_m$ for forward-bias power quadrant

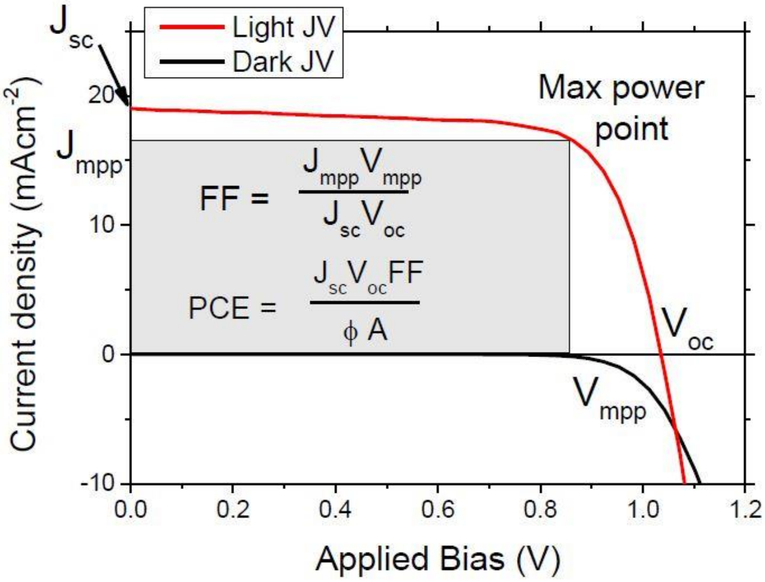

Figure 1.8: J-V curve for PSC device where the red curve is for under illumination and black is for dark. The area in the shade gives maximum achievable power.

On the other hand, the fill factor (FF) is evaluated by comparing the maximum power to the theoretical power (P_T). The fill factor also reflects the J-V curve's squareness, which represents the effects of resistive and recombination losses. The fill factor depends on open circuit voltage and short circuit current density, so there can also be a reduction in short circuit current below the value of the photocurrent due to the forward biasing across the junction as a result of the voltage drop across the series resistance (R_S). Finally, power conversion efficiency (η) is defined as the ratio of output energy of the solar cell (P_{MPP}) to the incident optical power density from the sun (P_{in}). PCE can also be written as,

$$\eta = \frac{Output}{Input} = \frac{I_m V_m}{\sum nh\upsilon} = \frac{V_{OC} J_{SC} FF}{P_{in}}$$

1.2.3 Numerical Modelling of Perovskite Solar Cells

A numerical simulation-based modeling approach is performed to develop a highly efficient solar cell, obtain optimum solar cell parameters, and understand the device physics. The fabrication cost can be minimized by optimizing device characteristics using technology computer-aided design (TCAD) simulation. Several TCAD simulation tools, such as SCAPS-1D, Lumerical, AMPS, SETFOS (Fluxim), etc., are available for the electrical and optical simulation of organic and hybrid perovskite solar cells [33]. Among these two popular tools, SCAPS-1D and SETFOS^{TM} (Fluxim) are used in the present thesis work for the validation of the experimental results.

The numerical simulation model for the DSSC, silicon solar cell and other hybrid solar cells explains the behavior of the charge movement and the factor that affects the performance of the device. The performance of DSSC is based on the redox level in electrolytes, so the model includes a solvent that conducts ions and current. Similarly, the simulation models of the silicon-based photovoltaic device involve the doping that forms the p-n junction. The working principle of the perovskite solar cell is different from DSSC and silicon solar cells. The redox level and doping level is not required for the PSCs simulation model. Electrons and holes contribute to the current generated by photons energy in the PSC. So the numerical simulation plays a vital role in understanding carrier transportation mechanism and device performance.

The SCAPS-1D simulator can efficiently simulate the CIGS, CdTe, and crystalline solar cell (Crystalline Si and GaAs), which comprises up to 7 layers, whereas SETFOS can also be used for simulation of organic LED, solar cell as well as tandem solar cell structure with different layers. The simulation and modeling of hybrid perovskite solar cells are reported first time by Agrawal et al. [34] in 2015. The SETFOS simulation tool includes four different types of models, such as drift-diffusion, absorbance, advanced optics, and emission for a solar cell with a fitting and optimization algorithm. The Emission module deals with dipole emission, full-spectrum, color filter, and substrate optics, whereas the scattering module helps in improving the optical efficiency of the material. The charge generation, recombination, and transportation profile are managed by the absorption and drift-diffusion modules. The basic parameters required for electrical simulation are electron affinity (X), Bandgap (Eg), dielectric constants, the density of states of the conduction band and valence band (N_C and N_V), mobility of electrons and holes (μ_e and μ_h), the thermal velocity of electrons and holes, doping concentration of acceptor and donor (N_A and N_D), absorption coefficient, defect density (N_t) of different layers and also working temperature.

In these simulation tools, there is the flexibility to choose parameters either graded or different profiles. Optically we can separately define reflection, transmission, and other parameters. It also provides the option to vary the illumination spectra such as AM1.5G, AM0, AM1.5D, etc. SCAPS-1D provides generation- recombination status, energy band, quantum efficiency, and J-V characteristics, which is used for the calculation of open-circuit voltage (Voc), short circuit current (Jsc), power conversion efficiency (PCE), and fill-factor. The sweep function is also available in the tools, which is very useful for optimizing the performance of the solar cell by varying the material parameters such as thickness, defect density, doping, etc., of the different layers.

The simulation tools solve Poisson's equation for the electric field, which depends upon charge flow and trap centers in the material. Poisson's equation for a semiconductor can be stated as [35]:

$$\frac{d^2\phi(x)}{dx^2} = \frac{e}{\epsilon_0 \epsilon_r}\left(\rho(x) - n(x) + N_D - N_A + \frac{\rho_d}{e}\right)$$

The current density due to electron or hole at any point in the device must be identical at all the points under the steady-state condition in dark condition. However, generation and recombination affect the current density under illumination. The continuity equation for electrons and holes can be inscribed as [35]:

$$\frac{dJ_n}{dx} = G - R$$

$$\frac{dJ_p}{dx} = G - R$$

Also, the total currents are calculated from drift and diffusion components as [35]:

$$J_n = D_n \frac{dn}{dx} + \mu_n n \frac{d\emptyset}{dx}$$

$$J_p = D_p \frac{dn}{dx} + \mu_p p \frac{d\emptyset}{dx}$$

Where J_n and J_p are current densities due to electron and hole, G is generation rate R is recombination rate, ϕ is electrostatic potential, e is electric charge, ε_o is vacuum permittivity, ε_r is relative permittivity, p and n are electron and hole concentration, N_A and N_D are charged impurities of donor and acceptor and ρ_d is defect charge density.

The recombination models commonly used are band-to-band recombination, SRH (Shockley-Read-Hall) recombination, and Auger recombination, as illustrate in Figure 1.9. Band to band (rediative recombination) and Auger recombination are unavoidable because these are intrinsic material properties. Band-to-band recombination is the process in which the electrons fall back from the conduction band to the valence band to recombine with holes. The expression for the band to band recombination is given as [35]:

$$R = \gamma(n.p - n_i^2)$$

Where γ is the recombination coefficient. The SRH (Shockley-Read-Hall) recombination takes place due to the impurities and defects in a material. These defects create trap states, which are essential for this recombination; hence it is also called trap-assisted recombination. The rate of this recombination can be expressed as:

$$R_{SRH} = \frac{p.n - n_i^2}{(n + n_i) + \tau n(p + n_i)}$$

Where τp and τn are electron and hole lifetime, n_i is intrinsic carrier concentration.

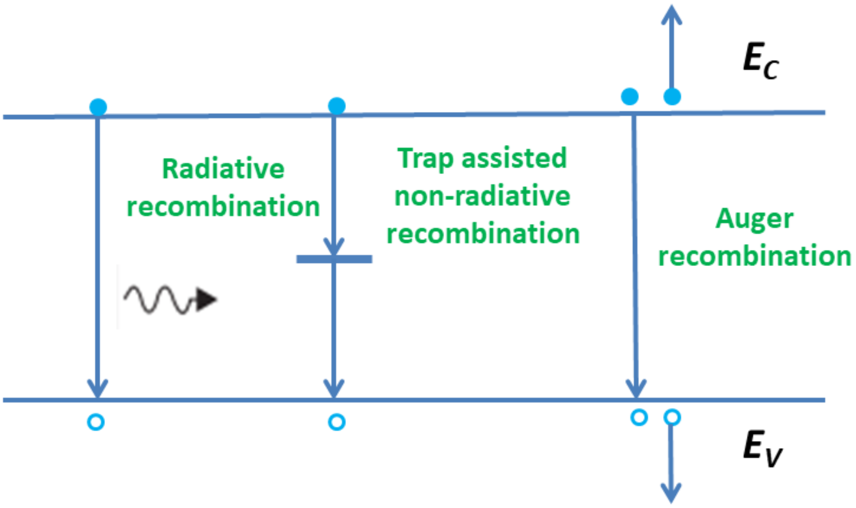

Figure 1.9: Band-to-band (radiative recombination), SRH, and Auger recombination.

SRH recombination occurs extensively when defects between crystal grains are present and cause increased trap states. Therefore, single-crystal materials have generally lesser SRH recombination due to extrinsic impurities and dangling bonds at the surface. In Auger recombination, the energy released by a band to band recombination of an electron-hole pair is given to another carrier. It can be expressed as [35]:

$$R = (C_n^A + C_p^A)(np - n_i^2)$$

Where c_n^A and c_p^A are constants.

1.3 Fabrication Process for Perovskite Solar Cells

The perovskite solar cell is a multilayered thin-film device. The different layers, namely electrodes (anode and cathode), photo absorber, hole transport layer, electron transport layer, and other interface layers, are composed of different materials in the solar cell structure. Some key processing steps should be considered for high-performance solar cells. First of all, a suitable bandgap material (absorber material) is chosen to absorb the maximum solar light spectrum, the next one is selecting the wide bandgap electron and hole transport material to separate maximum charge carriers, and finally, the suitable work function material for electrodes are required to collect the maximum charge carriers. This section briefly discussed the various layers of perovskite solar cells.

1.3.1 Electrodes

The suitable top and bottom electrodes are used for better collection of charge carriers to get high-performance solar cells. Different physical vapor deposition (PVD) techniques such as sputtering, thermal, electron beam, etc., are commonly used to obtain a thin film of metals (Al, Ag, Cu, Au, Pd, Pt, etc.) and doped semiconductors (ITO, FTO, etc.) for the electrodes.

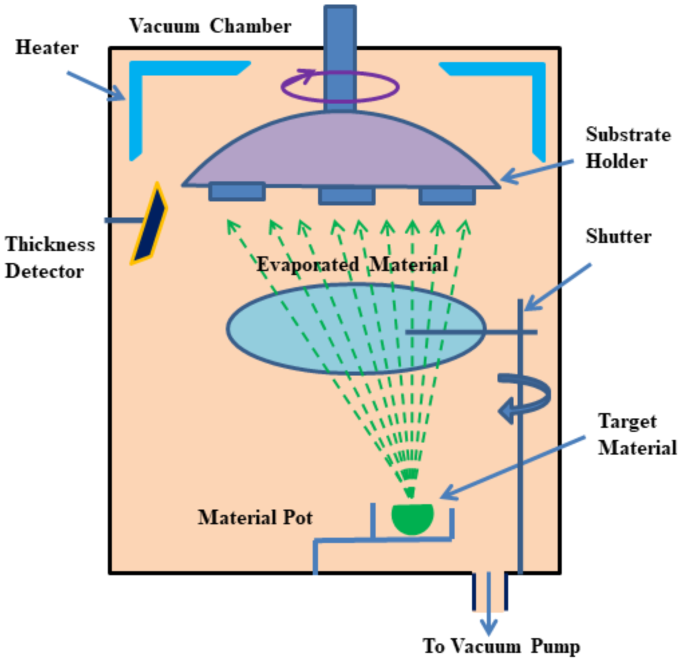

Figure 1.10: Block diagram of physical vapor deposition.

A block diagram of a typical PVD system is illustrated in Figure 1.10. The ITO/FTO is primarily deposited by the sputtering method and used as transparent conducting oxide electrodes at the bottom of the solar cell so that maximum light can pass through it. Noble metals, Au and Pd, with high work function (~4.8 to ~5.1 eV) are the most suitable top electrodes (avoiding fast oxidation and degradation) for perovskite solar cell is commonly deposited by thermal and electron beam evaporation. Thermal evaporation is also employed to deposition high purity Ag/Al film as a top electrode on both the solution-processed and thermally deposited metal oxide ETL.

1.3.2 Photoabsorber Layers

The photoabsorber layer is the most crucial layer, and perovskite material is used for this layer. The LUMO and HUMO level of hybrid perovskite material can be easily modified by using the composition of different halide anions (i.e., the composition of Cl, Br, and I in hybrid perovskite), and thus the absorbance coefficient changes. In the last few years, the power conversion efficiency of perovskite solar cells has been remarkably increased by gradual development in deposition techniques of perovskite thin film. The film coating controls the morphology and crystallinity of hybrid perovskite material that affects the absorbance coefficient of perovskite material and significant impact on short circuit current density. The stability of perovskite film also depends on the growth and crystallinity of perovskite material.

The high solar cell performances achieved in this short period are primarily due to the extensive efforts that have been invested over the years to develop and optimize these perovskite thin film deposition procedures [27]. These deposition methods include single step deposition [36], sequential deposition [37], vapor assisted deposition (via single source and dual source) [38], screen printing, and anti-solvent methods [39]. Among these, sequential deposition and anti-solvent methods are two of the most widely used (methods) for the fabrication of solar cells. The PCE of hybrid PSC is achieved over 25.2% via sequential deposition technique [40]. In general, the spin coating deposition technique has enormous potential for the development of highly efficient perovskite solar cells for large scale production. Therefore, these achievements are very promising for the scale up of perovskite photovoltaics in the near future [27]. The three common deposition methods are discussed in following sub-sections:

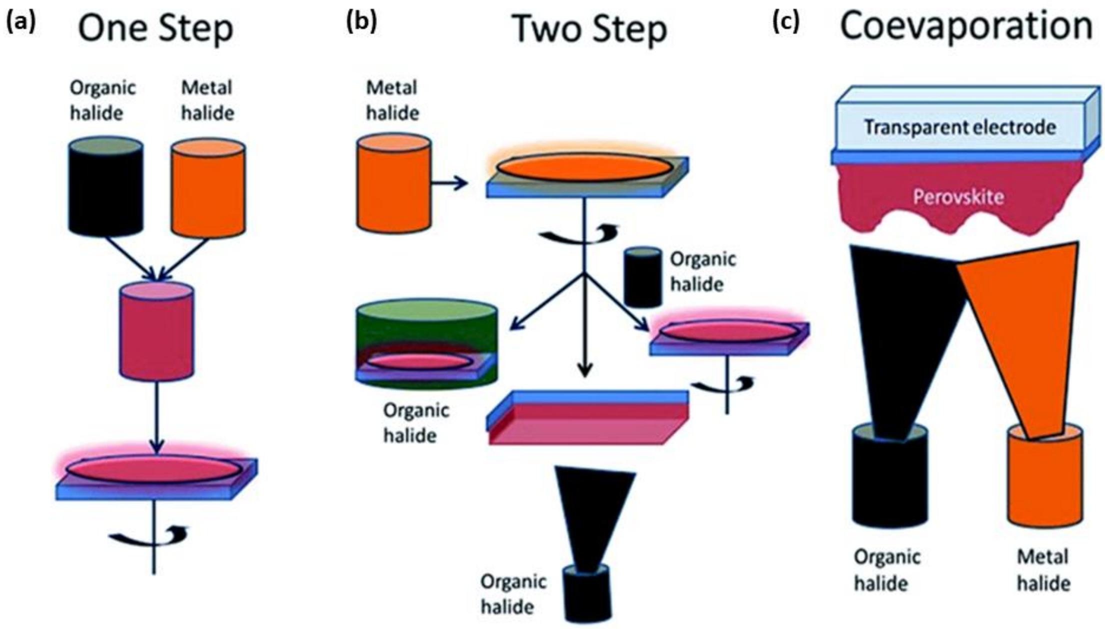

Figure 1.11: Deposition methods for the perovskite thin film: (a) One step deposition, (b) Two step deposition, and (c) Physical vapor deposition [41].

1.3.2.1 One Step Deposition via Spin Coating

The perovskite thin-film is initially deposited via spin coating in a single step on mesoporous metal oxide films using an equimolar ratio of PbX_2 and CH_3NH_3X in a common solvent [42]. Polar solvents, such as dimethylformamide (DMF), dimethylsulfoxide (DMSO), g-butyrolactone(GBL), or N-methyl-2-pyrrolidone (NMP), are commonly used [43]. Spin coating is followed by heating the film at 70–150^{o}C to evaporate the high-boiling point solvent and in order to increase the grain size and crystallinity of hybrid perovskite ($MAPbX_3$) thin film [43]. The perovskite deposited substrate is converted from light yellow to dark brown after cooling at ambient temperature and confirmed the formation of perovskite film [42]. The problem with these deposition methods is that non-uniformity and uncontrolled grain size. Typically, it leads to uncontrolled precipitation of the perovskite with large morphological variations in photovoltaic performance in the resulting devices.

1.3.2.2 Two Step Deposition via Spin Coating

A sequential deposition method for perovskite thin layer is first employed by Liang et al. [28] to enhance the performance of PSC. For the preparation of organic-inorganic lead halide ($CH_3NH_3PbI_3$) thin film, the solution of organic compound (PbI_2) is infiltrated in the mesoporous layer of Al_2O_3 or TiO_2, and the film is dried by evaporating the solvent. In the 2nd step, the PbI_2 deposited substrate is dipped into the solution of organic compound (CH_3NH_3I). Conversion of perovskite thin-film occurs within the mesoporous when both the compound organic and inorganic comes into contact, permitting much better control over the perovskite morphology. The sequential deposition technique is further optimized for performance improvement of hybrid PSCs by Burschka et al. [37]. This significantly increased the reproducibility of device performance and achieved a PCE of approximately 15%. Further, with the development of technology, the anti-solvent technique has been employed for enhanced performance parameters of perovskite solar cells. Jeon et al. [44] have used an anti-solvent method during deposition of perovskite thin film to fabricate highly efficient hybrid perovskite solar cells.

1.3.2.3 Vapor assisted deposition technique

Vapor assisted deposition process is a novel techniques for the deposition of high quality and uniform perovskite thin film. In this method, the first step includes the deposition of the inorganic compound via solution process followed by deposition of physical vapor of organic compound from a single source. This technique provides full surface coverage and moisture stability in a non-vacuum solution. The vapor assisted solution process is distinct from other traditional solution deposition techniques because it decelerates nucleation and permits robust reorganization of thin-film growth. Ping fan et al. reported a PCE of 10.90% for perovskite solar cells based on the single-source physical vapor deposition method [32]. The vapor deposition via dual-source process is used for well-defined grain structure, extremely uniform deposition, and full surface coverage of perovskite thin-film without post-heating treatment. But the simultaneous control of evaporation of both the organic and inorganic compound is very difficult to handle with dual-source evaporation methods.

1.3.3 Charge Transport Layers

Wide bandgap hole blocking and electron blocking materials are commonly used for ETL and HTL, respectively, in the PSCs. The structural and material engineering of the ETL and HTL plays an important role in the performance improvement of the PSCs. Efficiency can be enhanced by choosing a suitable wide bandgap material for ETL, HTL, and bandgap alignment in the device structure [45]. The primary function of the ETL and HTL layer is to extract the electron and hole from the absorber layer and transport them to electrodes. The energy band alignment between HTL (ETL) and absorber layer plays an essential role for transportation of hole (electron) and blocking of the electron (hole) to minimize charge carrier recombination.

The structural, chemical, electrical, and optical properties of the charge transport layers (ETL/HTL) strongly depend on the deposition techniques and the environment under which the deposition of the materials is performed on the desired substrate. Various methods such as spin coating, thermal evaporation, electrochemical, hydrothermal, spray coating, screen printing, vapor deposition, chemical bath deposition, etc., are employed for the deposition of ETL and HTL of the solar cell. The comparison of various methods is listed in Table 1.2. The spin coating and screen printing (Blade coating, slot die coating), spray coating, hydrothermal, etc., are chemical solution-based, low-cost techniques. Metal oxide electron transport layers such as TiO_2 and ZnO are deposited by all techniques. However, the hydrothermal method is mostly used for the nanostructures (nanorods, nanowires, nanotubes, etc.) based thin film of TiO_2, ZnO, and other metal oxides at low cost and low temperature. The hydrothermal process provides a controlled size and shape of the nanostructures with highly crystallized and uniform.

Table 1.2: Comparison of different deposition techniques for charge transport layers.

Methods	Advantages	Disadvantages
Sputtering: Thin-film is deposited by ion bombardment of the source (target) by generated plasma on the desired substrate.	1. Large surface area deposition 2. Good reproducibility	1. It may be surface damage in the substrate used. 2. A high-cost vacuum chamber is required
E-beam evaporation: The electron beam is used to deposition thin-film by the transformation of atoms into the gaseous phase.	1. Good for liftoff 3. Highest purity 4. High precision of film thickness 5. Ease of operation 6. Excellent material utilization	1. Some CMOS processes sensitive to radiation and heat 2. Difficult for alloys 3. Poor step coverage and decomposition 4. A high-cost vacuum chamber is required
Chemical bath deposition (CBD): The thin film layer is deposited by dipping substrates in solutions with ions of interest (particularly metal ions).	1. Simple and low-cost experimental set up requires 2. Easy Control of the thickness of the film	1. Lack of reproducibility compare to other chemical deposition methods
Sol-Gel: This method is based on inorganic polymerization reactions in which colloidal solution is used for deposition of the thin film of metal oxide. It includes four steps: hydrolysis, polycondensation, drying, and thermal decomposition.	1. Excellent composition control 2. Can be used for large scale production. 3. Low cost and low-temperature technique	1. Film thickness control 2. Optimization for the particle size of the colloidal solution required 2. Surrounding environment affects the film 3. Porosity control is difficult 4. Multiple thin film layer may cause cracks
Chemical Vapor deposition (CVD): Deposition by chemical reaction of reactants at the substrate surface and energy for the reaction is provided by heat.	1. High purity 2. Relatively high deposition rates 3. High quality, high-performance thin film	1. High temperatures requirement 2. The precursors material should be volatile at room temperature
PECVD: The chemical vapor deposition the technique uses plasma to improve the yield and performance of the synthesis	1. Less temperature required 2. Good material properties of the deposited thin film.	1. In some cases, toxic precursors are needed 2. High-cost equipment 3. Plasma could damage the deposited thin films
Spray Pyrolysis: The traditional multisource CVD process can be converted to a single-source deposition process by spraying a solution onto a surface at an adequate temperature	1. Simple and low– cost method 2. Suitable for large scale deposition	1. Size of droplets of the initial solution is not the same which can lead to inhomogeneity in the material
Hydrothermal deposition: This is a simple deposition technique that requires a specific growth temperature under high pressure to synthesize single-crystalline material using an aqueous solution. This is commonly used for the deposition of TiO_2/ZnO nanorods.	1. Better control of size and shape of thin film 2. It is possible to obtain high crystallized nanostructures	1. Optimization is required for the process 2. Problems in reproducibility.

1.4 Characterization Techniques for Perovskite Solar Cells

The different types of characterization techniques are commonly used to analyze and verify different layers in the solar cell structure. The characterization includes surface, optical, and optoelectronic for the thin films and devices, as follows:

1.4.1 Surface Characterization

Some essential surface characterizations are performed to understand the basic properties of the synthesized perovskite and other associated materials in the solar cell structure. The brief discussion on these characterization tools are discussed in the following subsections:

1.4.1.1 Atomic Force Microscopy

Atomic force microscopy (AFM) is a surface imaging technique used to find the surface topography of the deposited film. It is a type of scanning probe microscopy (SPM) and is widely used for height, surface roughness, and magnetism measurements. The resolution of the AFM is in the order of a fraction of nanometer that is 1000 times higher than the optical diffraction limit. Surface imaging through AFM is taken place by measuring the force between the tip of the probe and the sample under process, as depicted in Figure 1.12 (a). Three modes of operations of the AFM are as follow:

Contact mode: The raster scanning of the sample with respect to the tip of the probe for a minimal area is taken place to obtain the image.

Non-contact mode: In this mode of operation, the probe oscillates at the resonance frequency, the sample under process is kept standstill, and the force between probe and sample is measured to get the exact image.

Tapping mode: It is somewhere between contact and non contact mode of operation and takes advantage of the above two. The sample is escaped from being damaged by incorporating intermittent contact.

1.4.1.2 Scanning Electron Microscopy

Scanning electron microscopy (SEM) is a powerful tool to get the morphological, topographical, and compositional information of the sample through a focused beam of electrons. High resolution (better than 1 nanometer) image is produced by raster scanning of the electron beam and combining the beam's position with the detected signal, as depicted in Figure 1.12 (b). The most common mode of operation of the SEM is the detection of the secondary electron emitted by the atoms excited by the electron beam. The topographical image of the sample is produced by detecting the number of secondary electrons emitted by atoms excited by the electron beam. Energy dispersive X-ray (EDX) attached with SEM is used to find the elemental composition of the sample. Data produced by EDX analysis shows spectra consist of unique peaks corresponding to the elemental composition of the material.

1.4.1.3 Transmission Electron Microscopy

Transmission Electron Microscopy (TEM) is a technique to study the topography, morphology, composition, and crystallography of the material. TEM utilizes high energy electrons and electromagnetic lenses for characterization, as depicted in Figure 1.12 (c). TEM generates high-resolution images with a maximum resolution near 0.5Å. The selected area electron diffraction (SAED) pattern is primarily used for crystallographic measurement utilizing the wave nature of electrons instead of particle nature. A high energy (~100-400 keV) parallel beam of the electron is passed through the sample. The electron beam has a wavelength in the nanometer range compared to atom spacing in the prepared sample. Electrons are diffracted by atoms of the material, and the scattering angle defines the crystal structure of the sample.

1.4.1.4 X-Ray Diffraction

X-ray Diffraction (XRD) is a widely used tool to extract information about crystal structure, phase, texture, and other parameters such as average grain size, defects, etc., of the nanomaterial. Data produced by XRD analysis is based on the diffraction pattern, as depicted in Figure 12 (d). The X-Ray strikes on each set of lattice planes of the sample at a specific angle in the process of the extraction of the sample information.

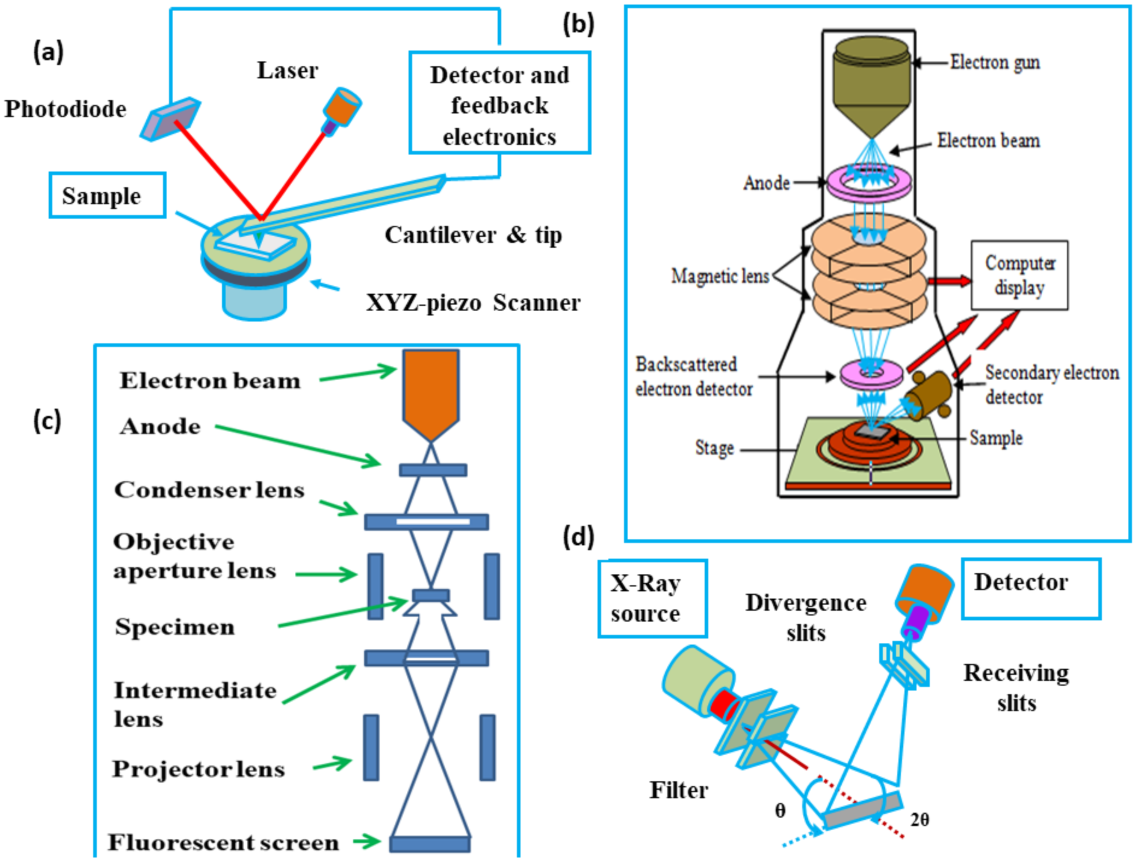

Figure 1.12: Meaurement setup for (a) AFM (b) HRSEM, (c) TEM, and (d) XRD.

1.4.2 Optical Characterizations

The optical characterization technique is a non-contact and non-destructive type analysis. It is commonly used to find the parameters such as absorbance, reflectance, transmittance, emission, film thickness, crystal structure, optical constant, etc., of the sample under investigation.

1.4.2.1 Absorbance

The absorbance technique is an extensively used technique for the evaluation of various parameters, namely absorbance, reflectance, transmittance, film thickness, crystal structure, optical constant, etc. The absorbance is also measured in reflectance and transmittance mode. It is also used to study the spectral composition of the light reflected from the surface with respect to the angularly dependent intensity and the composition of the light initiated from the light source. This study provides the film thickness as well as refractive index, coating homogeneity, and the other optical constant. Absorbance is primarily measured using the UV-Vis spectroscopy technique, as depicted in Figure 1.13 (a). In this technique, UV/visible light is passed through the sample, and the difference in intensity after transmission gives information about the optical characteristics of the sample.

1.4.2.2 Photoluminescence

The photoluminescence technique is a powerful non-contact and non-destructive type technique widely used to extract information about the electronic structure of the semiconducting materials. Under light illumination, photoexcitation occurs by absorbing the light and imparting the excess energy into the material. This excess energy can be dissipated in the form of light emission called photoluminescence, as depicted in Figure 1.13 (b). Data generated by this analysis provides excitation and emission peaks corresponding to the materials, and based on these peaks electronic structure of the corresponding material is extracted.

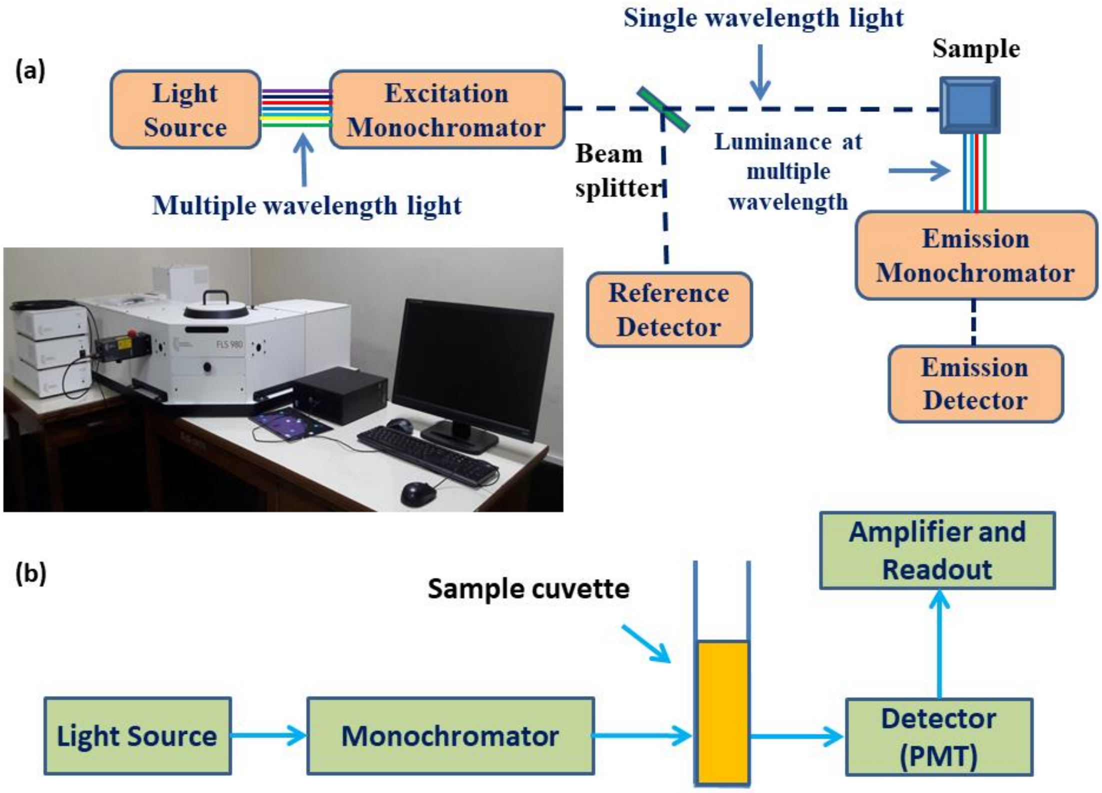

Figure 1.13: Measurement setup for (a) Photoluminescence spectrometer and (b) UV-Vis absorption spectroscopy.

1.4.3 Optoelectronic Characterizations

Electrical characterization of semiconducting materials or devices plays an essential role in examining its suitability for the integrated circuit used in different kinds of electronic devices such as mobile phones, computers, digital cameras, etc. The electrical characterization of electronic devices is called electronic characterization, and the measurement of change in electronic characteristics under optical illumination is called optoelectronic characterization. The complete experimental setup for the measurement of various electrical and optoelectronic characteristics is depicted in Figure 1.14.

Current (I)-voltage (V) characteristic of any device shows how the current flowing through the device is being changed with respect to the voltage applied on terminals. An I-V characteristic is very crucial to evaluate various device parameters such as ideality factor, barrier height, etc. Capacitance (C)-voltage (V) characterization of any device represents the relationship between junction capacitance and the voltage applied across the terminal of the device. C-V characteristics are junction dependent and are used in the calculation of barrier height, carrier concentration, and depletion width. Impedance spectroscopy is used to study the resistance or capacitance properties of the device by applying the AC sinusoidal excitation signal. On the other hand, the I-V characteristics under dark and solar light illumination are used for the evaluation of various solar cell parameters.

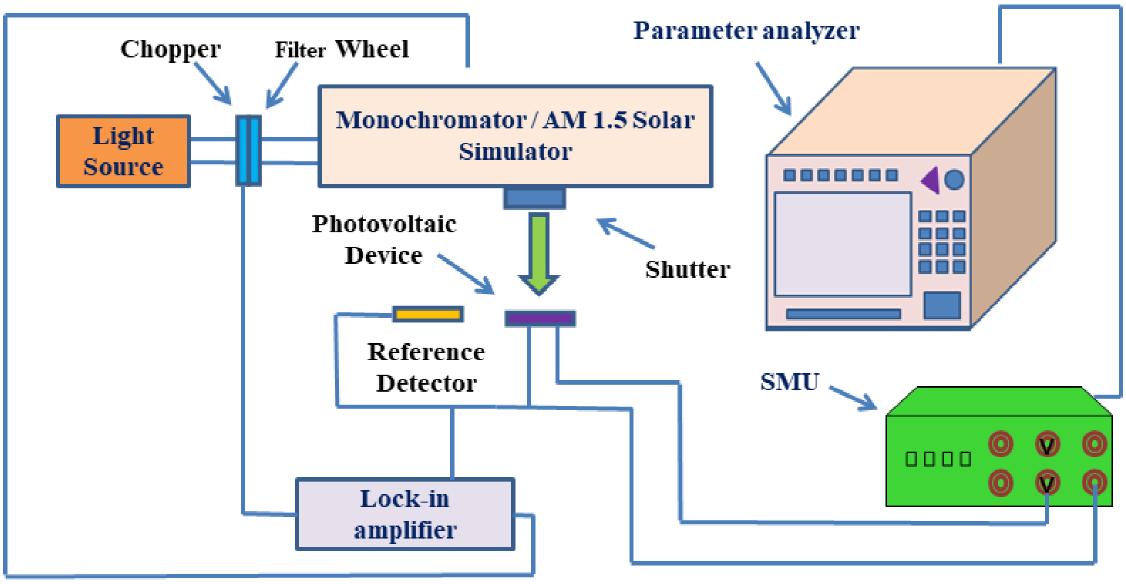

Figure 1.14: Optoelectronic characterization setup for perovskite solar cells.

1.5 Literature Review

This section aims to summarize the gradual development of perovskite solar cells and the detailed discussion on hybrid perovskite-based solar cells. First of all, the perovskite solar cell with different hole transport materials and some additives have been reviewed. Later, some crucial works on TiO_2 and ZnO nanorods based hybrid perovskite solar cells have been reviewed.

1.5.1 Review of Perovskite Based Solar Cells

The inorganic-organic hybrid perovskite is the emerging photosensitive material for photovoltaic applications due to its high absorbance coefficient and suitable bandgap [46]. The journey of perovskite solar cells began in 2006 with a power conversion efficiency (PCE) of 2.2% by Miyasaka et al. [47]. They have also reported the PCE of 3.1% and 3.8% by using $CH_3NH_3PbBr_3$ and $CH_3NH_3PbI_3$ sensitizers, respectively, in the dye-sensitized solar cell (DSSC) [48]. Considerable efforts have been made in the last few years to improve the PCE of the hybrid perovskite solar cells (PSCs) to near 25% [49]-[53], as depicted in Figure 1.15.

Perovskite sensitizer used with liquid electrolyte faced serious stability issues in the solar cell structure. In 2008, Miyaska et al. have employed a solid-state hole transport layer in PSC and fabricate carbo/conductive polymer composite based first solid-state PSC with PCE of 1% [54]. Later, Gratzel et al. reported Sb_2S_3 and poly(3-hexylthiophene) (P3HT) based solid-state perovskite photovoltaic device with 5.13% PCE [55]. Park et al. fabricated the first perovskite solar cell based on perovskite quantum dot (an equimolar mixture of the organic and inorganic compound in g-butyrolactone solvent) and achieved PCE of 6.5% in 2011 [56]. Later, Park et al. made a full solid-state device by employing nanoparticles (NPs) of $CH_3NH_3PbI_3$ as a light sensitizer on mesoporous ETL and recorded the PCE of 9.7% in 2012 [57]. Snaith et al. fabricated solar cells by incorporating a new deposition technique (dual-source vapor deposition) for perovskite thin film and get an excellent PCE of over 15% in 2013 [58]. In 2014, Juan et al. investigated the impedance spectroscopy measurement for $CH_3NH_3PbI_{3-X}Cl_X$ solar cell and studied the physical parameters of carrier transport and recombination in compositions based perovskite thin film [59].

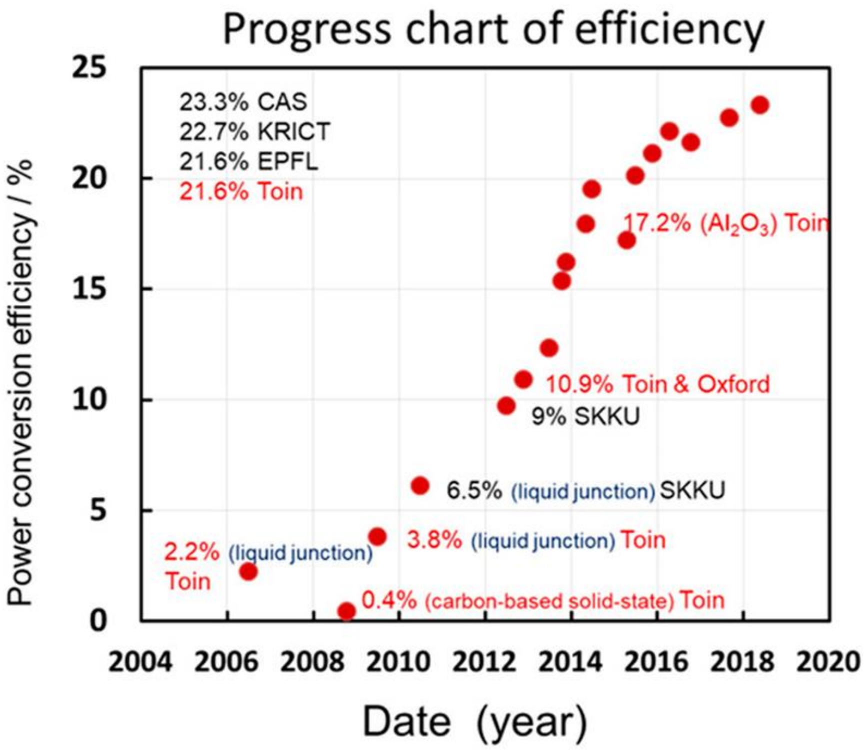

Figure 1.15: Progress in the power conversion efficiency of PSCs from 2006 to 2018 [60]

Further, Luo et al. [61] reported first-time perovskite nanowire-based hybrid solar cell and recorded 14.71 % PCE in 2015. Madhavan et al. [62] reported more than 20% PCE in 2D/3D perovskite-based PSC using CuSCN as a hole transport layer. They have also reported a photovoltaic device with photo-electrochemical systems that employ mesoscopic forms of semiconducting oxides as light absorbers. In 2015, Niu et al. [63] investigated the chemical stability of perovskite material in different environmental conditions such as oxygen, moisture, UV-light, etc. The charge carrier transport behavior of quantum dots in perovskite material has been explained by Ning et al. [64], whereas the optical and electrical properties of perovskite material for photovoltaic and optoelectronic applications have been reported by Jung and Park [65] in 2015**.** Yang et al. [66] have investigated different electron transport layer-based perovskite solar cells in 2017. The performance of organic HTL and ETL based hybrid PSCs with a different annealing temperature for the perovskite layer have been studied by Jhong et al. in 2017 [67]. Hayase has reported a compositional mix of PbI_2 and SnI_2 based hybrid and toxic-free hybrid perovskite solar cell [68].

Furthermore, the performance of $CH_3NH_3SnI_3$-based solar cells with several types of HTM layers such as CuSCN, Cu_2O, and spiro-OMeTAD are optimized using the TCAD simulation [69]. The ZNRs are employed for ETL in all the PSC structures and achieved remarkable PCE of 18.34%, 20.23%, and 20.21% for CuSCN, Cu_2O, and spiro-OMeTAD based HTL. Li et al. [70] have grown ZNRs on the aluminum-doped ZnO seed layer and fabricated PSCs with the following structure: ITO/AZO seed-layer/ZnO-NRs/perovskite/spiro-MeOTAD/Au. They analyzed the surface preheating effect on parameter performance of ZNRs based PSCs and achieved optimum J_{sc} of 21.43 mA/cm^2, V_{oc} of 0.84 V, FF of 57.42%, and PCE of 10.34% with reduced pinholes in perovskite layer due to substrate preheating. P.S.Chandrasekhar et al. [71] demonstrated the performance of nitrogen-doped graphene/ZnO nanorod nanocomposites based PSC with improved device parameters photocurrent of 21.98 mA/cm^2 and PCE of 16.82% compare to without graphene-based PSCs.

1.5.2 Review of TiO_2 nanorods Based Perovskite Solar Cells

Various types of organic and inorganic materials such as PCBM, C_{60}, TiO_2, ZnO, SnO_2, and Al_2O_3 have been reported as ETL in the PSCs [72], [73]. Among them, TiO_2 is the most promising material for the ETL due to its large bandgap, high stability, and desired band bending with perovskite material [74]. The TiO_2 based ETL improves the stability of the PSCs and hence is mostly preferred over other metal oxides [73]. Different TiO_2 nanostructures such as nanotube, nanosheets, nanoparticles, nanorods, and nanowires have been used as ETL in highly efficient PSCs [75]-[78]. However, TiO_2 nanorod is preferred over other nanostructures in the PSCs due to its better charge transportation and robustness with perovskite materials [74].

Alberti et al. and Lozhkina et al. [79], [80] have developed thin solid-state hybrid solar cells composed of mesoscopic TiO_2, based solar cells using solution-printable processes. They have also developed other perovskite cell structures toward the realization of full printable technology of high-performance hybrid solar cells. The perovskite layer in PSC structure FTO/TiO2/Perovskite/SpiroOMeTAD/Au was fabricated via blade coating, and ETM/HTM material was deposited using thermal evaporation technique with an active solar cell area of 100 cm^2 by Razza et al. [77] and achieved 4.3 % PCE. Recently, Wan et al. [81] have improved the efficiency of CdS-sensitized TiO_2 solar cells by hydrothermal etching treatments of TiO_2 nanorods (TNRs). Priyadarshi et al. [82] introduced another deposition technique, drop cast for perovskite material for large area (70 cm^2) fabrication of PSCs structure of FTO/TiO2/ZrO2/Carbon/Perovskite and recorded 10.74% PCE. The PSC with 11.32% PCE based on an active area of 1.47 cm^2 was fabricated by Gao [83] using 50 nm compact layer of TiO_2, spiro-OmeTAD based HTM layer by spin coating, and 300 nm thin perovskite layer via knife coating method.

1.5.3 Review of ZnO Nanorod Based Perovskite Solar Cell

The ZnO nanomaterials are among the most promising wide bandgap material for solar cell applications, LED, and photodetectors. ZnO is a widely used electron transport material due to its high mobility, easy synthesis, abundant availability, and high stability [84], [85]. In general, ZnO nanostructure is preferred in the ETL over its bulk counterpart due to the larger surface-to-volume ratio. The surface to volume ratio plays a vital role in photocatalytic activity [86]. Although 0D material (colloidal quantum dot) has a large surface to volume ratio, its use in perovskite solar cell structure is very less due to poor charge transportation. One dimensional material (ZnO nanorods) offers increased photocatalytic efficiency compared to bulk ZnO. Compared to other nanostructures, ZnO nanorods have fast electron transportation, a large conduction band, and high electron density. Son et al. [86] have reported the maximum PCE of 14.35% using (NH4)2TiF6 treated ZnO NRs based ETL in the PSC structure. Xu et al. [87] have obtained the PCE of 9.15% using ZnO NR (ZNR) arrays synthesized by modified solvothermal method.

Liu et al. have reported PCE of 15.4%% using ZnO ETL and vapor deposited hybrid perovskite material [58]. From the last two decades, there was some modification in the quality of single-crystalline ZNRs to improve the performance of optoelectronic and photovoltaic devices [88], [89]. Several techniques such as seed layer via spin coating, sputtering, chemical bath deposition (CBD), electrostatic spraying, atomic layer deposition (ALD) have been used for uniform growth of ZNRs for minimizing the defects and traps [87], [90]–[92]. The bandgap of ZnO nanomaterials can be tuned by doping with some metal dopants like Al, Mg, and P. [88], [93], [94]. Shirazi et al. have also reported the ZNRs based HTL free hybrid PSC and achieved efficiency improvement by increasing the conductivity of ZNRs by Al doping [93]. Jeon et al. found the uniform and defect-free layer of perovskite when the toluene has been used as anti-solvent during spin coating deposition of perovskite thin film. The better phase formation and crystallinity of PbI2 with MAI (methylammonium iodide) are achieved when DMSO has been used as a solvent for PbI_2 precursor instead of DMF [44].

Peng et al. [95] minimized the decomposition of the hybrid perovskite layer by insertion of the SnO_2 layer on ZnO nanorods. The core-shell SnO2-ZnO nanostructures have been used to increase the oxygen vacancies at the ZnO-hybrid perovskite interface [95] for stabilization of perovskite later. The power conversion efficiency of hybrid PSC is significantly improved from 6.92% to 12.17%, and hysteresis is eliminated from the J-V curve by taking the core-shell nanostructure of the SnO_2-ZnO layer.

Zhang et al. [96] used a relatively fast and low temperature processed electrochemical method for deposition of ZnO layer and demonstrated low J-V curve hysteresis with PCE of 11% in the fabricated ZnO nanostructures based PSCs on ITO coated flexible substrate. The charge carrier mobility and charge recombination mechanism have also been investigated by Zhang et al. [97] for ZnO thin film deposited via electrospraying technique-based PSCs. They have also reported the performance of ZnO nanostructured based PSCs for perovskite thin film deposition via one-step and two-step deposition methods.

Later, several ZnO nanostructures deposited via different techniques such as pulsed laser deposition [98], electrophoretic deposition [99], PECVD [100], magnetic sputtering [101] have been explored for the fabrication of different types of PSCs structures, including planner [102], inverted planner [103], and mesoporous [97]. Kumar et al. [104] fabricated the perovskite/Spiro-OMeTAD/Au based PSCs with four different planner structure for ETL, namely FTO/ZnO(CL), FTO/ZnO(CL)/ZNRs, PET/ITO/ZnO(CL), and PET/ITO/ZnO(CL)/ZNRs. They have synthesized ZNRs using chemical bath deposition technique on FTO/ITO substrate with and without ZnO seed layer and recorded PCE of 8.90% for FTO substrates and 2.62% for flexible PET/ITO substrate-based PSCs.

1.5.4 Major Observation from the Literature Survey

The milestones achieved in the area of perovskite solar cells during their development are interesting to note [60]. It is observed that the period of 2013-2015 was focused primarily on the development of high-efficiency cells by using appropriate material selection and deployment of methods for high-quality perovskite film formation. This period also addressed issues regarding hysteresis and interfacial engineering. In 2016-2017, compositional engineering is applied widely, which resulted in improvement in both structural stability and efficiency. Extensive efforts are made to develop lead-free perovskites too. Now, after developing and optimizing methods of synthesis, the attention of researchers is on making the perovskite solar cell more stable for long-term use by addressing issues regarding light, moisture, oxygen, and thermal instability. Currently, attempts are made to scale up the production of solar cells for meeting industrial requirements, and the methods such as mechanochemical synthesis are gaining popularity due to their solvent-free nature. Also, extensive research is being carried out in the area of all-inorganic halide based perovskites solar cells.

1.6 Issues and Challenges in Perovskite Solar Cells

The commercialization of hybrid PSC is still challenging because of toxicity issues (during fabrication, deployment, and disposal), long term chemical and phase stability, and cost-effectiveness. The perovskite material pertains to its stability and degradation due to moisture, oxygen, UV radiation, and temperature. The three major areas of thrust in perovskite research are: improving the material stability like phase stability, thermal stability, and replacement of the toxic heavy metal (Pb^{+2}). One possible modification has come through the substitution of cations, metal ions, and halogen to solve these challenges. Tin (Sn) is a candidate for the replacement of lead (Pb^{2+}) cation and can help in bandgap tuning of the perovskite material.

Compositional engineering is the leading interest in perovskite research for optimizing structure and usability governing factors. The hybrid perovskite decomposed in methylammonium, hydrogen iodide, and lead iodide in the presence of water. The prominent approach is the substitution of a methyl group with a bulky organic cation, leading to a 2D perovskite structure. The 2D layered and 3D bulk perovskite material can then be used to alternatively coat layers to prevent moisture impingement due to the hydrophobic nature of the alkyl group and avoid further degradation; however, with its own challenges such as disorientation, grain size improvement. Though, to enhance air stability, some butyl halide groups could be used. The compositional change by n-butyl ammonium iodide in the methyl group can yield towards low dimensionality. So, Goldschmidt tolerance factor will change accordingly based on the composition of methyl and butyl group. A suitable tolerance factor will make a more stable perovskite material against moisture and oxygen.

1.7 Motivation and Problem Definition

It is discussed that the perovskite solar cells have some inherent challenges for commercialization. The identified challenges and their possible solutions are listed as follows:

- ❑ The 3rd generation of solar cells (organic solar cells) has low efficiency.
    - ✓ The absorbance coefficient of perovskite material is relatively more so efficiency can be improved by incorporating perovskite material.
- ❑ The low energy photons of solar spectrum (having energy less than the bandgap of active material) incident on photovoltaic device can't be converted into electricity and lost while the excess energy of high energy photon (having energy greater than the bandgap of active material) have been lost in heat form.
    - ✓ This can be easily overcome by changing the "A" cation of the perovskite material, and the suitable bandgap material (quasi-2D/3D perovskite) can be employed in PSCs for wide bandgap absorption.
- ❑ The efficiency of planar PSCs is less compare to mesoscopic PSCs.
    - ✓ The efficiency can be enhanced using TiO_2 and ZnO nanostructure in PSCs. The mesoporous layer (nanorods, nanowires, nanotubes, etc.) permits the perovskite photo absorber to penetrate mesoporous framework material, enhancing the absorption due to the high surface volume ratio of the perovskite material. So the incorporation of mesoporous material into PSCs improves the efficiency of PSCs.
- ❑ The planar perovskite solar cell has less stability

- ✓ By the incorporation of TiO_2 and ZnO NRs in PSCs, the stability can be improved. The monohydrate phase forms rapidly when the hybrid perovskite layer is deposited on a compact layer, but the decomposition rate of hybrid perovskite material is reduced when mesoporous scaffolds are employed.

Therefore, in this thesis, we focussed on optimizing the mesoporous n-type electron transport layer to improve the efficiency and stability of the perovskite solar cell.

1.8 Scope of the Thesis

The present thesis deals with the fabrication, characterization, and TCAD simulation of some $CH_3NH_3PbI_3$ hybrid perovskite-based PSCs using TiO_2 nanorods (TNRs)/ ZnO nanorods (ZNRs) as the ETL and Spiro-OMeTAD/PTAA as the HTL in the device. All the PSCs considered in the present thesis are of conventional n-i-p mesoporous device structure where the n-region represents the ZNRs/TNRs based ETL, i-region includes $CH_3NH_3PbI_3$ hybrid perovskite-based active layer, and the p-region represents the Spiro-OMeTAD or PTAA based HTL in the PSCs. The thesis consists of SIX chapters, including the present chapter. The outline of the remaining FIVE chapters is briefly described as follows:

Chapter 2 reports the fabrication, simulation, and characterization of FTO/TiO_2 Nanorods/$CH_3NH_3PbI_3$ (Hybrid-Perovskite)/PTAA/Pd structure-based perovskite solar cells (PSCs) where the FTO (fluorine-doped tin oxide) is the substrate, TiO_2 nanorods (NRs) layer acts as the electron transport layer (ETL), hybrid perovskite ($CH_3NH_3PbI_3$) is the active layer, PTAA is the hole transport layer (HTL), and Pd film acts as the contact electrode in the device. The TNRs are grown by the hydrothermal process followed by $TiCl_4$ treatment for enhancing the performance of the device. The perovskite thin-film active layer and PTAA based HTL are deposited using the spin-coating technique. The effect of the ETL thickness on the performance parameters of the PSCs has been investigated and compared with the simulation data. The fabrication and characterization have been performed in open atmospheric conditions. The measured electrical and optical characteristics for three devices with three different ETL thicknesses were compared with the TCAD simulation results for comparing performance parameters of the proposed structure under real operating conditions and theoretically ideal conditions.

Chapter 3 investigates the effects of solvothermal etching and $TiCl_4$ treatment of the TiO_2 NRs based ETL on the performance of the FTO/TiO_2 NRs/$CH_3NH_3PbI_3$ /Spiro-OMeTAD/Pd PSCs. This study is carried out to basically show that not only the thickness of the ETL but also its surface morphology plays an important role in the performance optimization of the proposed PSC. Three different devices have been studied: The first device contains hydrothermally grown TNRs based ETL, the second device uses a $TiCl_4$ treated TNRs based ETL, and the third device uses solvothermally etched and $TiCl_4$ treated TNRs ETL, maintaining remaining parts of the device same as used in Chapter-2. The growth of other layers in the device is the same as considered in Chapter-2. Finally, the electrical and optical parameters are compared for all three PSC devices mentioned above.

Chapter 4 deals with the investigation of the effect of ZnO NRs ETL (grown on four different types of ZnO seed layers by hydrothermal method) on the performance of FTO/ZnO NRs/$CH_3NH_3PbI_3$/PTAA/Au based PSC structures. Four different types of seed layers of drop-casted ZnO film, spin-coated colloidal ZnO nanoparticles (NPs) film, spin-coated colloidal ZnO quantum dots (QDs) film, and solvothermally grown ZnO NRs film were deposited on four FTO substrates. Then the seed layer coated FTO substrates were processed for growing ZnO NRs (of four different morphologies on four different seed layers) by the hydrothermal method. The $CH_3NH_3PbI_3$ perovskite active layer, PTAA based HTL, Au were successfully deposited for fabricating four different PSC devices under study. The surface morphologies of the four different types of ZnO NRs ETLs were studied by XRD and SEM analyses. The electrical and optical characteristics of the four PSCs with four different morphologies of ZnO NRs based ETLs have been studied in detail. The PSCs with ZnO NRs ETL grown on the ZnO QDs based seed layer showed better electrical and optical characteristics over the other devices.

Chapter 5 investigates the effects of doped and undoped Spiro-OMeTAD based HTL on the performance of FTO/ZnO NRs/$CH_3NH_3PbI_3$/Spiro-OMeTAD/Pd PSCs. The two types of hybrid-PSCs with doped and undoped HTLs were fabricated and characterized. Measured results were compared with the TCAD simulation data to validate the results measured under open atmospheric conditions.

Finally, **Chapter-6** summarizes the major observations and findings of the present thesis. Some future scopes of research related to this thesis have been outlined at the end of this chapter.

CHAPTER 2

Effect of TiO_2 Nanorods (TNRs) ETL Thickness on the Performance of FTO/TNRs/$CH_3NH_3PbI_3$/PTAA/Pd Strcuture Based Perovskite Solar Cells*

Contents

*Part of this work has been published as:

1. Jarwal, Deepak Kumar, et al. "Fabrication and TCAD simulation of TiO_2 nanorods electron transport layer based perovskite solar cells." *Superlattices and Microstructures* (2020): 106463.

CHAPTER 2

Effect of TiO_2 Nanorods (TNRs) ETL Thickness on the Performance of FTO/TNRs/$CH_3NH_3PbI_3$/PTAA/Pd Strcuture Based Perovskite Solar Cells

2.1 Introduction

Thin film-based solar cells are getting much attention to meet the global demand for low-cost and clean energy [105], [106]. Recently, thin-film solar cells are dominated by the inorganic-organic hybrid perovskites, which are synthesized and deposited by low-cost solution processing methods [107]-[109]. The hybrid perovskite materials are now synthesized with a high absorbing coefficient, long diffusion length, ambipolar charge transport, tunable bandgap, and low exciton binding energy [110]–[115]. Considerable efforts have been made in the last few years to improve the PCE of the hybrid perovskite solar cells (PSCs) [49]–[52]. The improvement in the PCE has also been achieved by optimizing the thin-film processing technology along with bandgap engineering of the perovskite film in the solar cells [19].

As discussed in Chapter-1, PCE is significantly enhanced by hybrid perovskite or by choosing a suitable wide bandgap material for electron transport layers (ETLs), hole transport layers (HTLs), and bandgap alignment in the device structure. In the hybrid PSCs, TiO_2 and ZnO are widely used materials for the ETL, while PTAA and spiro-OMeTAD are commonly used for the HTL due to their better alignment of energy levels with those of the perovskite materials [9], [20], [21]. The one-dimensional (1-D) nanostructure is preferred over their bulk counterparts for ETL, as discussed in Chapter-1. The 1-D TiO_2 NRs (TNRs) provide the direct path for the charge carrier transport, thereby enhancing the carrier transportation by nearly 50 to 80 times that obtained in nanoparticles and other nanostructures [27], [28]. Further, TNR also provides enhanced chemical and mechanical stability for the perovskite solar cell structures [28]. Moreover, the low-cost solution processing techniques [28]–[30] are preferred for the large area growth of NRAs.

It is observed from the literature survey discussed in Chapter-1 that no systematic investigations are carried out for the effect of TNRs transport layer thickness on the performance of PSCs. Furthermore, PSCs' performance optimization for different parameters (i.e., dimensional or material) using the computer-aided design (CAD) simulation tool will be an added advantage for practical feasibility, time effectiveness, and cost-cutting. Fabrication and simulation of a Pd/PTAA/hybrid perovskite ($CH_3NH_3PbI_3$)/TiO_2 nanorods (TNRs) based PSC is carried out on an FTO coated glass substrate in this chapter. The CH_3NH_3I (Perovskite), TNRs, and PTAA layers act as active, ETL, and HTL, respectively. Three devices have been considered with three different TNRs based ETL thicknesses. The PSC devices have been fabricated by a chemical solution method in an open environment condition. Measurements have also been carried out in the open atmospheric condition to demonstrate the performance of the PSCs under robust conditions. The measured experimental results for as-fabricated PSCs have been compared with the SCAPS-1D simulation tool to show the difference between the results obtained under the practical and ideal conditions. The content of the rest of this chapter is outlined as follows:

Section 2.2 presents the experimental details for the fabrication techniques for PSCs. Section 2.3 deals with the methodology and process for the numerical simulation of the PSCs. Further, the detailed results and discussion for the fabricated and simulated PSCs are presented in Section 2.4. Finally, the finding and observations of this chapter are summarized in Section 2.5.

2.2 Experimental Details

The fabrication techniques for the perovskite thin films and the PSCs are presented in this section.

2.2.1 Material Used

All chemicals used in the PSCs fabrication were of analytical grade and used directly without any further purification. The materials, PTAA, $PbI_{2,}$ and FTO coated substrate, were purchased from Ossila (UK). Titanium (IV) isopropoxide (TTIP), titanium tetrachloride ($TiCl_4$), dimethylformamide (DMF), hydroiodic acid (HI, 55–58 wt%), methylamine (40 wt%), and hydrochloric acid (HCl, 37 wt%) were purchased from Fisher Scientific.

2.2.2 TiO_2 Nanorods Synthesis and $TiCl_4$ Treatment

The synthesis of TiO_2 nanorods was done by a facile hydrothermal method. First of all, fluorine-doped tin oxide (FTO) substrate ($15\times15\ mm^2$) was cleaned using a soap solution, acetone, and isopropanol in an ultrasonic bath for 15 minutes, respectively. After that, the cleaned FTO substrate was placed in a tilted position (FTO in the downward direction) in Teflon lined cylinder. Now the solutions of 560 μl TTIP, 30 ml HCl (~35%) and 30 ml DI water prepared separately were poured into a Teflon lined cylinder. The cylinder was then sealed properly and kept in a digital muffle furnace (Escon lab. Inst, India) at 180°C. By this method, three types of TNRs samples were prepared of different thicknesses by varying the growth time in the order of 3.5 hour, 5 hour, and 7 hour. The length and diameter of TNRs depend on growth temperature and time. After the cooling at room temperature, the substrate was rinsed in DI water and then washed with ethanol to remove acids and other impurities. Subsequently, the substrate was annealed at 400°C for 1 hour in the air for a proper crystalline TiO_2 layer. The prepared TNRs sample was post-treated in 40 mM aqueous solution of $TiCl_4$ prepared by dissolving 0.5 ml $TiCl_4$ in 100 ml deionized (DI) water at 80°C for 90 minutes [116]. The $TiCl_4$ treatment helps in the minimization of voids and traps in synthesized TNRs ETL [116]. Finally, the sample was annealed at 450°C for 1 hour.

2.2.3 CH_3NH_3I Perovskite Synthesis

The perovskite precursor CH_3NH_3I (MAI) was synthesized by reacting 15.5 mL HI acid (55–58 wt% aqueous solution) and 13 ml methylamine (40 wt%) in an ice bath while stirring up to 4 hours [117]. The light-yellow color product was obtained after vacuum evaporation at 45^oC, followed by washing four times with diethyl ether. Finally, the light-yellow color powder was converted into white color crystalline powder after drying for 48 hours in a vacuum oven at room temperature.

2.2.4 Device Fabrication

The whole PSCs fabrication was carried out under an open-air atmosphere at a relative humidity of 60% measured by a commercially available hygrometer. The hybrid perovskite thin film was deposited via two-step spin coating methods on $TiCl_4$ treated TNRs samples. 10 mg CH_3NH_3I and 462 mg PbI_2 were dissolved in 1 ml isopropanol and 1 ml DMF, respectively, for the perovskite precursor [116]. In the first step, synthesized CH_3NH_3I was deposited on $TiCl_4$ treated TNRs via spin coating at 3000 rpm for 30 seconds, and then the sample was transferred upon the hot plate to anneal for 10 minutes at 70^0 C. In the second step, PbI_2 was spin-coated for 30 seconds at 3000 rpm. Subsequently, a 20 µl solution of toluene was also spin-coated for fully crystalline perovskite film and then annealed at 90^0C for 1 hour to obtain a thickness of 350 nm. The 100 nm PTAA was deposited as HTL on perovskite film at 2000 rpm for 30 seconds. Finally, 80 nm top electrode palladium was thermally deposited on HTL. The block diagram of the fabricated PSC structure is shown in figure 2.1 (a). The possible band diagram for the PSC device structure is shown in figure 2.1 (b).

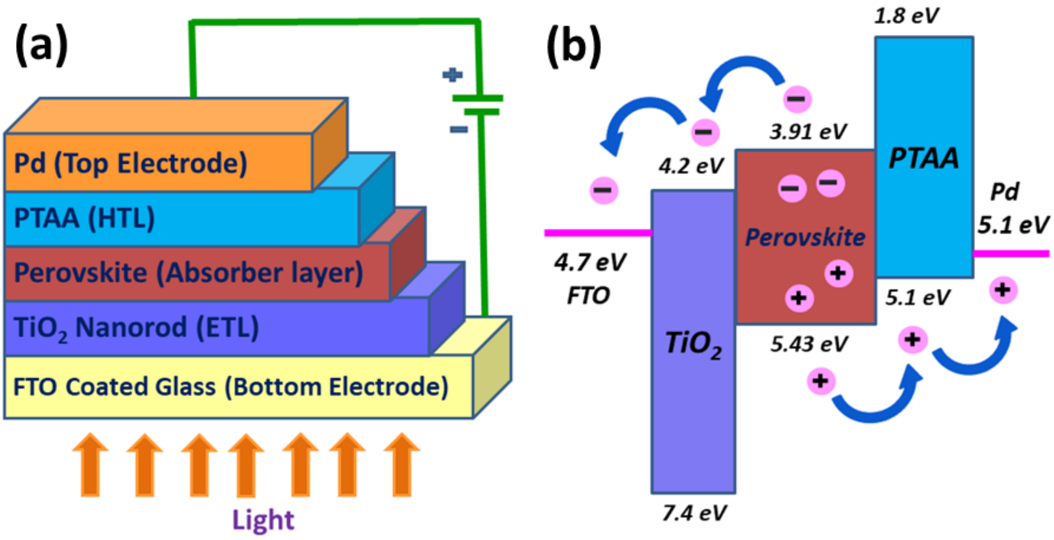

Figure 2.1: (a) Device structure of the PSCs; (b) Band diagram for the fabricated PSCs structure under equilibrium.

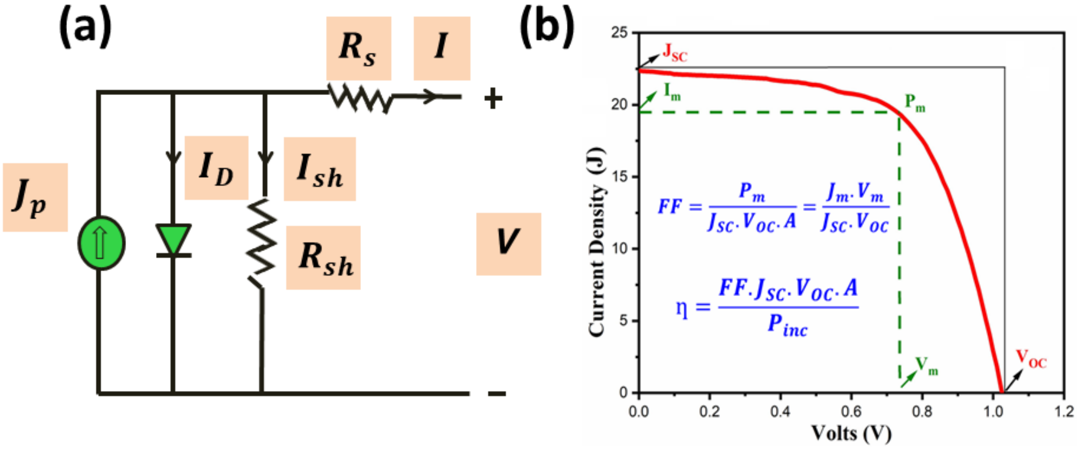

Figure 2.2: (a) Equivalent circuit of perovskite solar cell; (b) Equivalent *J-V* characteristic and performance parameters of PSC.

2.3 Numerical Modeling and Device Simulation

The investigated PSC device is analyzed using the simplified equivalent circuit with solar parameters shown in figure 2.2 (a) and (b). The governing current density-voltage (*J*-*V*) equation under dark and Sun-light is expressed as [118]:

$$J = J_0\{\exp[(q(v - JR_S))/\eta K_B T] - 1\} + \frac{V - JR_S}{R_{Sh}} - J_{ph} \tag{2.1}$$

where, J_0, q, η, K_B, R_S, R_{Sh} are the reverse saturation current density, carrier charge, ideality factor, Boltzmann constant, series resistance, and shunt resistance, respectively. T and J_{ph} are the temperature and photon current density.

The 1D TCAD simulation has used the drift-diffusion and Shockley-Read-Hall (SRH) recombination models for computing recombination, trapping, doping, and electric field distribution in the device [119]-[120]. In a hybrid perovskite solar cell, the output current is a result of the diffusion and drift phenomenon of electrons and holes. The light absorbance is calculated by the transfer matrix methods. The drift-diffusion equations for holes and electrons are given as [121]:

$$J_p = J_p(diff) + J_p(drift) = q\left[\mu_p pE - D_p \frac{\partial p}{\partial x}\right] \tag{2.2}$$

$$J_n = J_n(diff) + J_n(drift) = q\left[\mu_n nE - D_n \frac{\partial n}{\partial x}\right] \tag{2.3}$$

where the μ_p and μ_n are electron and hole mobility, D_n and D_p are electron and hole diffusion constants while E is the electric field in the active layer defined by

$$E = \frac{V - V_{bi}}{d}$$

Where V and V_{bi} are the biasing voltage and built-in potential across the ETL/Active layer junction, and d is the thickness of the active layer.

The continuity equations for holes and electrons under illuminated conditions are given by [33]:

$$q\frac{\partial n}{\partial t}=\left[\nabla \vec{J}_n+qG_n-qR_n\right] \tag{2.4}$$

$$q\frac{\partial p}{\partial t}=\left[\nabla \vec{J}_p+qG_p-qR_p\right] \tag{2.5}$$

For steady-state condition $\frac{\partial p}{\partial t}=\frac{\partial n}{\partial t}=0$, so we have

$$\nabla \vec{J}_n+qG_n=qR_n \tag{2.6}$$

And $$\nabla \vec{J}_p+qG_p=qR_p \tag{2.7}$$

where $G_n(R_n)$ and $G_p(R_p)$ are the electron generation (recombination) and hole generation (recombination) rates, respectively.

To include the effects of defects and traps in various materials on the performance of the PSCs, we have used the SRH recombination model defined by [45].:

$$R=\frac{n.p-n_{\text{int}}^2}{\tau_p(n+n_t)+\tau_n(p+p_t)} \qquad (2.8$$

where τ_p and τ_n are the mean lifetime of the holes and electrons, respectively; R is the recombination rate of the charge carriers; and n_t (p_t) is electron (hole) trap density.

The parameters used for the numerical simulation are listed in Table 2.1. The charge generation rate in the absorbing layer under 1 sun is considered. The amplitude of light intensity in different layers is formulated by using the transfer matrix method, where light intensity, $I(x,\lambda)$, is modeled as a function of position and wavelength. The short-circuit current can be described as [45]:

$$I_{SC,\max}=\iint q\frac{Q(x,\lambda)}{h\upsilon}.dx.d\lambda \tag{2.9}$$

where $Q(x,\lambda)$ is dissipated power per meter square, which can be expressed as

$$Q(x,\lambda)=\alpha(\lambda).I(x,\lambda) \tag{2.10}$$

where α is the absorption coefficient.

The maximum short circuit current ($I_{SC,\ max}$) enumerates us a rough idea for the optimization of layer thickness without affecting the charge transport phenomena in the drift-diffusion model. Maximization of the photon absorption profile in the drift-diffusion model for a particular layer thickness can also be performed to make it more robust. With the help of the photon absorption profile, the generation function for the charge or the exciton continuity equation can be designed depending on the type of solar cell under study.

Table 2.1. The Material Parameters for Numerical Simulation.

Parameter and Units	**TiO_2 NRs** [69], [122]-[124]	**Perovskite** [125]-[127]	**PTAA** [125]
Dielectric Constant (ε_r)	9.0	10	3
Bandgap (eV)	3.2	1.52	3.3
Electron affinity (χ)	4	3.85	2.30
Electron Mobility (μ_n)- $cm^{-2}V^{-1}s^{-1}$	100	2.2	0.002
Hole Mobility (μ_p)- $cm^{-2}V^{-1}s^{-1}$	25	2.2	0.004
CB effective density of states (N_C) (cm^{-3})	2×10^{18}	3×10^{18}	2.2×10^{18}
VB effective density of states (N_V) (cm^{-3})	1.8×10^{18}	3.97×10^{18}	1.8×10^{19}
Electron thermal velocity (cm/s)	1×10^{7}	1×10^{7}	1×10^{7}
Hole thermal velocity (cm/s)	1×10^{7}	1×10^{7}	1×10^{7}

2.4 Results and Discussion

In this section, optical and electrical characterizations of fabricated as well as simulated devices with various thickness variations are presented.

2.4.1 Thin Film Characterization

The hydrothermally grown TNRs samples are first investigated for morphology/composition and crystalline structure using high-resolution scanning emission microscopy (Nova Nano SEM 450, FEI, USA) with in-situ energy dispersion spectroscopy (EDS) (EDAX Inc.) and X-ray diffractometer (XRD, Miniflex, Rigaku, Japan) respectively. The photoemission spectra of perovskite thin film is measured using photoluminescence (PL) spectroscopy (FLS 980 from Edinburgh Instruments, UK). The optical absorption in TNRs and perovskite thin film has been measured using a thin film analyzer (from Filmetrics, USA).

It is found that the grown TNRs have uniform distribution on the surface, as shown in figure 2.3 (a), and desire elemental composition, as shown in figure 2.3 (b). The optimized TNRs with a growth time of 3.5 hour having an average length and average diameter around ~500 nm and ~70 nm were observed from the HRSEM image. The XRD patterns also confirm the formation of good quality crystalline TNRs with mostly rutile phase, as shown in figure 2.4 (a). The perovskite film exhibits single peak emission spectra at an excitation wavelength of 450 nm, as shown in figure 2.4 (b). The morphology of perovskite film on the TNRs is shown in figure 2.5 (a). The cross-sectional image is taken to analyze the thickness of individual layers of FTO/TNRs/Perovskite structure. It is found that the TNRs have an average length of 500 nm and perovskite film has a thickness of ~350 nm, as shown in figure 2.5 (b).

The optical absorption in the optimized TNRs is shown in figure 2.6 (a), which is comparable to the simulated absorption spectra obtained in the SCAPS-1D simulation tool. It is found that the optical band gap (Eg) and absorbance coefficient (α) have a relation obtained from the tau plot as below [128]:

$$\alpha h\upsilon = A\left(h\upsilon - E_g\right)^m \tag{2.11}$$

where $\alpha = 2.33\log\left(T/_d\right)$, T is transmittance, d is the sample thickness, $h\upsilon$ = *1240(incident light (nm))*, and m is a constant. The bandgap of the TNRs is estimated as ~3.2 eV from the experimentally obtained transmittance. The experimental and simulation absorbance spectra of the perovskite layer are shown in figure 2.6 (b).

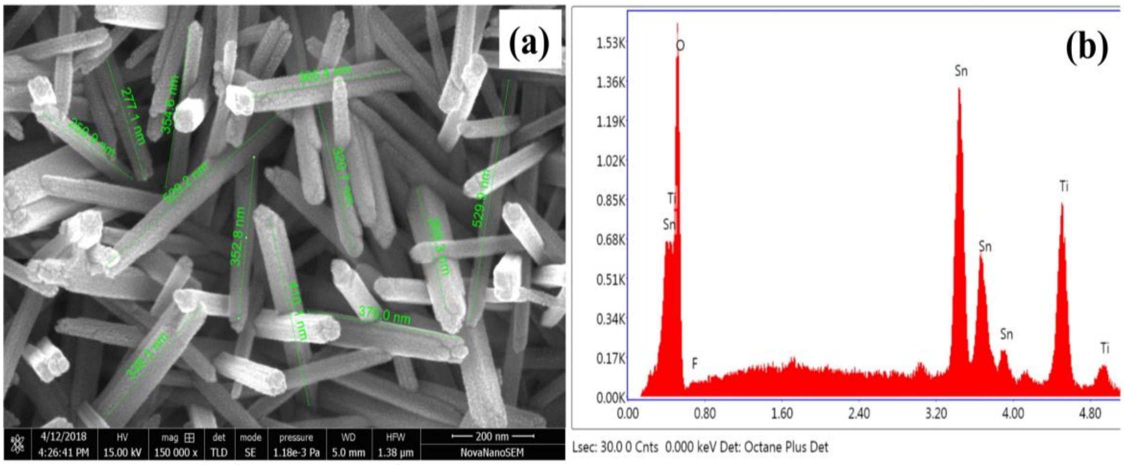

Figure 2.3: (a) HRSEM image of TNRs and (b) EDS image of TNRs.

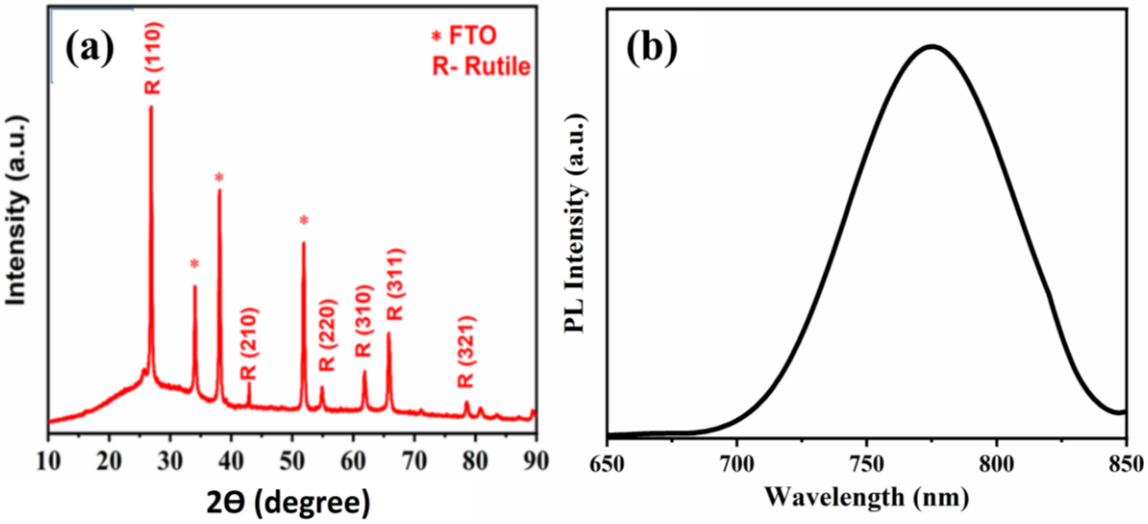

Figure 2.4: (a) XRD pattern of hydrothermally synthesized TNRs and (b) PL emission spectra of perovskite thin film.

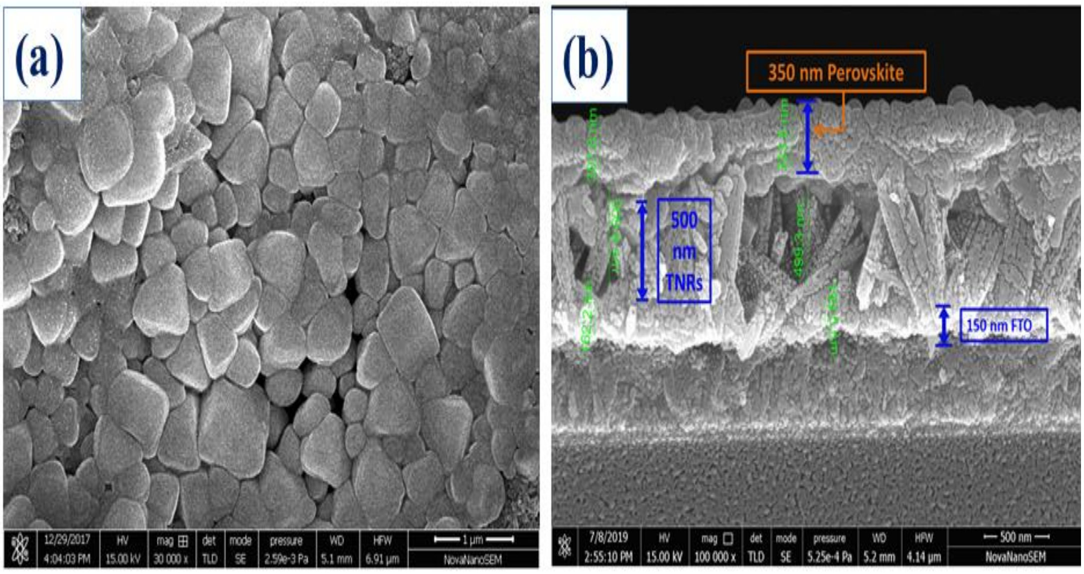

Figure 2.5: HRSEM image of (a) perovskite thin film surface (b) Cross-sectional view of PSC structure without metal electrode.

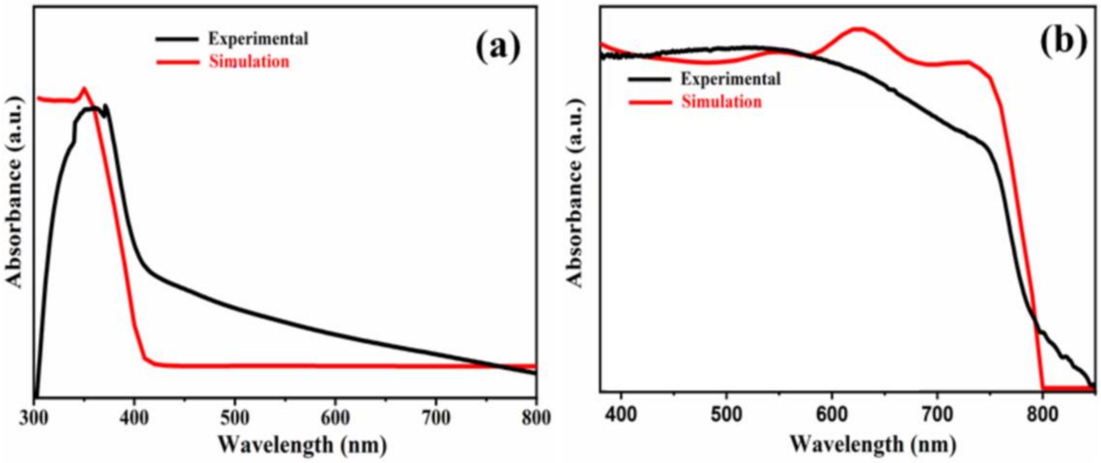

Figure 2.6: (a) Absorbance spectra of hydrothermally synthesized and simulated TNRs on FTO coated glass substrate, (b) Absorbance spectra of synthesized and simulated perovskite thin film.

2.4.2 Solar Cell Characterization

The current density (*J*)-voltage (*V*) characteristics of the fabricated PSCs have been compared with the simulation results in figure 2.7 (a)-(c) for different thicknesses of the TNRs-based ETL of the device. The standard solar light is obtained from the solar simulator (AAA150 from PET, USA). The solar cell parameters (J_{SC}, V_{OC}, *FF*, and η) and external quantum efficiency (EQE) are obtained from the *J*-*V* characteristics. The

TNRs with smaller lengths in the ETL reduce the shunt resistance (which, in turn, increases the dark current) while larger lengths of TNRs enhance the recombination of the photo-generated carriers (which, in turn, reduces the photocurrent) [129], [130]. It is observed that TNRs with lengths ~500 nm result in optimum performance in PSCs considered in the present study. The efficiencies for 200, 350, 500, 650, and 800 nm lengths of TNRs are measured as 13.47, 14.65, 15.04, 11.70, and 10.73%, respectively, in ambient conditions. The efficiencies are slightly lower than other reported works for measurements under a robust open-air atmosphere [131]. A part of perovskite materials breaks into lead iodide and methylammonium iodide in the presence of atmospheric moisture, which limits the efficiency of the PSCs [132]. We have carried out the measurements in the open atmosphere to demonstrate the operation of the PSCs in actual conditions rather under controlled environments. The experimentally estimated performance parameters are compared with the corresponding values obtained from the simulated results in Table 2.2. The simulation results are found to be in close proximity to the experimental data. It may be noted from Table 2.2 that J_{SC} is decreased with increased thickness of the TNRs-based ETL layer due to the possible increase in the series resistance of the solar cell. The open-circuit voltage is reduced from 1.06 ± 0.01 V to 0.95±0.02 V when the thickness of the ETL is increased from 500 nm to 800 nm, possibly due to enhancement in the recombination of charge carriers in nanorods or limitation of diffusion length of charge carriers. As a consequence, overall, the *PCE* is decreased with the increase in ETL layer thickness above 500 nm. Further, the thickness of different layers changes the electric field in the layers, which, in turn, affects the drift current of the device. The diffusion current also depends on the thickness of the active layer. If the thickness of the active layer is less than the diffusion length of the electron (hole), all photo-generated electrons (holes) contribute to the diffusion current.

Otherwise, a part of the photo-generated carriers is lost due to recombination, which affects the device performance.

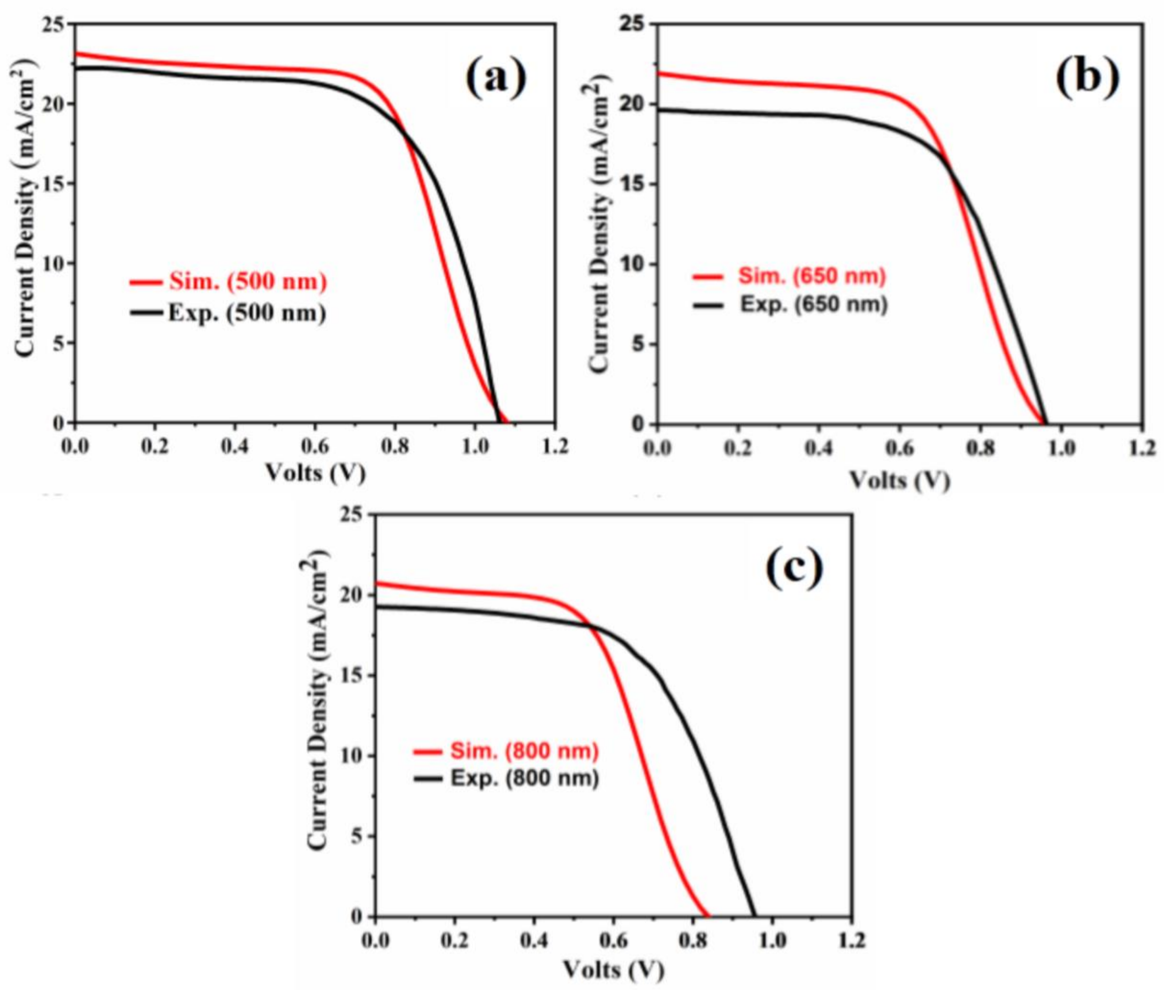

Figure 2.7: J-V curve of fabricated and simulated PSCs with (a) 500 nm TNRs, (b) 650 nm TNRs, (c) 800 nm TNR.

Table 2.2 shows that the current density decreases when the ETL thickness increases. The increase in the ETL thickness decreases the light intensity entering into the active layer, which reduces the photon absorption and hence increases the series resistance of the solar cell. The open-circuit voltage of the solar cell is given by [45]:

$$V_{OC} = \frac{KT}{q} \ln(\frac{J_{SC}}{J_0}) \tag{2.12}$$

The increased ETL thickness enhances the recombination of carriers. This increases J_0 and reduces V_{OC}. Thus, internal power consumption increases with increased ETL thickness, which affects the fill factor (FF) and the PCE (η) of the PSC. The relationship between FF and PCE is given by [133]:

$$FF = \frac{P_m}{J_{SC}.V_{OC}.A} = \frac{J_m.V_m}{J_{SC}.V_{OC}} \tag{2.13}$$

$$\eta = \frac{FF.J_{SC}.V_{OC}.A}{P_{in}} \tag{2.14}$$

where P_{in} is the incident power from the solar simulator, A is the area of the top electrode of the fabricated PSC and J_m, V_m, and P_m are the maximum current density, maximum voltage, and maximum power obtained from the device. The thickness of the ETL needs to be chosen in such a way that the diffusion length of charge carriers is larger than the thickness of the ETL. For high power conversion efficiency, a 500 nm optimum thickness of ETL is obtained for our proposed structure.

Table 2.2. Fabricated and Simulated Results for Different ETL of the PSCs

		ETL Thickness (nm)		**Performance Parameters**			
ETL Defect Density ($1/cm^3$)	Active Layer Defect Density ($1/cm^3$)	(TNRs Growth Time)		V_{OC}	J_{SC}	FF	η
10^{13}	10^{7}	500 (3.5 Hour)	Exp.	1.06 ± 0.01	22.19 ± 0.2	0.63±0.01	15.04±0.03
			Sim.	1.07	23.71	0.63	15.69
10^{14}	10^{8}	650 (5 Hour)	Exp.	0.96±0.02	19.62±0.2	0.62±0.01	11.70±0.05
			Sim.	0.96	21.91	0.59	12.58
10^{15}	10^{9}	800 (7 Hour)	Exp.	0.95±0.02	19.26±0.2	0.58±0.02	10.73±0.05
			Sim.	0.84	20.71	0.55	9.67

The EQE is computed by the following expression [134]:

$$EQE = 1240 \times \frac{R}{\lambda} \times 100 \tag{2.15}$$

where R is the responsivity defined as

$$R = \frac{I_{Ph}}{P_{in}} \tag{2.16}$$

where P_{in} and I_{Ph} are incident power and output photocurrent of the device at the wavelength λ of the incident light. The external quantum efficiency (EQE) of the fabricated and simulated device is compared in figure 2.8. A close matching is observed for the optimized thicknesses of 500 nm, 100 nm, and 350 nm of the ETL, HTL, and active layers, respectively.

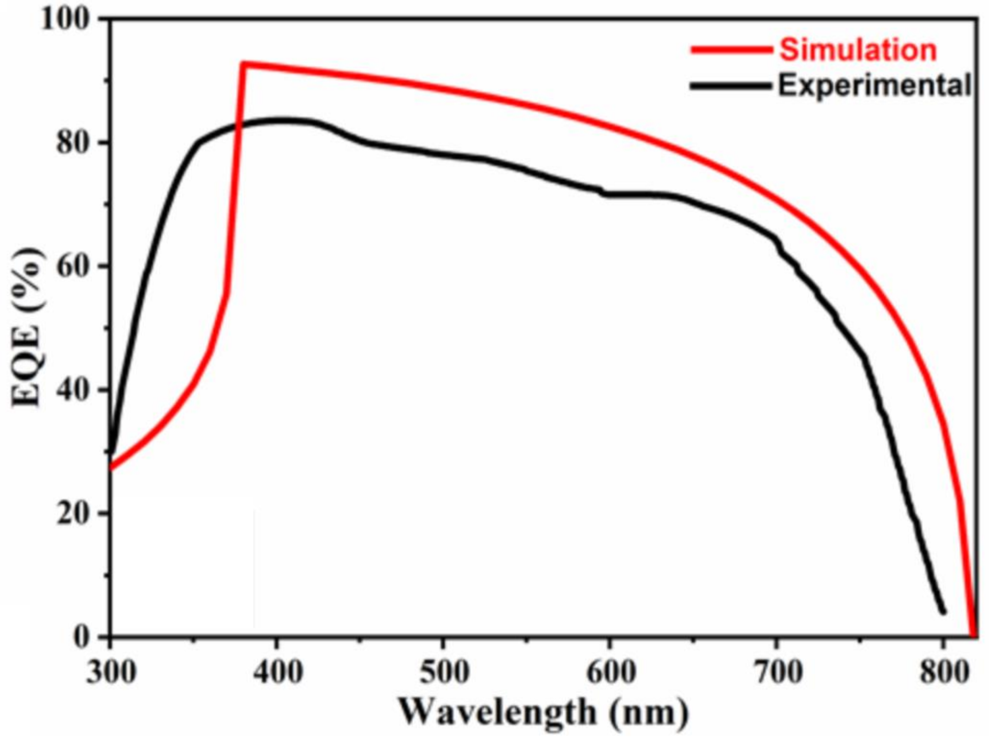

Figure 2.8: External quantum efficiency of fabricated and simulated PSCs with 500 nm ETL, 350 nm active layer, and 100 nm HTL.

2.5 Conclusion

This chapter examines the FTO/TNRs/Perovskite/PTAA/Pd structure-based PSC, where

TNR acts as the ETL, PTAA as the HTL, and hybrid perovskite ($CH_3NH_3PbI_3$) as the active layer of the device. The effects of TNRs thickness on the performance parameters have been investigated using fabricated and simulated solar cells. The morphological, structural, electrical, and optical properties of FTO/TNRs/Perovskite/PTAA/Pd structure have been analyzed for their suitability in solar cell applications. The simulation tool has been explored for optimizing various parameters of the PSC. All the experimental measurements have been carried out in the ambient-air condition. The PCE of the PSC is observed to be decreased for ETL thickness above 500 nm. The optimum values of the PSC parameters V_{OC}, J_{SC}, FF, and PCE are obtained for the thicknesses of 500 nm, 100 nm, and 350 nm of the ETL, HTL, and the active layer, respectively. Optimized simulated values of J_{SC}, V_{OC}, FF, and PCE are obtained as 23.71 mA/cm^2, 1.07 V, 0.63, and 15.69%, respectively, against their corresponding experimentally measured values of 22.19 mA/cm^2, 1.06 V, 0.63, and 15.04%, respectively for the aforementioned optimized thicknesses of the ETL, HTL, and the active layer. The EQE of the simulated and experimental devices matches well for the optimum values of different layers. The close proximity of the simulated electrical and optical characteristics with the experimental results confirms that the TCAD tools can be effectively explored for other PSC structures. The result shows that TNRs thickness also plays a very significant role in the solar cells performance.

CHAPTER 3

Effects of Solvothermal Etching and $TiCl_4$ Treatment of TiO_2 Nanorods (TNRs) ETL on the Performance Characteristics of FTO/TNRs/$CH_3NH_3PbI_3$/Spiro-OMeTAD/Pd Solar Cells*

Contents

*Part of this work has been published as:

1. Jarwal, Deepak Kumar, et al. "Efficiency improvement of TiO_2 nanorods electron transport layer based perovskite solar cells by solvothermal etching." *IEEE Journal of Photovoltaics* 9.6 (2019):1699-1707.

CHAPTER 3

Effects of Solvothermal Etching and $TiCl_4$ Treatment of TiO_2 Nanorods (TNRs) ETL on the Performance Characteristics of FTO/TNRs/$CH_3NH_3PbI_3$/Spiro-OMeTAD/Pd Solar Cells

3.1 Introduction

The effect of the TiO_2 nanorods (TNRs) based ETL thickness on the performance parameters of FTO/TNRs/$CH_3NH_3PbI_3$/PTAA/Pd perovskite solar cells (PSCs) has been discussed in Chapter-2. It may be mentioned that the morphology and shape of the TNRs surface play crucial roles in the performance improvement of the PSCs [135]. Thus, an attempt has been made in this chapter to improve the performance of the FTO/TNRs/$CH_3NH_3PbI_3$/Spiro-OMeTAD/Pd by solvothermal etching and $TiCl_4$ treatment of the hydrothermally grown TNRs based ETL by the low-cost hydrothermal method considered in Chapter-1 [136]. To show the robustness of the PSCs, both the fabrication and measurements have been carried out at room temperature and the high humid open-air environment with a relative humidity of ~65% or above. The top of TNRs in the ETL has been split into small nanowires and nanotubes by the solvothermal etching of the TNRs to speed-up electron transportation, enhance porosity, and increase the effective surface-to-volume ratio of the ETL [81]. The TNRs have been finally treated with $TiCl_4$ to improve the fill factor (FF) and open-circuit voltage (V_{OC}) of the hybrid PSCs under study [63]. The outline of the rest of the present chapter is as follows:

Section 3.2 contains the experimental detail for the synthesis of materials and fabrication of PSCs. The measurement of different solar parameters and their discussion are presented in Section 3.3. Finally, the finding and observations of the present chapter are summarized in Section 3.4.

3.2 Experimental Details

This section deals with the fabrication and characterization details of the TNRs ETL based hybrid PSC solar cells on fluorine-doped tin oxide (FTO) coated glass substrates. 4-tert-butylpyridine, lithium bis (trifluoromethanesulfonyl)-imide, and Spiro-OMeTAD were purchased from Ossila (UK).

3.2.1 Preparation of Electron Transport Layer (ETL)

TiO_2 NRAs used for the ETL were grown on a cleaned FTO coated substrate through multiple steps, as demonstrated in Figure 3.1. A seed layer (~20 nm) of TiO_2 nanoparticles was first deposited on FTO coated substrate to achieve fast nucleation for the growth of isolated and uniform TNRs [137]. Then TiO_2 NRAs were grown on the seed layer by the hydrothermal method under optimized time and temperature. Solvothermal etching of TiO_2 NRAs was then performed to enhance the effective surface area of the ETL. Finally, $TiCl_4$ treatment of the NRAs was performed for removing the traps and voids in the TiO_2 NRAs. Four major steps in the fabrication of TiO_2 NRA based ETL is described below:

1) TiO_2 Seed Layer Deposition

A solution of TiO_2 nanoparticles (NPs) was prepared from TTIP by modifying the synthesis method reported in [138]-[139]. First of all, 740 µl of TTIP and 70 µl of HCl (~35 wt% concentration) are mixed in 2.5 ml ethanol separately. Diluted HCl solution was added drop by drop to the diluted solution of TTIP under magnetic stirring for 3 hours till the mixed solution was turned to opaque in color at room temperature. Finally, the prepared TiO_2 NPs solution was filtered by PVDF filter to achieve colloidal TiO_2

NPs of uniform size. The FTO coated glass substrates of 15 mm×45 mm was cleaned ultrasonically using soap solution, DI water, acetone and iso-propanol sequentially for 15 minutes each. The substrates were then dried at 100^{o}C and processed for plasma cleaning for 10 minutes. After the plasma cleaning of the FTO substrates, a seed layer (~ 20 nm thicknesses) of TiO_2 NPs was grown on the cleaned FTO substrates by spin coating of the colloidal TiO_2 NPs at 4000 rpm. The TiO_2 NPs coated FTO substrates were then annealed at 450^{o}C for 1 hour to prepare the compact layer (C-TiO_2) to block holes in the hybrid PSC.

2) *TiO_2 Nanorod Grown by Hydrothermal Process*

TiO_2 nanorods were grown hydrothermally on spin-coated TiO_2 seed layer (C-TiO_2) by using a Teflon lined autoclave at 170^{o}C through a modified synthesis route [137]. First of all, TTIP of ~560 µl was added to DI water, and the obtained white precipitate at the bottom of the solution was dissolved further in the solution of HCl (35 wt% concentration) and DI water (1:1 ratio). The mixed solution was put in a Teflon lined cylinder and the seed layer deposited FTO substrates (with FTO coated surface in the backside) were placed tilted in the TTIP solution of the cylinder in such a way that the TiO_2 NRA could grow on FTO coated surface in the downward direction as shown in Figure 3.1 (c). The Teflon lined cylinder was then sealed properly and kept into an autoclave, which was heated in the digital muffle furnace (Escon lab. Inst, India) at 170^{o} C for 3 hours. Since the length and diameter of TNRs are dependent on the growth time and temperature, the above temperature and duration were optimized for the desired length and diameter of the NRs in the present study. Then the autoclave was cooled down to room temperature for getting TiO_2 NRs of ~450 nm long in 3 hours. The glass substrate with TNRs grown on the FTO coated side was ringed in DI water, washed in ethanol and dried at 100^{o}C. Finally, the samples with TiO_2 NRs were annealed at 450^{o}C for 1.30 hours in the air environment for preparing the ETL layer.

3) Solvothermal Etching of TiO$_2$ Nanorods

The FTO coated glass substrates with TiO$_2$ nanorods (TNRs) were processed for solvothermal etching of the TNRs [140]. The TNRs based substrates were placed in an etching solution prepared by mixing of 15 ml concentrated HCl (35 wt%) and 15 ml DI-water in a Teflon lined cylinder.

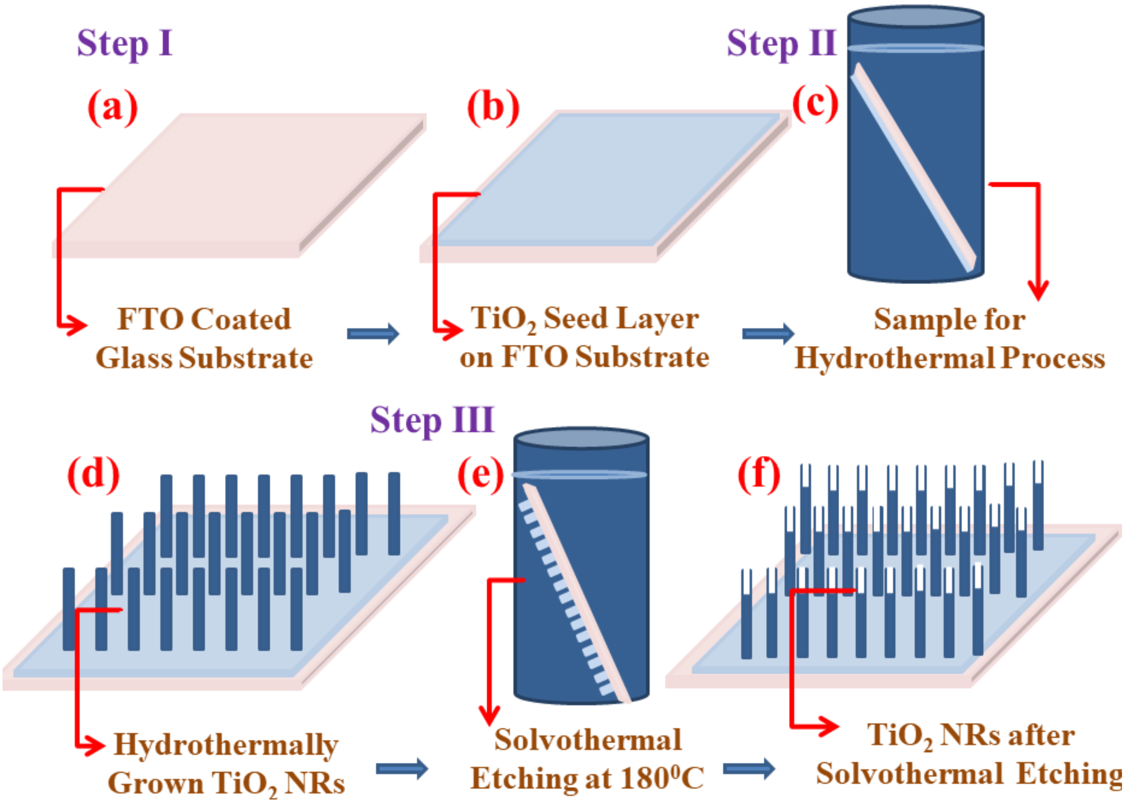

Figure 3.1: (a) FTO coated glass, (b) TiO$_2$ seed layer on FTO coated glass, (c) Hydrothermal Process at 170^{0}C in Teflon lined cylinder, (d) TNRs after hydrothermal process, (e) Solvothermal etching of TNRs at 180^0 C and (f) TiO$_2$ NRs after solvothermal etching.

The cylinder was placed in the autoclave, which was heated in the digital muffle furnace at a temperature of 180^o C for an optimized duration of 4-5 hours. The autoclave was then cooled down to the ambient temperature to achieve the solvothermally etched TNRs on the FTO coated glass substrates. The reaction for solvothermal treatment is given as follows [81]:

$$TiO_2 \Leftrightarrow Ti\,\text{(IV) complex} \tag{3.1}$$

This dissolution reaction is dynamic in nature, which results in the formation of TiO_2 hollow rectangular structure (nanotubes) with filaments like appearance at the top with small nanoparticles.

4) $TiCl_4$ Treatment to Etched TiO_2 Nanorod

The substrates containing solvothermally etched TNRs were processed for $TiCl_4$ treatment to remove trap states and voids present in the TNRs based ETL. For $TiCl_4$ treatment, the substrate was immersed in a 40 mM aqueous solution of $TiCl_4$ for 30 minutes at the optimized temperature of 70^{o}C, followed by washing with DI water to remove excess salt, and annealed at 500°C for 1 hour [81].

3.2.2 Solar Cell Fabrication

The hybrid perovskite layer was obtained by two-stage spin-coating of organic and inorganic precursor solutions prepared by dissolving 462 mg of PbI_2 in 1 ml of DMF solvent and 10 mg of methylammonium iodide (CH_3NH_3I) in 1 ml isopropanol solvent, respectively. The PbI_2 solution was heated at 70°C with stirring for 1 hour and then used to deposit on the TNRs by spin coating at 3000 rpm for 40 seconds. The sample was then heated on the hot plate at 70^{o}C for 10 minutes. The CH_3NH_3I solution was then deposited on the PbI_2 layer as a second precursor at 3000 rpm by spin coating to complete the perovskite film. Toluene was used as an anti-solvent during the spin coating of CH_3NH_3I for improving the surface morphology of the perovskite film. Toluene was also used to improve the conductivity of the hybrid perovskite film by removing the voids and residues in methylammonium and halide ions [141]. The substrate containing the hybrid perovskite film was heated at 100 ^{o}C for 30 minutes for improving its crystalline structure. Since perovskite behaves as conductive material, a thick (~100 nm) capping layer or hole transport layer (HTL) of p-type Spiro-OMeTAD (i.e. hole transport material (HTM)) was grown on the perovskite layer by spin coating method to avoid the possibility of short-circuiting between perovskite layer and top electrode of the solar cell. The HTM solution was prepared by mixing of 17.5 μl lithium bis (trifluoromethanesulfonyl)-imide [Li-TFSI] (520 mg/ml in acetonitrile), 28.8 μl of tert-butylpyridine (4-TBP), and 72.3 mg of Spiro-OMeTAD in 1 ml of chlorobenzene. The HTM solution of ~40 µl was dispersed onto perovskite and then used for spin coating at 2000 rpm for 30 seconds to achieve a ~100 nm capping layer. The capping layer also helps in improving the performance by making a balance between the shunt resistance and series resistance of the solar cell [40].

To complete the fabrication of the PSC under study, a ~ 60 nm film of palladium was deposited for top electrode by thermal evaporation (FL400, Hind High Vacuum Ltd, India with in-built thickness monitor: SQM-160, INFICON) at a vacuum of $\sim 2\times 10^{-6}$ mbar. The complete fabrication steps of three types of PSCs- Device A: PSC with simple TNRs based ETL without $TiCl_4$ and solvothermal etching; Device B: PSC with only $TiCl_4$ treated TNRs based ETL but no etching; and Device C: PSC using TNRs ETL treated with both the $TiCl_4$ and solvothermal; is illustrated in Figure 3.2. The block diagram of as-fabricated PSCs after solvothermal etching is shown in Figure 3.3 (a). The energy level of various material layers in the PSC structure is analyzed through the energy band diagram shown in Figure 3.3 (b). Note that electrons and holes after separation of the photo-generated electron-hole pairs travel in opposite directions with the help of ETL and HTL.

3.2.3 Material and Device Characterization

The crystalline structure of the prepared TNRs grown on FTO coated glass was characterized by X-ray diffractometer (XRD, Miniflex, Rigaku, Japan) by using Cu-Ka at a wavelength of $\lambda = 1.5406$Å for an operating voltage of 45 kV and current of 40 mA. The structure and crystallinity of TNRs are analyzed using transmission electron microscopy (TEM) (FEI G2 T20 STWIN). The elemental composition of the sample was evaluated by energy dispersion spectroscopy (EDS) (EDAX Inc.), and the surface morphology of the sample was recorded by high-resolution scanning emission microscopy (HRSEM) (Nova Nano SEM 450, FEI, USA). The roughness of the TiO_2 layer and perovskite layer is analyzed by atomic force microscopy (AFM) (NTEGRA Prima, NT-MDT Service & Logistics Ltd.). The transmittance and absorbance spectra were obtained from the dual-beam UV-Vis

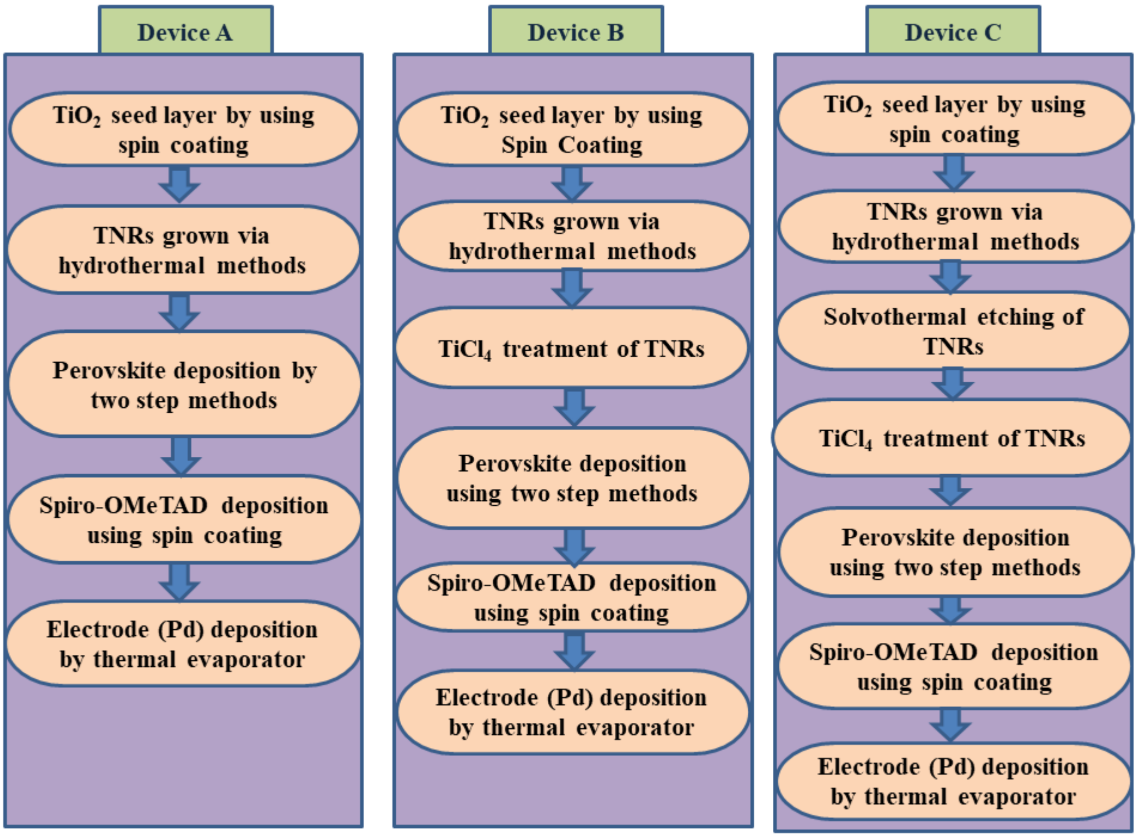

Figure 3.2: Fabrication steps used for device A, B and C.

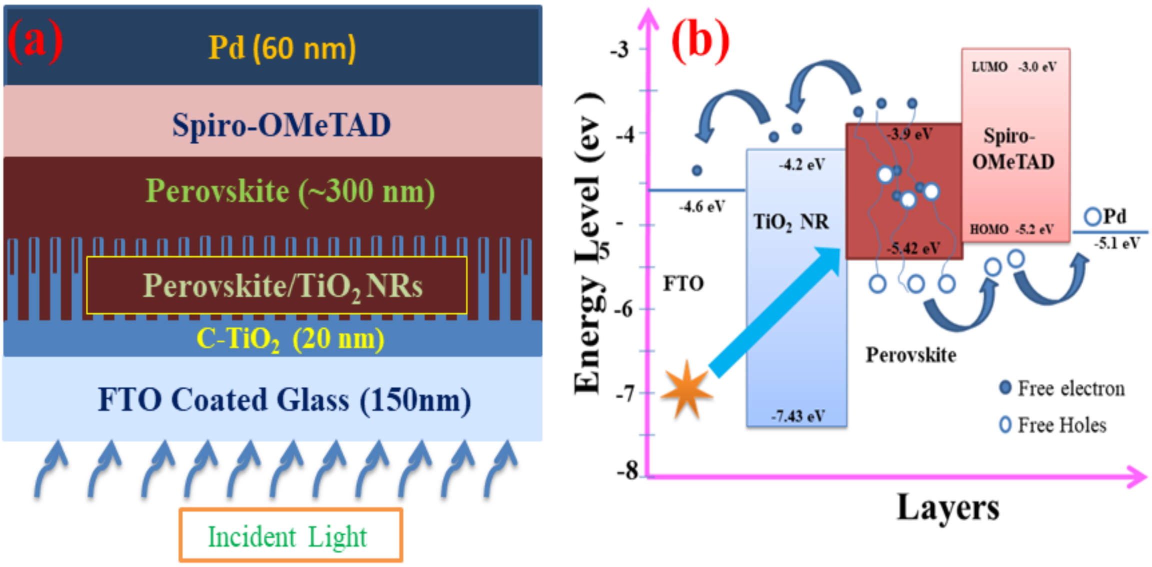

Figure 3.3: (a) The device structure of PSC after solvothermal etching of TiO_2 NRs and (b) Schematic representation of the energy band diagram of PSC.

spectrophotometer (Jesco, V-750, Japan). The photoluminescence measurement is performed using spectrometer (FLS 980 from Edinburgh Instruments, UK). The electrical measurement including current-voltage (*IV*) and impedance of the solar cells was performed using probe station attached to the semiconductor parameter analyzer (B1500A, Keysight). Solar light spectrum of 100 mW/cm^2 and 1.5 AM G is obtained from solar simulator (PET corp., USA). The external quantum efficiency (EQE) was measured from the experimental setup of monochromator (SP2150i, Princeton Instruments, USA) connected with light source (Princeton Instruments) and digital multimeter (DMM, 34410A, Agilent). The power of the incident light and output current of the device at different wavelength was measured using power meter (PM100D, Thorlabs) and DMM, respectively, connected through LabVIEW software.

3.3 Results and Discussion

The measured solar characteristics and parameters are presented in this section. Further discussion on the solar cell characteristics is also listed in this section.

3.3.1 Thin Film Characterization

X-ray diffraction analysis was used to investigate the crystallinity and phase of the TiO_2 film. The diffractogram of the TNRs is shown in Figure 3.4 (a) from 5 degrees to 80 degree for a step of 0.0200 degree. It is observed that grown TNRs have both anatase and rutile phases. The experimental XRD pattern is well-indexed to the tetragonal rutile phase (JCPDS No. 21-1276). Stronger diffraction peaks at 26.90 degree, 36.49 degree and 54.89 degree over two minor peaks (at 63.15 degree and 70.17 degree) of the anatase phase confirm rutile as the majority phase in the TNRs. Two spurious diffraction peaks at 42.84 degree and 71.08 degree are also observed. The XRD pattern of the TNRs before and after the solvothermal treatment exhibit the same diffraction peaks as shown by the Wan et al.[81]. This clearly rules out any possibility of phase transformation or any new phase formation during the solvothermal etching process. The elemental composition analysis through energy dispersive spectroscopy (EDS) is shown in Figure 3.4 (b).

The surface morphology and structure of individual TNR obtained by TEM analysis is shown in Figure 3.5. The bright field images in Figure 3.5 (a) and (c) show the diameter of TNRs before and after solvothermal etching of TNRs. The selected area electron diffraction pattern (SAED) in Figure 3.5 (b) and (d) confirm that TNRs are of single crystalline rutile phase. Figure 3.5 (c) also shows small TiO_2 nanoparticles with TNRs which could have formed due to dissolution and reprecipitation during solvothermal etching treatment.

The scanning electron microscopy (SEM) images of TiO_2 NRs are shown in Figure 3.6. The SEM images of the TNRs before the solvothermal etching in Figure 3.6 (a) and (b) show that TNRs are uniformly distributed over the FTO substrate having average length around ~ 450 nm and an average diameter of ~150 nm. The length and diameter are also measured from the cross-sectional HRSEM shown in the inset of Figure 3.6 (b). The surface morphology and density of TNRs can be optimized by changing the concentration of precursor (TTIP) in the solution. The length and diameter of TNRs are dependent on the temperature and time of the hydrothermal process. It is also observed that there is a significant space between any two TNRs, which can be explored to place the perovskite material of the PSC under study. The solvothermal etching improves the net surface area of the TNRs by splitting their top surfaces into small nanowires and hollow rectangular structures in the form of nanotubes ~70 nm diameter and ~ 100 nm depth, as shown in Figure 3.6 (c) and (d). The inner diameter and depth of the rectangular hollow voids can be increased by enhancing the etching time and temperature. The surface morphology and grain of the perovskite layer deposited on TiO_2 NRs (TNRs) at room temperature and 65% relative humidity are shown in Figure 3.6 (e) and (f). The surface roughness and grain boundaries of the TNRs layer before and after the solvothermal treatment are analyzed from AFM images shown in Figure 3.7 (a)-(b) and 3.7 (c)-(d), respectively.

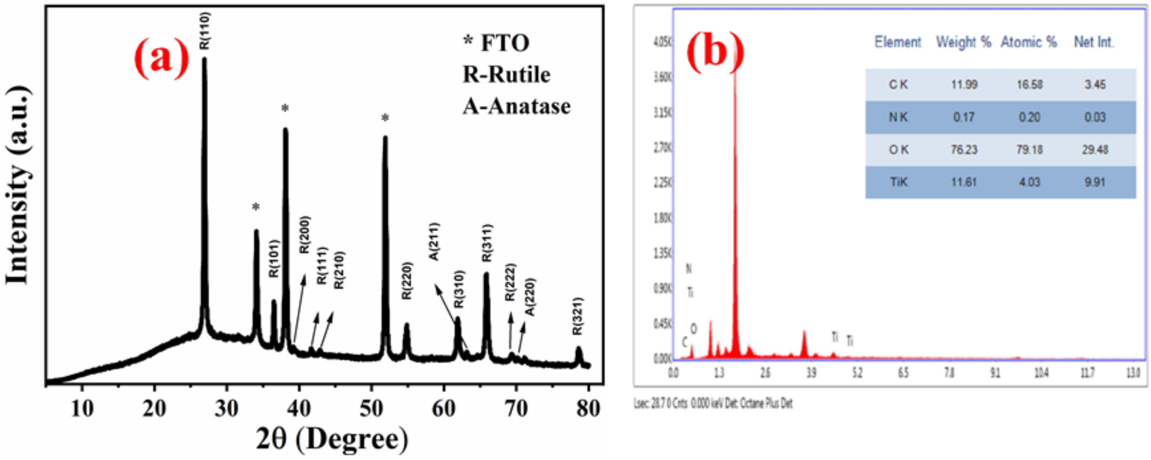

Element	Weight %	Atomic %	Net Int.
C K	11.99	16.58	3.45
N K	0.17	0.20	0.03
O K	76.23	79.18	29.48
TiK	11.61	4.03	9.91

Figure 3.4: (a) XRD analysis of TiO_2 NRs annealed at 450^0 C. (b) Energy dispersive spectroscopy (EDS) and elemental composition of TNRs.

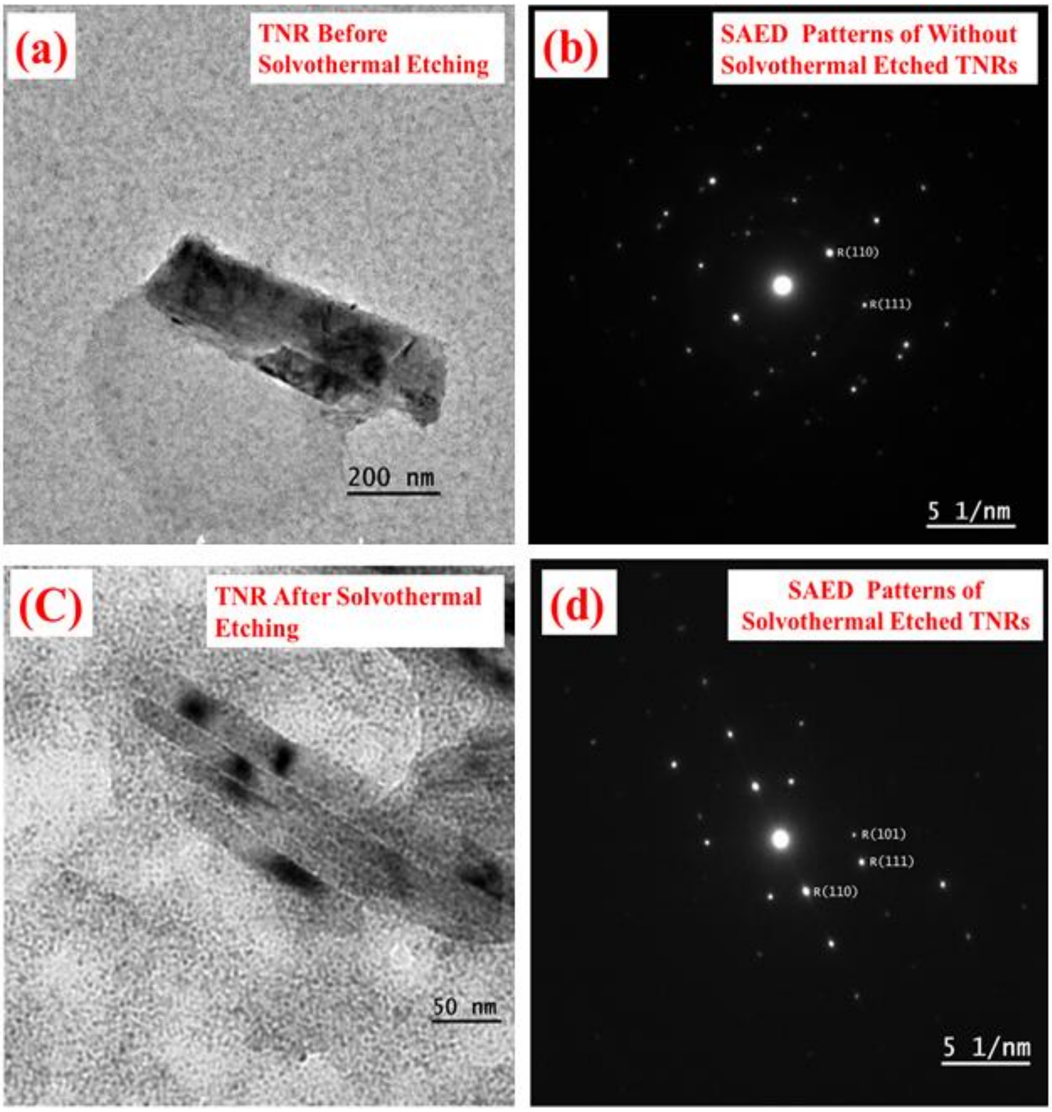

Figure 3.5: (a) and (c) are the TEM images of pristine rutile TNRs and TNRs after solvothermal etching respectively. Figure (b) and (d) are the selected area electron diffraction patterns corresponds to Figure (a) and (b) respectively.

The AFM images of the perovskite layer deposited on the solvothermally etched TNRs layer have been shown in Figure 3.7 (e)-(f). The root-mean-square (RMS) surface roughness of TNRs before solvothermal etching, TNRs after solvothermal etching, and perovskite layer on TNRs are measured as ~100 nm, ~112 nm, and ~56 nm, respectively. The roughness profile confirms that the TNRs layer after solvothermal etching has larger surface roughness than that of the TNRs layer without etching. In other words, the overall active surface area of the device is increased by solvothermal etching, which can be explored for enhancing the efficiency of PSC. The AFM results are found to be agreed with the SEM results shown in Figure 3.6.

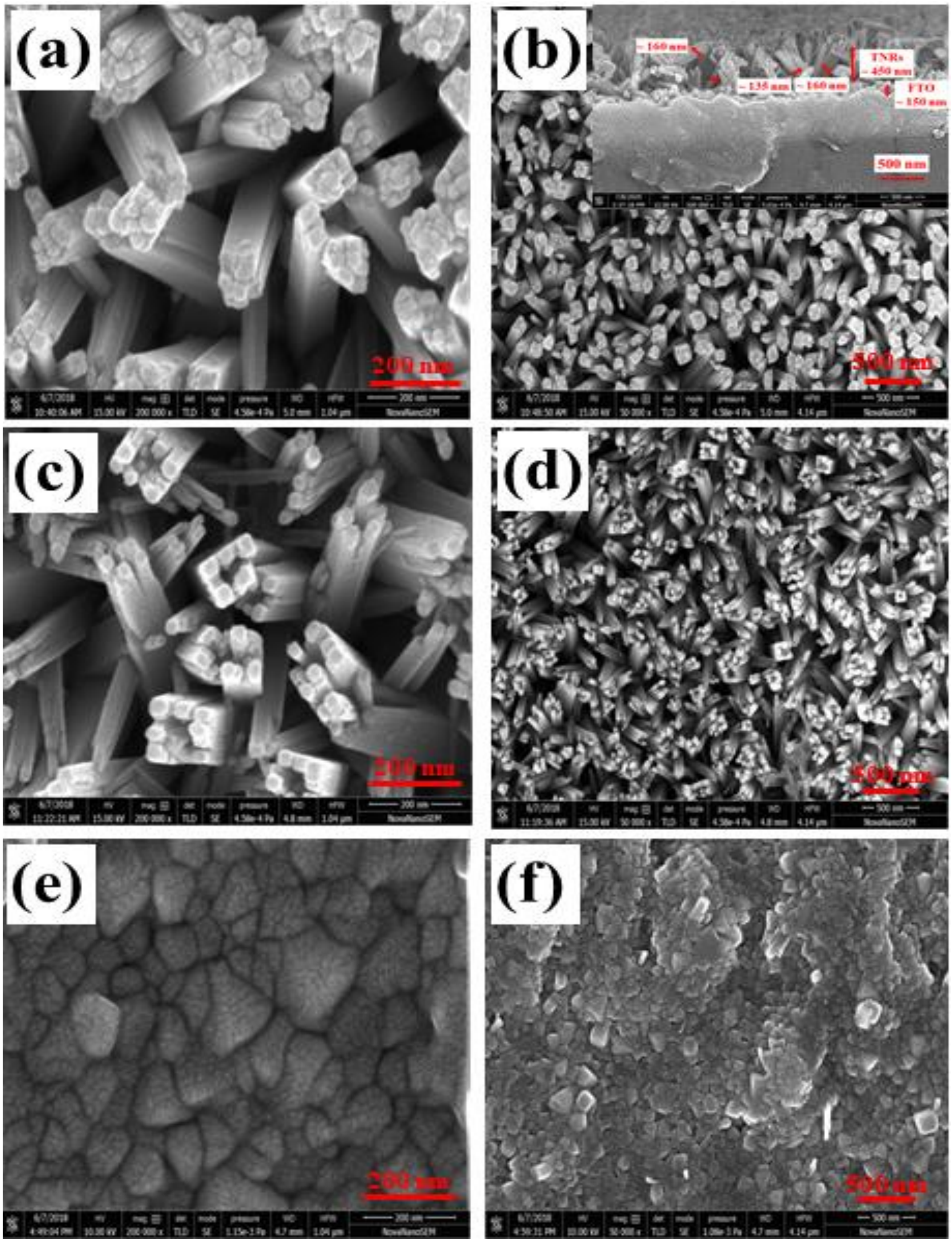

Figure 3.6: Top view SEM image of TNRs annealed at 450^0 C in ambient environment before solvothermal etching: (a) 200 nm scale, (b) 500 nm scale (Inset of Figure 3.6 (b) shows the cross-sectional image of TNRs at 500 nm scale); after solvothermal etching: (c) 200 nm scale, (d) 500 nm scale. Top SEM image of perovskite thin film deposited on solvothermal etched TNRs (e) 200 nm scale and (f) 500 nm scale.

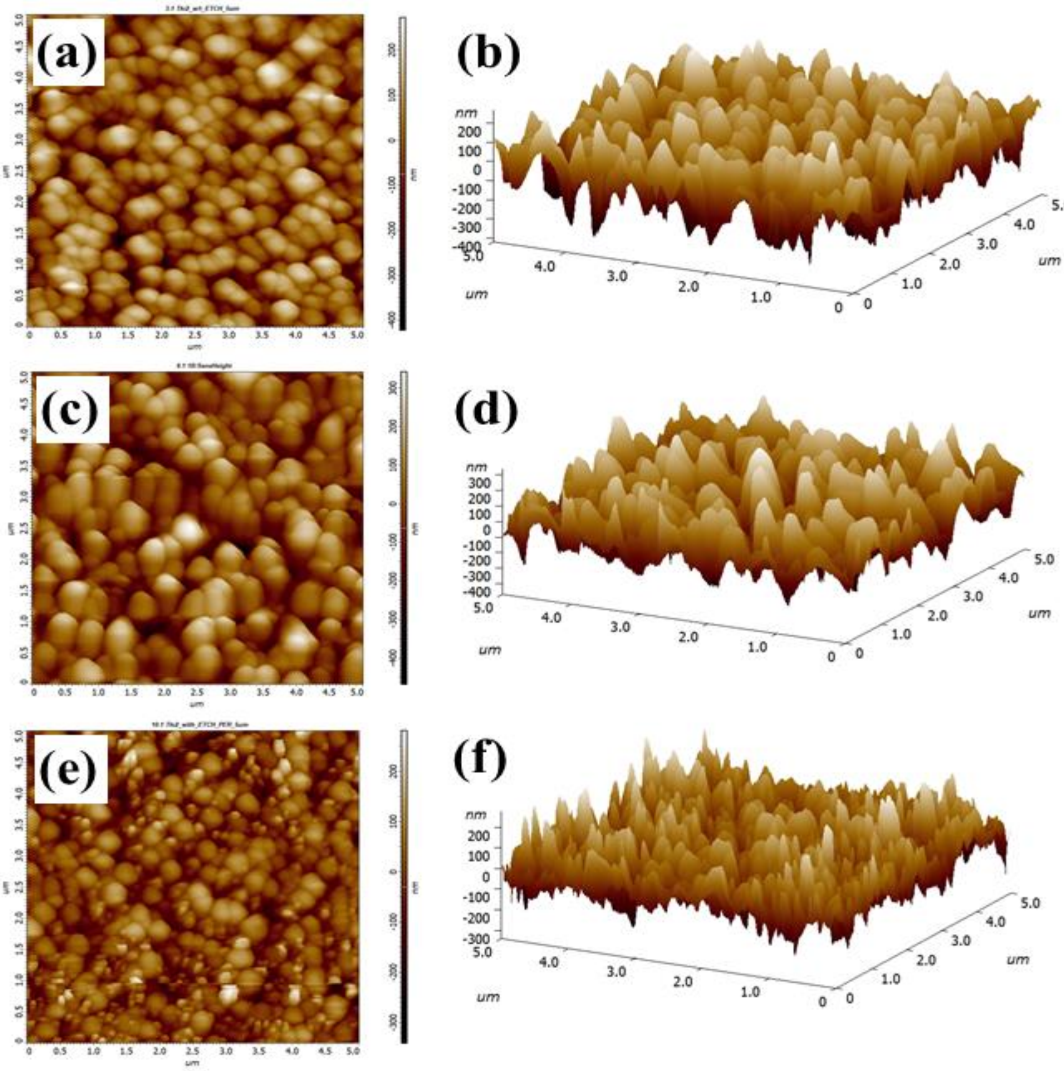

Figure 3.7: AFM image of TNRs without solvothermal etching (a) 2D and (b) 3D. AFM image of TNRs with solvothermal etching (c) 2D and (d) 3D. AFM image of perovskite film deposited on etched TNRs (e) 2D and (f) 3D.

The transmittance (T) spectra of TNRs without solvothermal etching and with solvothermal etching are shown in Figure 3.8 (a). Note that absorption in TNRs can be written as

A=log (1/T) [143]. Similar transmittance spectra pattern confirms that no change in phase of the TNRs is introduced by the solvothermal etching process except change in their effective surface area as also supported TEM image and SAED pattern of TNR (as shown in Figure 3.5). Also, the TNRs along with nanoparticles (as confirmed by TEM image) may further enhance the surface to volume ratio of the TNRs layer, which enhances the absorbance. A step-change in the transmittance spectra observed at ~405 nm due to an abrupt reduction in absorption near the optical bandgap edge of TiO_2. The value of optical band gap can be calculated from the tauc relationship [143]:

$$\alpha h\upsilon = \mathrm{A}(h\upsilon - E_g)^m \tag{3.2}$$

Where $$\alpha = 2.33\log(T/d) \tag{3.3}$$

is the absorbance coefficient, d is the sample thickness, and $h\nu$ = 1240/(incident light (nm)) is the photon energy. The estimated bandgap of the TiO_2 is ~3.2 eV, which has been derived from the plot of $(\alpha h\nu)^{1/2}$ versus (hν). For wavelengths below 400 nm, the absorption in TNRs (TiO_2 nanorods) after etching is more than the TNRs without etching, which may be attributed to the partial dissolution of TNRs in solvothermal etching as also noticed in the SEM images. It is observed that the perovskite layer on solvothermal etched TNRs has more absorbance compare to the perovskite layer on the other two kinds of TNRs layers, as shown in Figure 3.8 (b).

The charge transport and traps in different ETL films of the solar cell structure are studied using the electrical as well as optical measurements shown in Figure 3.9. The *I-V* characteristics of three Ag/TNRs based junction diodes made of three different types of TNRs (Device 1: TNRs, Device 2: TNRs/$TiCl_4$ treated, and Device 3: TNRs/Etched/$TiCl_4$ treated) are compared in Figure 3.9 (a). The improved diode current in Device 2 and Device 3 over Device 1 is clearly observed due to a reduction in traps in the modified TNRs treated with $TiCl_4$. The space charge limited current (SCLC) region of the *IV* characteristics are shown in the inset of Figure 3.9 (a). It can be noted from the SCLC region that the carrier mobility is increased significantly with the solvothermal etching followed by $TiCl_4$ treatment. The effect of modified TNRs on the optically generated charge carriers of PSCs is also investigated in terms of the PL quenching shown in Figure 3.9 (b). The subsequent decrease in PL intensity for Device B and Device C confirms the enhancement in the photoabsorption and photocurrent in the PSCs under study. The enhanced absorption also agrees with the results shown in Figure 3.8 (b). Finally, the impedance characteristics of all the three solar cell structures measured at an applied voltage of 1 V in the frequency range of 1 kHz to 1 MHz are plotted in the inset of Figure 3.9 (b). It is found that the impedance is reduced due to $TiCl_4$ treatment of the TNRs based ETL.

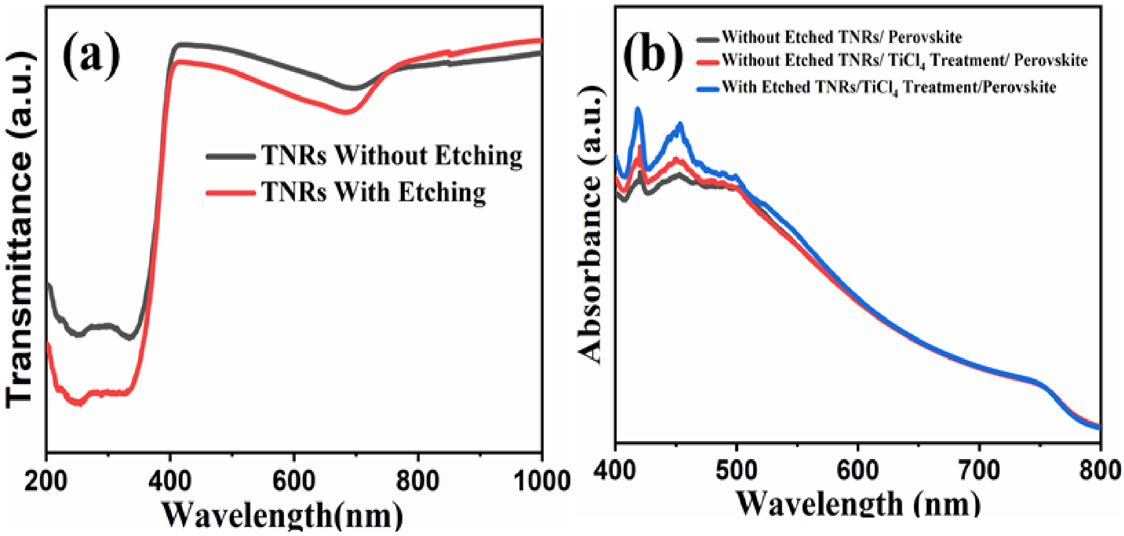

Figure 3.8: (a) Transmittance of TiO_2 NRs before and after solvothermal etching. (b) UV-VIS absorbance spectrum of perovskite film deposited on TiO_2 nanorods without $TiCl_4$ treatment, TiO_2 nanorods with $TiCl_4$ treatment before and after solvothermal etching.

3.3.2 Solar Cell Characterization

The photocurrent density (J_{ph}) vs. voltage (V) characteristic was recorded by a semiconductor parameter analyzer under the illumination of the solar spectrum through a circular mask having an area equal to the cell area of 0.0314 cm^2. The solar cell parameters such as V_{OC}, J_{SC}, FF, and PCE are obtained from the J_{ph}-V characteristic shown in Figure 3.10 (a). The solar cell parameters for different device structures are summarized in Table 3.1. The performance of the following three types of fabricated PSC is investigated in this article. The average PCE of 11.46%, V_{OC} of 0.97 V, J_{SC} of 20.75 mA/cm^{2,} and FF of 0.55 are obtained for “Device A”. The performance parameters are observed to be improved by $TiCl_4$ treatment of the ETL since the PCE of 12.90%, V_{OC} of 1.01 V, J_{SC} of 22.19 mA/cm^2, and FF of 0.57 are measured for “Device B”. The performance improvement in “Device B” over “Device A” is attributed to the enhancement of carrier lifetime and diffusion length achieved by removing the traps and voids from TNRs by the $TiCl_4$ treatment of “Device B”. Note that traps and voids in TNRs enhance the recombination of charge carriers and limit the diffusion length of carriers. “Device C” fabricated by using TNRs ETL with solvothermal etching followed by $TiCl_4$ treatment has an average PCE of 14.78%, FF of 62%, V_{OC} of 1.05 V, and J_{SC} of 22.31 mA/cm^{2,} which are the best among all the three types of PSCs (i.e., A, B, and C) considered in this study.

It is important to mention that the cell parameters discussed above are directly affected by the values of the shunt resistance (R_{Sh}), series resistance (R_S), and other losses in the devices [144]. The decrease in series resistance and increase in shunt resistance enhance the value of FF, which, in turn, results in higher PCE and optimizes the output power close to the theoretical maximum value [144]. The results confirm that the solvothermal etching process along with $TiCl_4$ treatment can be explored for improving the performance of the TNRs ETL based hybrid PSCs by reducing the surface traps and defects in TNRs by the $TiCl_4$ treatment and enhancing the effective light absorption area by the solvothermal etching process. The highest PCE of 15.16% is achieved for the champion Device-C along with FF of 0.64, J_{SC} of 22.64 mA/cm^{2,} and V_{OC} of 1.04, which are possibly the best under open-air measurements. The power conversion efficiency of $MAPbI_3$ and different type of TiO_2 ETL based PSCs are compared in

Table 3.2. Clearly, the use of modified TNRs based ETL in our proposed device shows promising power conversion efficiency under high humid and open atmosphere. The efficiency is believed to be enhanced further if the fabrication and measurements are performed in a controlled environment which is not available in our laboratory. We will consider the external quantum efficiency (EQE) of the devices A, B, and C compared in Figure 3.10 (b). The EQE is computed by using the following relation [145]:

$$EQE = 1240 \times \left(\frac{R}{\lambda}\right) \times 100\% \tag{3.4}$$

Where 'R' is the photoresponsivity and λ in the wavelength of the incident light. Figure 3.10 (b) shows the highest value of EQE in Device C, which again confirms its superior performance over the other two devices.

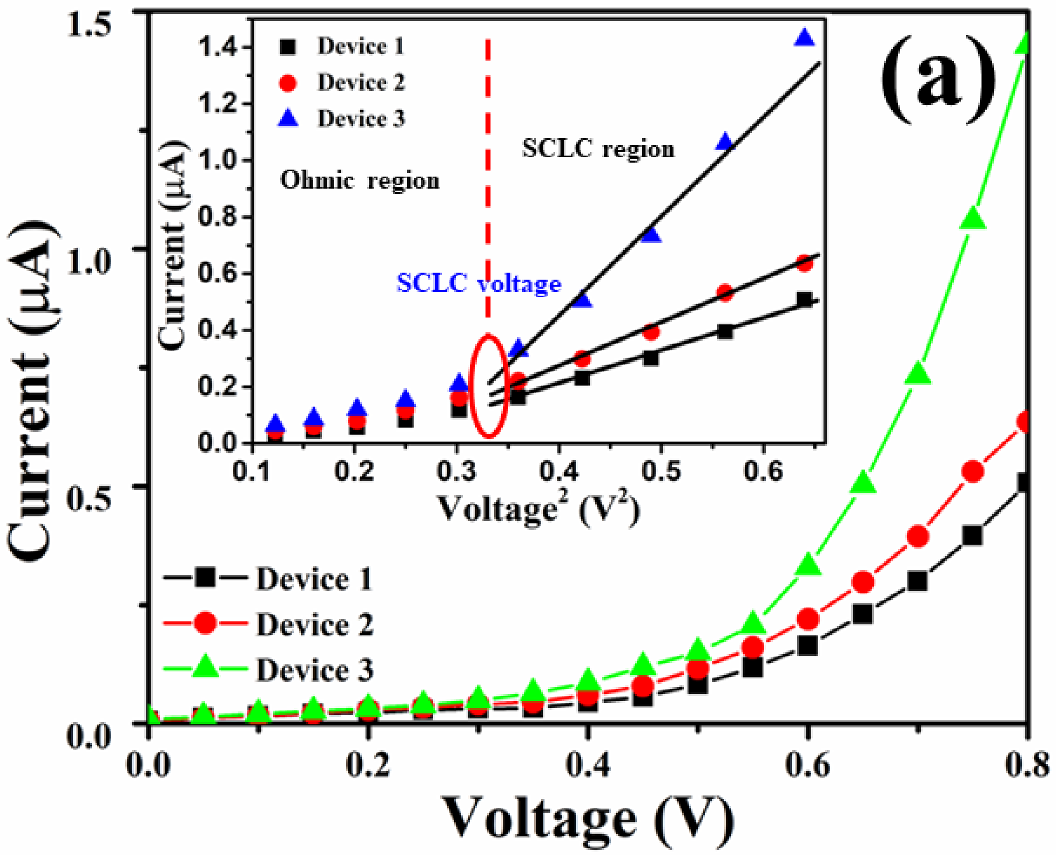

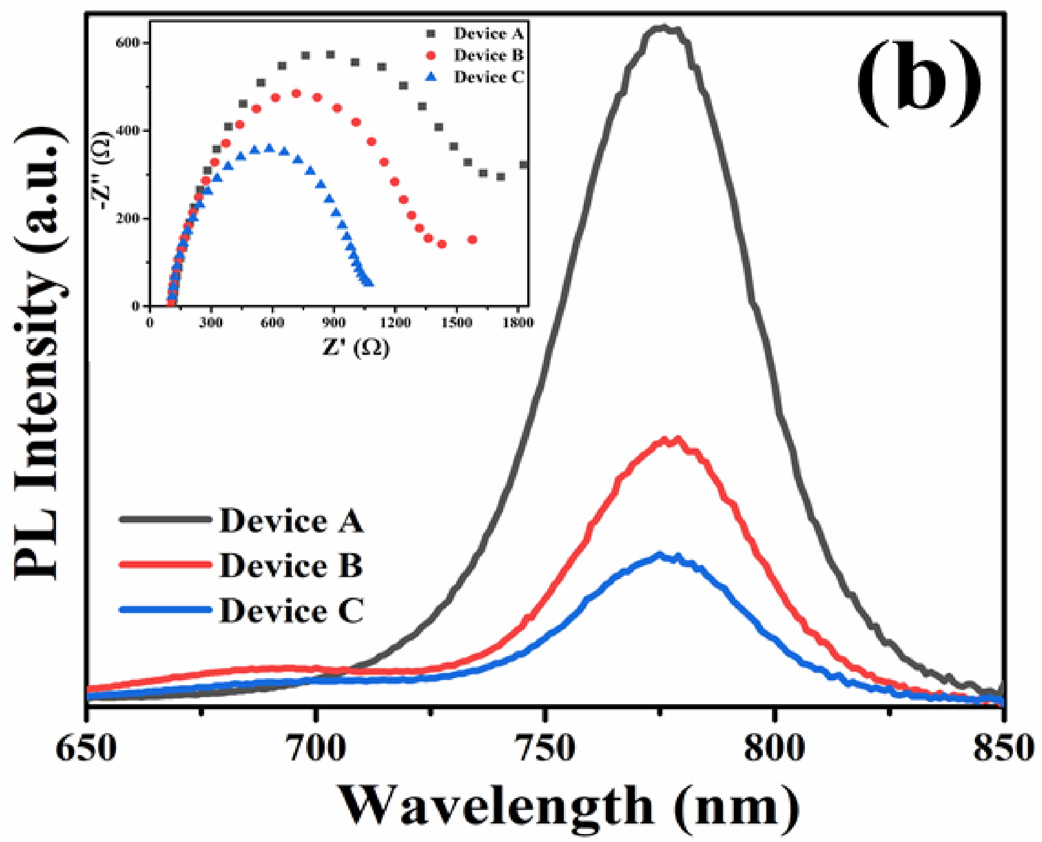

Figure 3.9: (a) *I-V* characteristics of the junction diode made of modified TNRs. Inset of (a) shows SCLC region in all the diode. (b) Emission characteristics in three solar cell structures. of TiO_2 NRs before and after solvothermal etching. Inset of (b) shows impedance characteristics of three solar cells.

Table 3.1: Device Comparison based on TiO_2 NRs ETL

Device Parameter → ↓ ETL		J_{SC} (mA/cm^2)	V_{OC} (V)	FF	PCE (%)
TNRs (Device A)	Average	20.75 ± 02.25	0.97 ± 0.04	0.55 ± 0.05	11.46 ± 0.65
	Champion	20.18	0.964	0.61	12.03
TNRs/$TiCl_4$ treated (Device B)	Average	22.19 ± 01.5	1.01 ± 0.04	0.57±0.04	12.90 ± 1.36
	Champion	22.18	1.07	0.61	14.55
TNRs/Etched/$TiCl_4$ treated (Device C)	Average	22.31 ± 0.30	1.05 ± 0.04	0.62 ±0.02	14.78 ± 0.45
	Champion	22.64	1.04	0.64	15.16

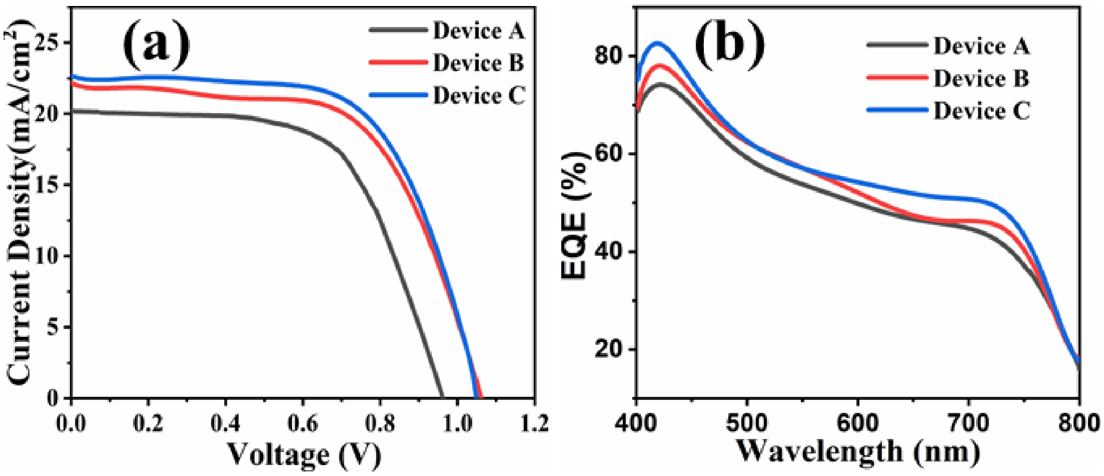

Figure 3.10: (a) J_{ph}-V characteristics of device A, B & C; (b) Comparison of EQE of device A, B & C.

TABLE 3.2: POWER CONVERSION EFFICIENCY OF TiO_2 ETL BASED PSCS.

ETL	PCE (%)	Ref.
TiO_2 nanorods	9.4	[146]
TiO_2 nanowire	11.7	[75]
Bare TiO_2 NR $TiCl_4$-treated TiO_2 NR 4.8 nm TiO_2 nanoparticle on TNRs $TiCl_4$-treated mesoporous- TiO_2	5.03 7.98 13.45 9.58	[147]
TiO_2 NP film (0.4 vol %) rGO/mesoporous- TiO_2	11.5 13.5	[148]
TiO_2 nanoparticles TiO_2 nanotubes TiO_2 nanotube/TiO_2 nanoparticle	6.56 7.63 9.16	[149]
TiO_2 mesoporous	12.62	[150]
Rutile TiO_2 nanorod	16.11	[151]
Compact- TiO_2 Compact- TiO_2 / mesoporous- TiO_2	11.85 14.76	[152]
TiO_2 (Compact + mesoporous) 0.5 mol% Al TiO_2	11.49 14.05	[153]
TNRs/ TNRs Etching/$TiCl_4$ treatment	15.16	This Work

3.4 Conclusion

The performance improvement in hybrid PSCs by solvothermal etching and $TiCl_4$ treatment of TNRs based ETL grown on the FTO coated glass substrates have been analyzed in this chapter. The performance parameters of three types of PSCs using hydrothermally synthesized TNRs based ETLs without etching and $TiCl_4$ treatment (Device A); with only $TiCl_4$ treatment but no etching of TNRs (Device B); and TNRs with solvothermal etching followed by $TiCl_4$ treatment (Device C) are compared. The PCE, V_{OC}, J_{SC} and FF are measured as 11.46%, 0.97 V, 20.75 mA/cm^2 and 0.55 for "Device A"; 12.90%, 1.01 V, 22.19 mA/cm^2, and 0.57 for "Device B"; and, 14.78 %, 1.05 V, 22.31 mA/cm^2 and 0.62 for and "Device C". The EQE is also found to be the best for "Device C" among the three devices. The improvement in the performance parameters of "Device C" is attributed to the enhancement of recombination lifetime of carriers due to the reduction of traps and voids in the TNRs by $TiCl_4$ treatment as well as to the enhancement of the effective surface area of the TNRs by solvothermal etching.

CHAPTER 4

Fabrication and Characterization of FTO/ZnO Seed Layer/ ZnO Nanorods/$CH_3NH_3PbI_3$/PTAA/Au Solar Cells with Different Seed Layers*

Contents

CHAPTER 4

Fabrication and Characterization of FTO/ZnO Seed Layer/ ZnO Nanorods/$CH_3NH_3PbI_3$/PTAA/Au Solar Cells with Different Seed Layers

4.1 Introduction

The effects of thickness and surface morphology of hydrothermally grown TNRs based ETL on the performance of FTO/TNRs/$CH_3NH_3PbI_3$/PTAA (or Spiro-OMeTAD)/Pd perovskite solar cells (PSCs) have been investigated in Chapter-2 and Chapter-3 respectively. It is discussed in Chapter-1 that, like the TiO_2 nanorods (TNRs), ZnO nanorods (ZNRs) can also be used for the ETL in the solar cells [154]. In view of the above, we will now explore the hydrothermally grown ZnO nanorods (ZNRs) for the ETL in the PSCs in this chapter. The ZnO seed layer on the FTO substrate deposited by various methods can be used for the growth of ZNRs by the hydrothermal method. Various methods such as spray pyrolysis, electrochemical deposition, CVD, spin coating, sol-gel, dipping method, etc., are used for the seed layer deposition on the FTO substrates [155]-[158]. The deposition method of the seed layer plays a crucial role in determining the properties of the ZNRs grown by hydrothermal methods [90]. In this chapter, four different types of ZnO seed layers of drop-casted ZnO film, spin-coated colloidal ZnO nanoparticles (NPs) film, spin-coated colloidal ZnO quantum dots (QDs) film, and hydrothermally grown ZnO NRs film were deposited on four FTO substrates. The seed layer coated FTO substrates were then processed for growing ZnO NRs (ZNRs) based ETL by the hydrothermal method. Then spin-coated $CH_3NH_3PbI_3$ hybrid perovskite active layer and PTAA based HTL layers and thermally evaporated Au film for contact electrode were successively deposited for fabricating four different PSC devices. The effects of coverage density, surface morphology, and orientation of the four different types ZNRs based ETLs on the performance parameters of FTO/TNRs/$CH_3NH_3PbI_3$/PTAA/Au structure-based PSCs have been investigated in this chapter. The content of the present chapter is outlined as follows:

Section 4.2 describes the details of the deposition process of ZnO seed layers, ZNRs, and the fabrication of PSCs. The measurement results for different seed layers and subsequent discussion are presented in Section 4.3. Finally, Section 4.4 summarizes the major finding and observations of this chapter.

4.2 Experimental Details

In this section, deposition of different seed layers, hydrothermal growth of ZNRs, and fabrication steps for different types of ZNRs based PSCs are presented.

4.2.1 Solution Preparation for Seed Layer

The FTO coated substrates (15×15 mm^2) were first cleaned using soap solution and rinsed in deionized (DI) water. Subsequently, the substrates were cleaned with acetone, 2-propanol, and then dried at 90°C for 10 minutes. Four different types of seed layer samples were prepared for the growth of ZNRs using ZnO drop-cast, ZnO nanoparticles (NPs), ZnO quantum dots (QDs), and solvothermal (ZnO NRs itself). The solution for the first sample (ZnO drop-cast) was made using 25 mM of zinc acetate dihydrate and 50 mM of sodium hydroxide (NaOH) in ethanol [159]. The sodium hydroxide solution was added dropwise to the zinc acetate dihydrate solution under vigorous stirring at 65^0C for 2 hours. The prepared solution was washed with ethanol several times after completing the reaction. The “ZnO NPs” sample was synthesized using 0.1 M solution of zinc nitrate ($Zn(NO_3)_2.6H_2O$) and 0.2 M solution of potassium hydroxide (KOH) in DI water [160]. The KOH solution was added slowly into the zinc nitrate solution and kept under vigorous stirring continuously for 1 hrs. The prepared solution has an appearance of milky white in color. Finally, the solution was centrifuged at 5000 rpm for 5 min and was then washed with ethanol. Further, the prepared NPs are dried, and 10 mg of NPs are dissolved in 1 ml of chloroform.

“ZnO QDs” was prepared by mixing zinc acetate dihydrate (100 mM) in 2-methoxy ethanol (coordinating ligand) and constantly stirred on a hot plate at a temperature of 60°C in a nitrogen environment. An equimolar concentration of monoethanolamine (MEA) was added drop-by-drop in the solution at a constant temperature of 60^0C with continuously stirring [161].

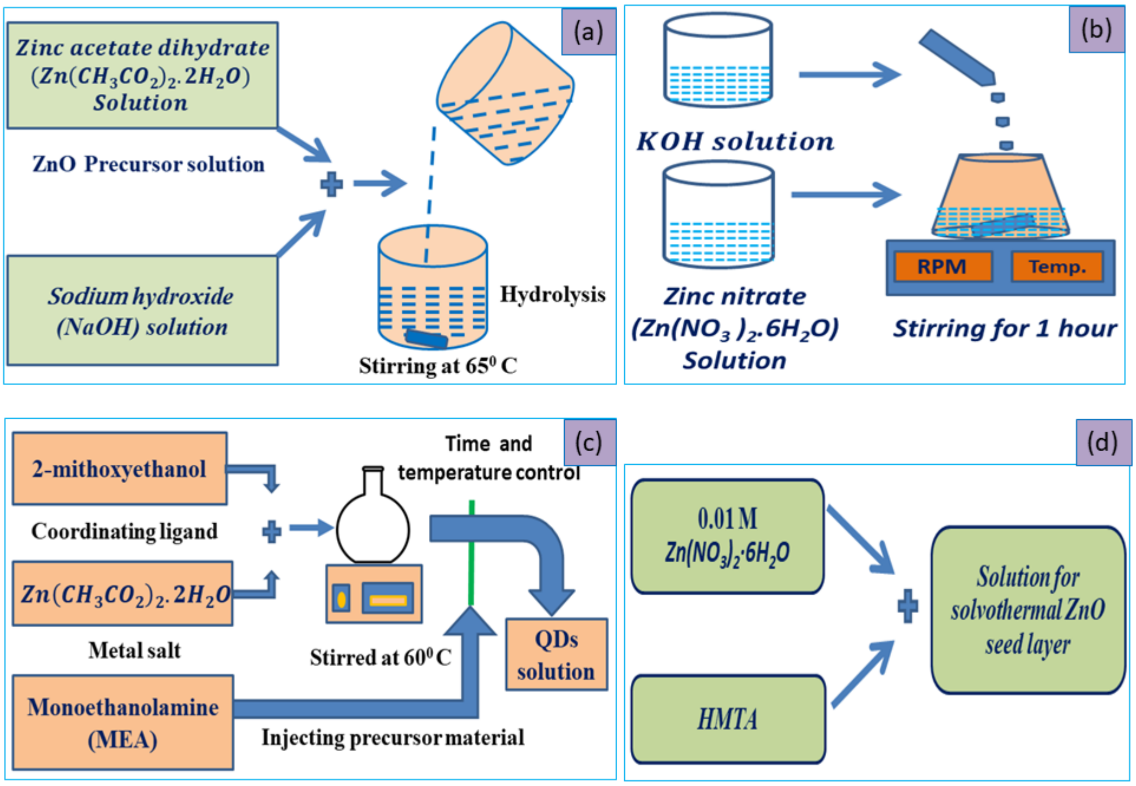

Figure 4.1: Graphical view of the preparation process of the solutions for the seed layers (a) ZnO drop-cast (b) ZnO NPs (c) ZnO QDs (d) Solvothermal ZnO NRs.

By controlling the reaction time, a uniform particle size of ZnO QD is obtained in the order of Bohr's radius (~2.34 nm for ZnO). After that solution was filtered out by using a PVDF filter (0.22 μm) to remove unreactive particles. The last sample, "ZnO solvothermal," was prepared by using a mixture of 0.01 M concentration of zinc nitrate hexahydrate ($Zn(NO_3)_2 \cdot 6H_2O$) and HMTA in DI water. The ZnO seed layer solution preparation is graphically demonstrated in Figure 4.1.

4.2.2 Growth of ZnO Nanorods

There are several methods reported for the fabrication of the ZNRs. In the present work, the hydrothermal synthesis route was used for the fabrication of nanorods. A seed layer of different precursor solutions was deposited with the help of drop-cast, spin coating, and solvothermal methods. 40 µl precursor solution of the first sample was deposited using drop-cast technique onto cleaned FTO substrate, and the substrate was dried on a hot plate. This method (step) was repeated several times and annealed at 350^0C for 1 hour in ambient condition. The seed layer in sample 2 (NP) and 3 (QDs) were deposited via spin coating (SPM-150LC, GmbH) technique at 3000 rpm for 30 sec and heated on the hot plate at 100°C for 10 minutes. This process was repeated 3 times for the conformal deposition of the seed layer. The seed layer in sample 4 was deposited by hydrothermal process. FTO coated substrate (FTO side kept facedown) was immersed vertically in prepared solution in Teflon lined stainless steel autoclave for 1 hour at 90^0C for growth of ZnO seed layer. After the set time, the autoclave was kept outside the furnace and cooled slowly till room temperature. The sample was taken out from the autoclave and washed with running DI water several times, and dried with N_2 gas flow. The sample was rinsed in DI water and annealed at 150^0C for 1 hour to form a ZnO compact layer, which acts as a seed layer. Finally, all the seed layer coated substrate was annealed at 350°C. The deposition process of different seed layers is illustrated in Figure 4.2.

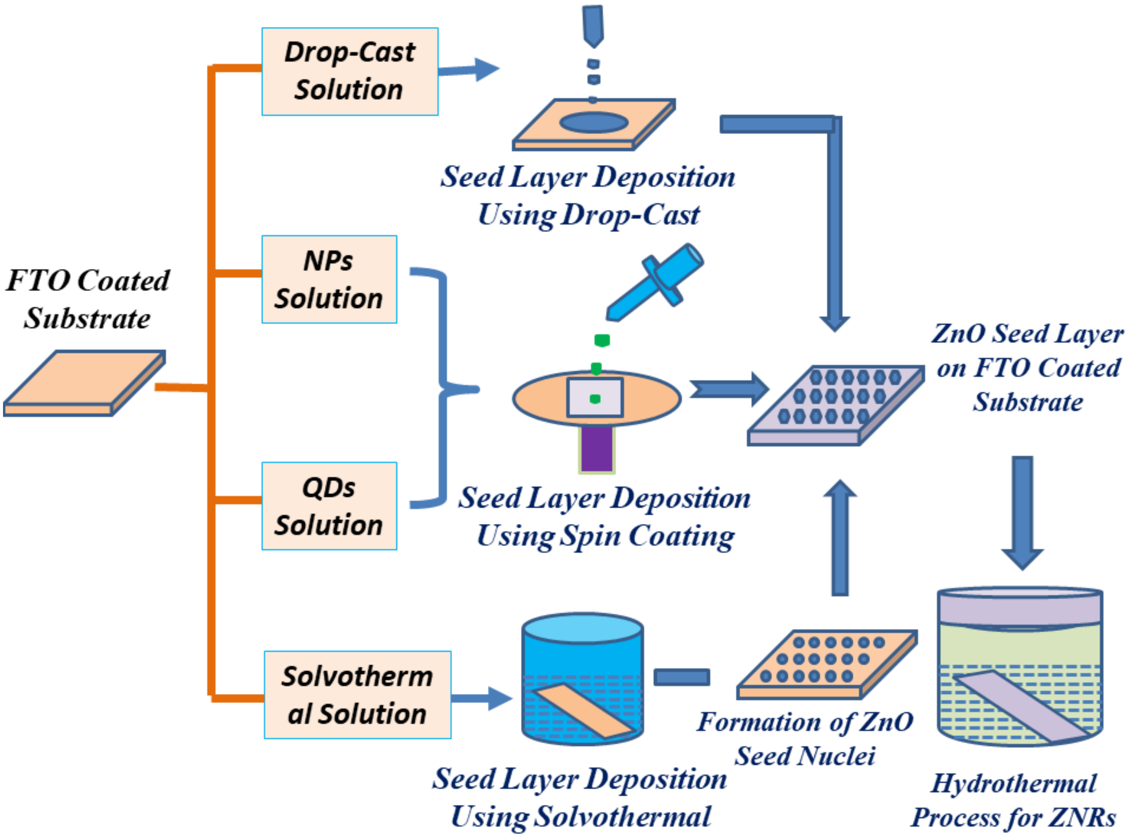

Figure 4.2: Seed layer deposition process using drop-cast, spin coating, and solvothermal. Growth of nanorods in the last step using the solvothermal process.

The seed layer coated FTO substrates were placed in the autoclave for the hydrothermal process as discussed for the seed layer of sample 4 and shown in Figure 4.2. The ZnO nanorod (ZNRs) on every sample was grown using an equimolar 50 mM solution of zinc nitrate hexahydrate ($Zn(NO_3)_2{\cdot}6H_2O$) and hexamethylenetetramine (hexamine) in DI water at 65^0C for 2 hours. Zinc nitrate and hexamethylenetetramine were used as the source of Zn^+ and OH^-, respectively in the hydrothermal process. No precipitate occurred when hexamine was mix in solution. By increasing in temperature, hexamine was converted into $Zn(OH)_2$ by decomposition. Further, the ZnO nuclei were created on the sample and continuously increased with time. The nuclei grew up, and the thin film of ZnO formed on the sample. The possible reaction mechanism for ZNRs growth is given as [162]:

$$(CH_2)_6N_4 + 6H_2O == 6HCHO + NH_3 \tag{4.1}$$

$$NH_3 + H_2\,O == NH_4^+ + OH^- \tag{4.2}$$

$$2OH + Zn^{2+} == Zn(OH)_2 \tag{4.3}$$

$$Zn(OH)_2 == ZnO_{(s)} + H_2O \tag{4.4}$$

4.2.3 Solar Cell Fabrication

A hybrid perovskite layer was coated on the ZNRs via a two-stage spin coating method. The separate precursor solution of methylammonium iodide (CH_3NH_3I (~ 10 mg)) and lead iodide (PbI_2 (~ 462 mg)) was prepared in 1 ml of 2-propanol and N, N-dimethyl formamide (DMF) solvent. A solution of PbI_2 was heated at 90°C and continuously stirred at 300 rpm for 1 hour on the hot plate. 50 µl of this solution was then spin-coated at 3000 rpm for 30 seconds and heated at 70°C for 10 minutes on the hot plate. After that, the CH_3NH_3I solution was spin-coated at 3000 rpm as the second precursor. Toluene was used as an anti-solvent on top of perovskite thin-film during spin coating, which improves the surface morphology as well as conductivity by removing the voids and residues from methylammonium and halide ions [41]. The film was then heated at 100°C for 30 minutes to improve the crystallinity of the film. A thin layer (~100 nm) of PTAA was spin-coated at 2000 rpm for 30 s for the proper charge separation from the active layer (i.e., perovskite layer).

Finally, a thin layer (~80 nm) of gold (Au) was deposited on PTAA, which acts as a top electrode by using a thermal evaporation unit (FL400, HHV). The detailed fabrication step is depicted in Figure 4.3. A comparative study was done to investigate the effect of different types of the seed layer on the PSCs' parameter. The four different types of PSCs have been fabricated with a different seed layer and named as follows:

PSC A:-Au/PTAA/$CH_3NH_3PbI_3$/ZNRs/ZnO Drop-cast seed layer/FTO

PSC B:-Au/PTAA/$CH_3NH_3PbI_3$/ZNRs/ZnO NPs seed layer/FTO

PSC C:-Au/PTAA/$CH_3NH_3PbI_3$/ZNRs/ZnO QDs seed layer/FTO

PSC D:-Au/PTAA/$CH_3NH_3PbI_3$/ZNRs/ZnO NR seed layer/FTO

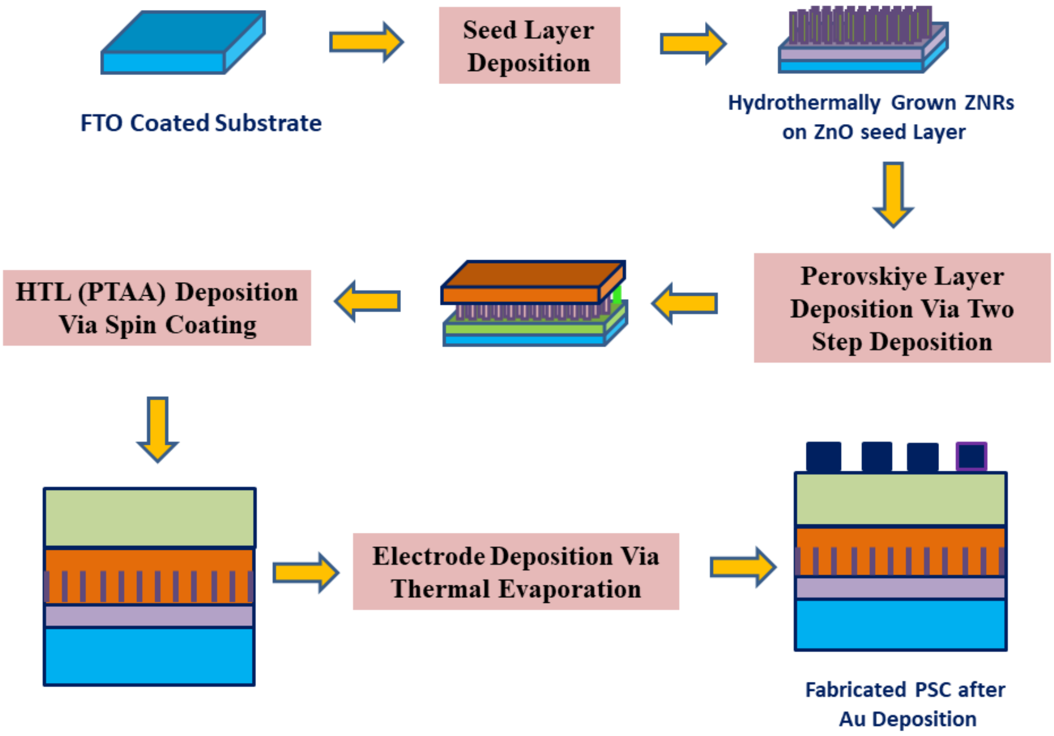

Figure 4.3: Fabrication flow diagram for the perovskite solar cell.

4.3 Results and Discussion

This section presents the optical and electrical characterizations of PSCs fabricated with different ZnO seed layers.

4.3.1 Thin Film Surface Characteristics

The scanning images of the top view of ZNRs grown on on different seed layer of ZnO deposited using drop-cast, spin coating, and solvothermal is shown in Figure 4.4. A significant morphological difference is observed. The nanorods which are grown on the first sample (ZnO seed layer by drop cast) are not well aligned and randomly distributed on the substrate. The growth is not perpendicular to the c-axis, even though growth is observed in all directions. It happened since the seed layer is not uniformly distributed throughout the substrate. The growth of ZNRs is uniform, well-distributed, and aligned for the ZnO QDs based seed layer. The nanorods' growth is in all directions and also perpendicular to the c-axis. It is possible because of the uniform growth of the seed layer. The size distribution and alignment of ZNRs are highly influenced by the particle size and the surface roughness of the seed layer. The particle of the seed layer acts as a nucleation center for the growth of ZNRs. The ZnO seed layer deposited from NPs solution has a larger particle size compared to ZnO QDs coated sample. It is shown in Figure 4.4 (b) and (c) that the diameter of ZNRs is more in the ZnO NPs based seed layer. It is observed from the SEM image that the surface to volume ratio is more in NPs and QDs seed layer based ZNRs compared to the other two samples, and it's also confirmed from the TEM image shown in the inset of Figure 4.4 (b) and (c). The ZNRs deposited on solvothermally grown seed layer have random distribution and non-uniformity due to poor nucleation of ZNRs. So it can be analyzed that solvothermally grown seed layer has a large particle size compared to the particle size of the other three samples. ZNRs deposited on the ZnO QDs seed layer are well decorated, better vertically aligned, and high packing density throughout the surface. The height and thickness are also consistent in ZnO QDs seed layer based ZNRs. It is possible due to good crystalline and uniform particle size (which is also supported by TEM image in the inset of Figure 4.4 (c)) of ZnO QDs seed layer.

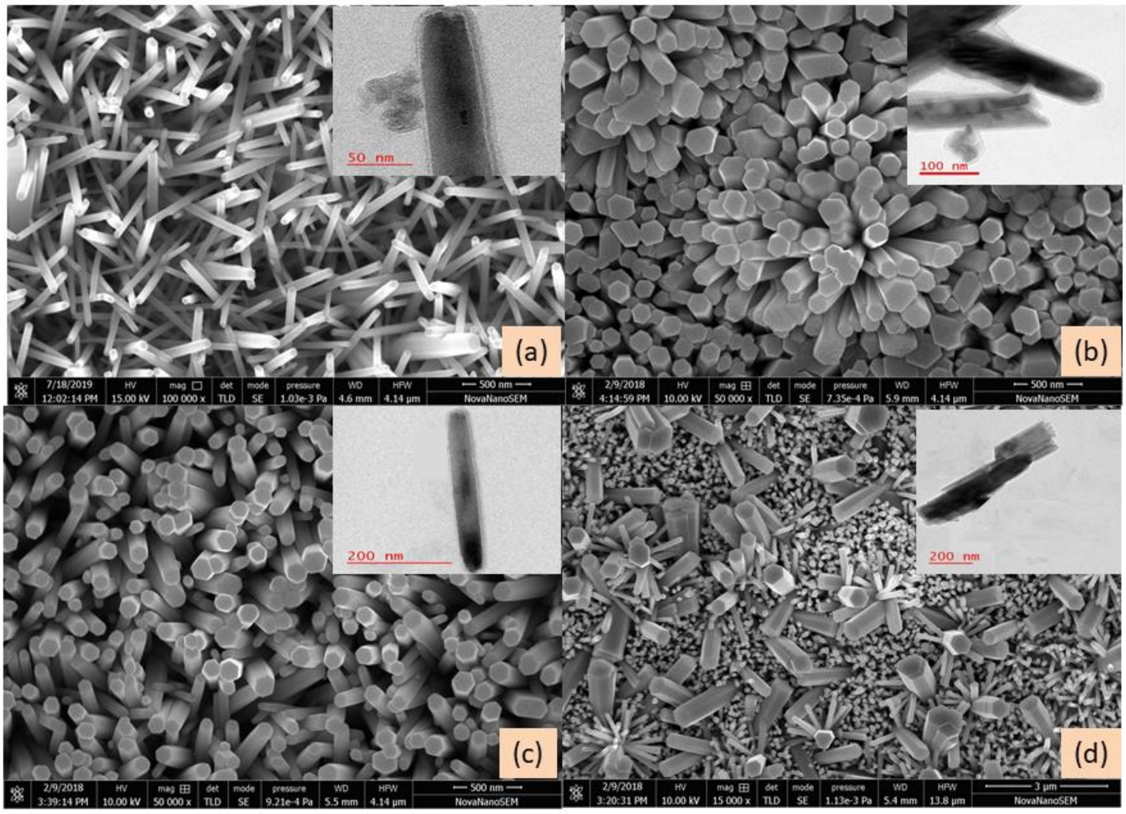

Figure 4.4: Top view of ZnO nanorods grown on different seed layers of (a) drop-cast (b) spin coated (ZnO NPs) (c) spin coated (ZnO QD) (d) solvothermal.

Figure 4.5 shows the X-ray diffraction (XRD) pattern of ZNRs grown on four different seed layer samples (Drop-cast, NPs, QDs, and solvothermal). The XRD image shows that most of the dominant diffraction peaks are corresponds to the wurtzite phase of ZnO and reveals uniform crystallinity. The major high-intensity peaks, such as 002, 101, 103, and 111, are common in all four samples (JCPDS 65-3431). The indexed peaks at $2\Theta \approx 31.77^\circ$, 34.42°, 36.25°, 47.53°, 56.60°, 62.85°, 66.38°, 67.95° and 72.56° correspond to the reflections from (100), (002), (101), (102), (110), (103), (200), (112) and (004) crystal planes of the wurtzite phase ZnO, whereas others peaks belong to the crystal plane of FTO. The intense and strongest peak was observed for the (002) plane. It is analyzed from the XRD pattern that the extra peak in the QDs based ZNRs sample is coming at 2θ=56.60° and 72.56° due to the good orientation of ZNRs along the c-axis. So, it can be concluded from the XRD pattern that the QDs based ZNRs have a uniform and better crystallinity compared to other samples.

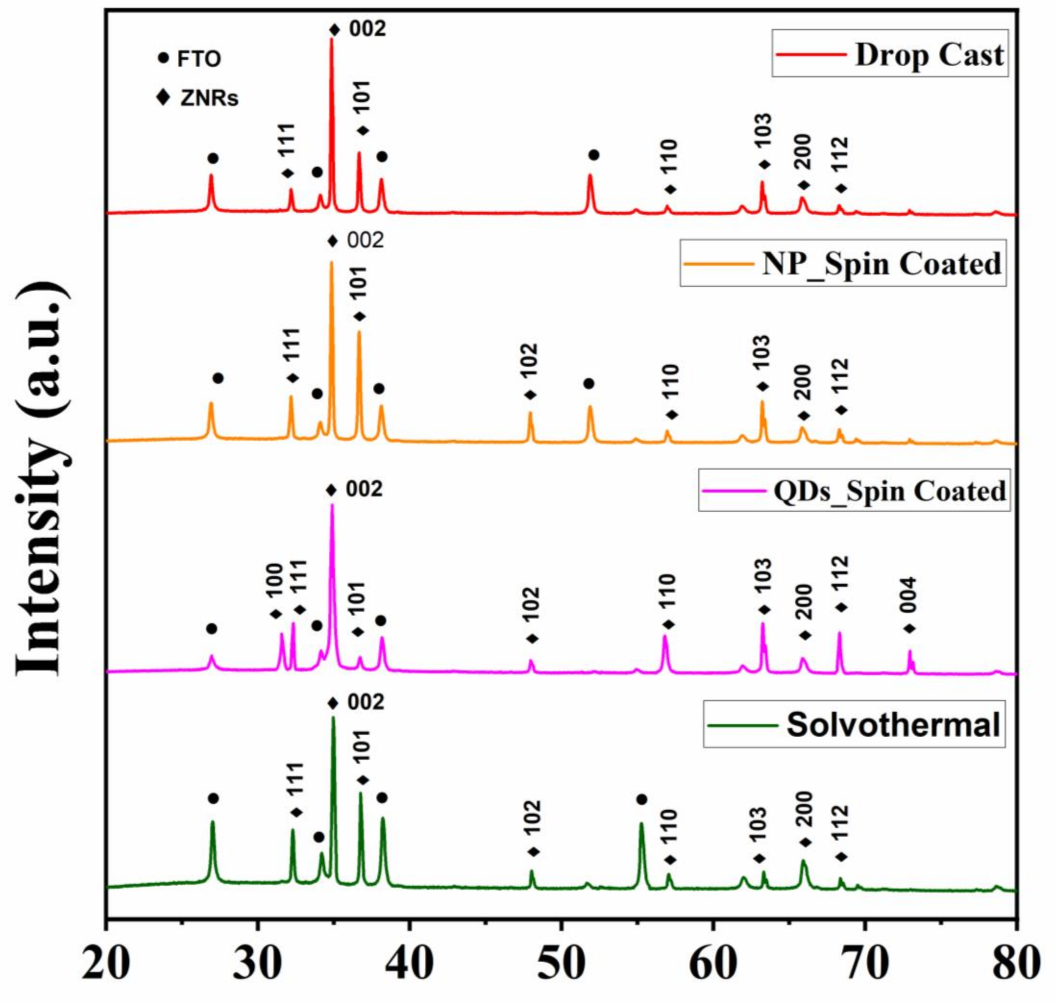

Figure 4.5: XRD pattern of ZnO NR grows on different ZnO seed layers deposited using (a) drop-cast (b) spin coated (ZnO NPs) (c) spin coated (ZnO QD) (d) solvothermal.

4.3.2 Optical Characterization

The optical absorbance and photoluminescence (PL) in the four types of seed layers on FTO coated substrate are plotted in Figure 4.6. A sharp change in absorbance has been observed at 395 nm wavelength in three seed layers (Drop-cast, NPs, and solvothermal based samples), while the QDs based seed layer sample has absorbance change at a wavelength of 375 nm. The optical characteristics are also verified by photoluminance (PL) emission spectra, where the intensity curve of PL is matched with the band edge of absorbance spectra. The QDs deposited seed layer sample has lower band edge spectra, which is due to the smaller particle size with respect to the other three samples. It can be observed from Figure 4.6 that nanoparticle and drop-cast seed layer based samples have similar absorbance pattern, which is also confirmed from the PL emission graph. The optical band gap is also calculated by using the Tauc plot corresponding to the respective graph depicted in Figure 4.7.

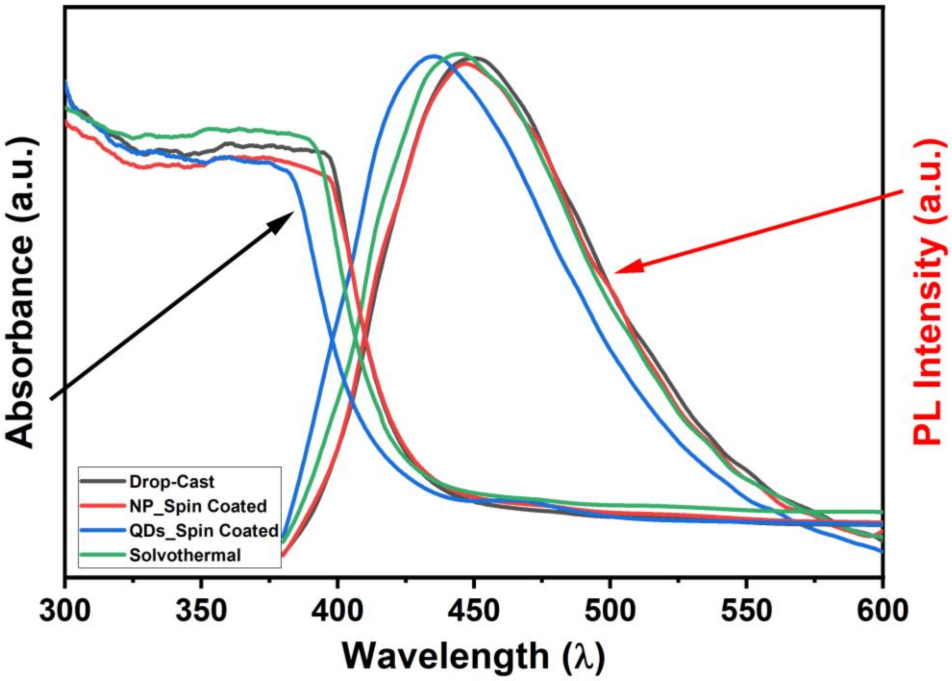

Figure 4.6: Photoluminescence emission and optical absorbance spectra of ZnO seed layer samples deposited on FTO substrate.

An abrupt change in absorbance spectra near the optical bandgap edge of ZNRs is calculated by the Tauc relationship [163]. The Tauc relationship is given as:

$$\alpha h\upsilon = A(h\upsilon - E_g)^m$$

Where $\alpha = 2.33 \log (T /d)$ is the absorbance coefficient, d is the film thickness, and $h\nu = 1240/[\text{incident light (nm)}]$ is the photon energy. The absorption in ZNRs can be written as A = log (1/T). The estimated bandgap is 2.95 eV for drop-cast, 3 eV for NP, 3.05 eV for solvothermal, and ~3.1 eV for QDs based seed layer sample, which have been derived from the plot of $(\alpha h\nu)^{1/2}$ versus (hν). The derived optical band gap value can be correlated to the particle size of seed layer samples. The larger optical band gap of ZnO QDs seed layer based ZNRs sample calculated from the Tauc plot confirms the smaller particle size compared to other samples.

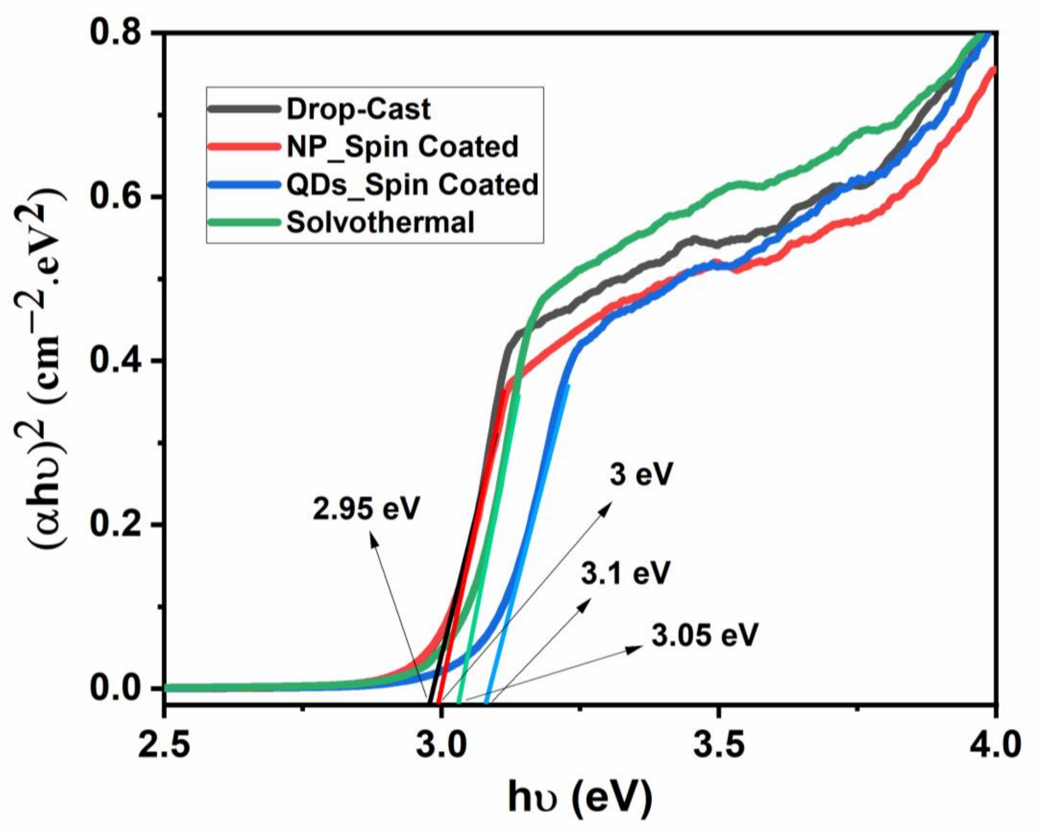

Figure 4.7: Tau plots for different ZnO seed layer samples.

The transmittance spectra of ZNRs grown on different ZnO seed layer is recorded by UV-Vis spectrometer for the wavelength range from 250 nm to 800 nm, as shown in Figure 4.8. The ZNRs grown on the ZnO QDs seed layer exhibits enhanced transmittance spectra in the visible range (from 400 nm to 700 nm) because of vertically oriented ZNRs compared to the other three samples. The ZNRs grown on nanoparticle and drop-cast based seed layer substrate have almost similar transmittance spectra but less than the transmittance spectra of ZnO QDs seed layer based ZNRs. The reduction in transmittance spectra in ZnO nanoparticle and drop-cast based sample is because of photon scattering phenomena, while the ZNRs deposited on solvothermally grown seed layer based sample have reduced transmittance due to random growth of ZNRs and an increase in surface roughness of the samples. Note that the optical band gap for ZNRs can also be derived from the transmittance spectrum. The ZNRs have strong band edge transmittance near ~370 nm due to crystalline ZNRs, which reveal more transmittance towards the visible range. In addition, ZNRs deposited on ZnO QDs seed layer having more transmittance among all samples due to single crystallinity, uniform distribution, and vertically well-aligned on the substrate or in other words, solvothermal seed layer based sample has less transmittance due to more scattering within ZNRs. The less transmittance in solvothermal-based ZNRs sample results in less optical absorbance for PSC D, consequently poor device performance.

4.3.3 Electrical Characterization

The four perovskite solar cells' impedance measurement is recorded at an applied voltage of 1 V in the frequency range of 1 kHz–1 MHz, as shown in Figure 4.9. It is estimated from Figure 4.9 that the impedance is lowest for PSC C because of fewer defects in the electron transport layer. The current density-voltage (J-V) characteristics of the solar cells in the PTAA/$CH_3NH_3PbI_3$/ZNRs structure on the different types of seed layer are shown in Figure 4.10. The J-V characteristics reveal that power conversion efficiency is maximum for PSC C, which has a seed layer of quantum dots. It is also observed that there is no significant change in PCE of drop-cast and NP seed layer based PSCs. The FF of PSC C is highest while it is lowest in the case of PSC D. The possible reason for that is ZNRs of PSC C are well aligned and perpendicular to the substrate, so that collection of charges takes place effectively. The FF is decreased due to the fact that the NR is not well aligned and not perpendicular to the c-axis in PSC A and D. The V_{OC} is minimum in case of solvothermal deposited PSC due to more internal series resistance and more chance of short-circuiting of the device. Whereas V_{OC} is maximum in the case of QDs seed layer based PSC due to lower series resistance. The increment in the V_{OC} is observed due to better alignment of ZNRs (As shown in SEM image) or less chance of short-circuiting and long electron pathway in the QDs seed layer based PSC. The photovoltaic parameters of four types of cells based on different seed layers are compared in Table 4.1.

Table 4.1: Photovoltaic parameter of different PSCs based on different seed layers**.**

ZnO Seed Layer	**V_{OC}**	**J_{SC}**	**FF**	**Efficiency (%)**
PSC A	0.95	19.26	0.58	9.12
PSC B	0.98	17.77	0.55	9.68
PSC C	1.01	19.14	0.64	10.69
PSC D	0.91	13.98	0.48	6.09

The overall optical absorbance is higher in both devices (PSC A and C) due to the large surface to volume ratio, which results in more current density. The voids and defects in the solvothermally deposited seed layer-based device enhance the possibility of recombination of electron-holes, resulting in a decrease in PSCs' performance. The distribution of ZNRs is non-uniform, so more voids and defect states in ZNRs, which results in a decrement in the V_{OC} as well as current-density in PSC D.

External quantum efficiency (EQE) of the solar cell is determined by using the following relation [164]:

$$EQE = 1240 \times \left(\frac{R}{\lambda}\right) \times 100\% \tag{4.5}$$

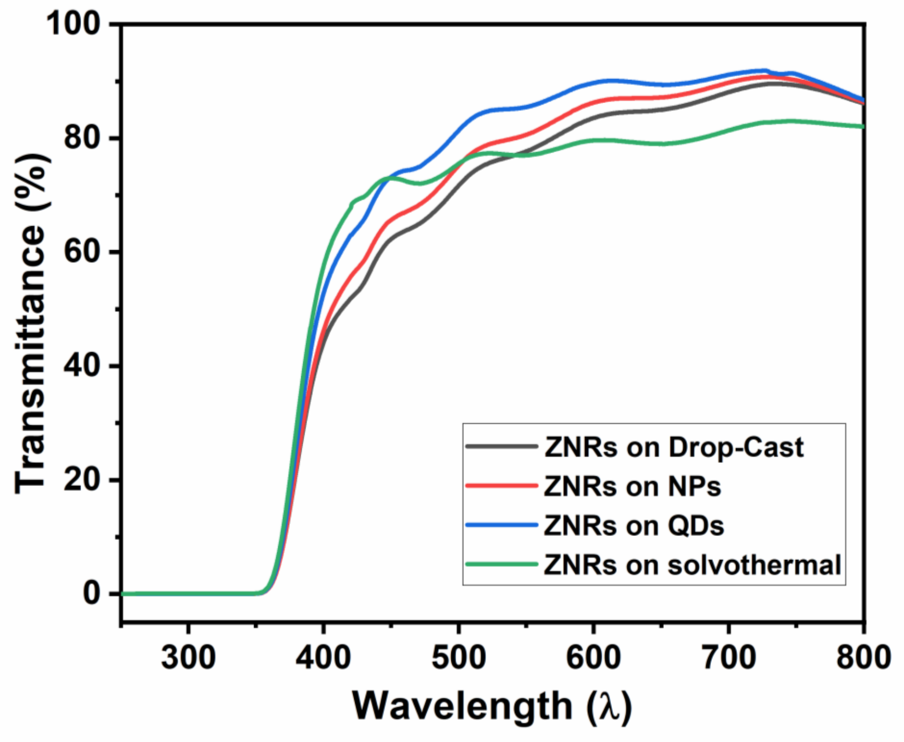

Figure 4.8: Transmittance spectra of ZnO nanorods deposited on various ZnO seed layer

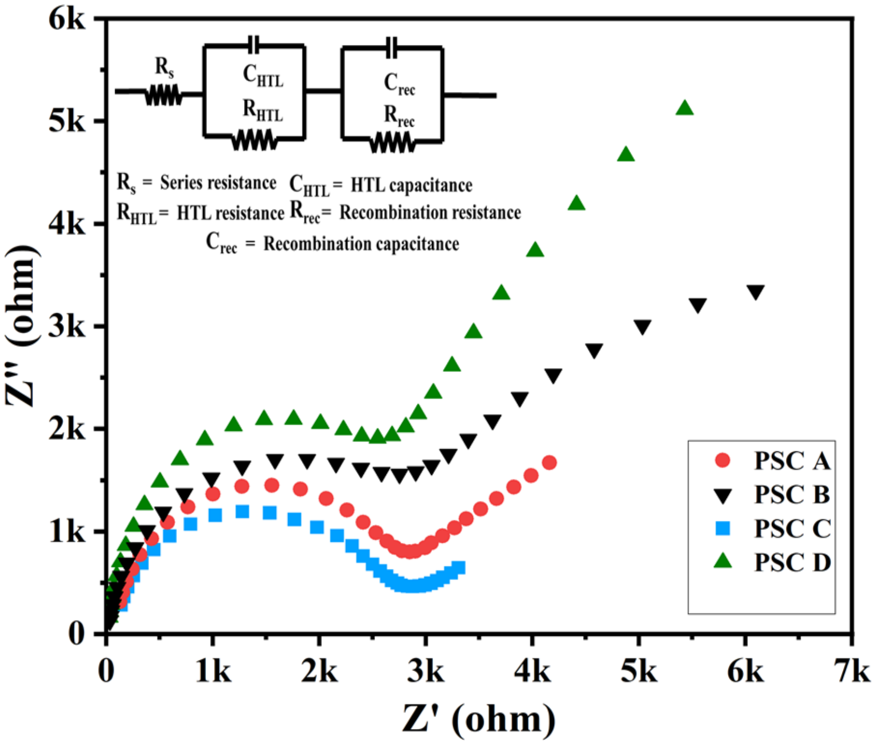

Figure 4.9: Impedance characteristics of PSCs A, B, C, & D

where “R” is the photoresponsivity and λ is the wavelength of the incident light. EQE for all the PSCs has been plotted in Figure 4.11 to compare the optical energy to electrical energy conversion in the selected wavelength range. The measured EQE is almost identical (~75%) for PSC A and PSC B in the range of 300-900 nm.

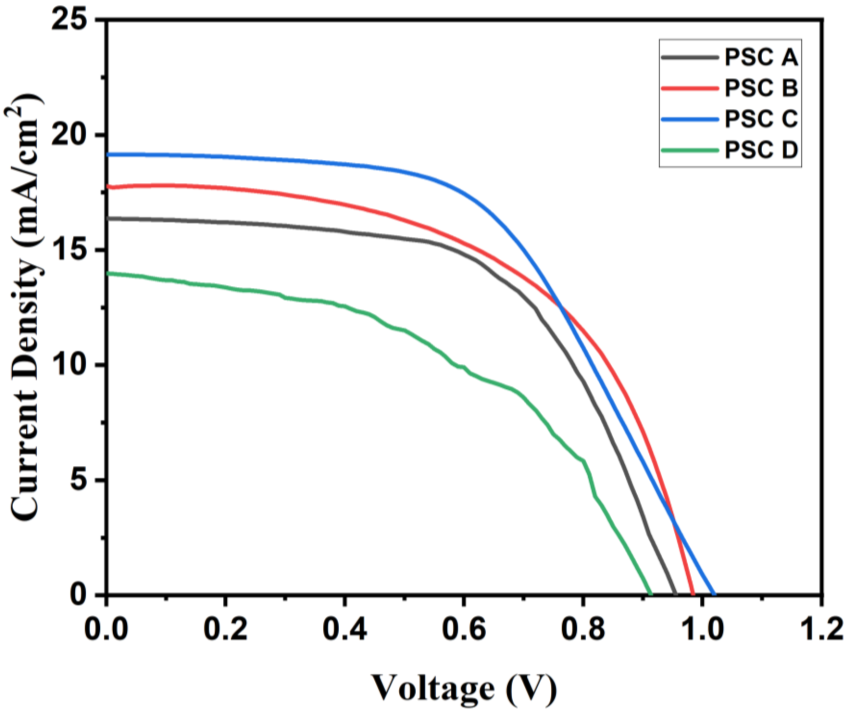

Figure 4.10: Current density vs voltage (J-V) curve of four ZNRs based PSCs fabricated on different ZnO seed layers

The highest EQE is obtained in PSC C, which again confirms its superior performance over the other three devices. Photon corresponding to this wavelength is well absorbed in the PSC C, and the generated charge carriers are transported effectively to the electrode. However, a significant improvement in the EQE of PSC B is also observed due to the growth of less defective ZNRs in a particular direction, which enhances the considerable absorption of light and also helps in collecting the generated charge carriers.

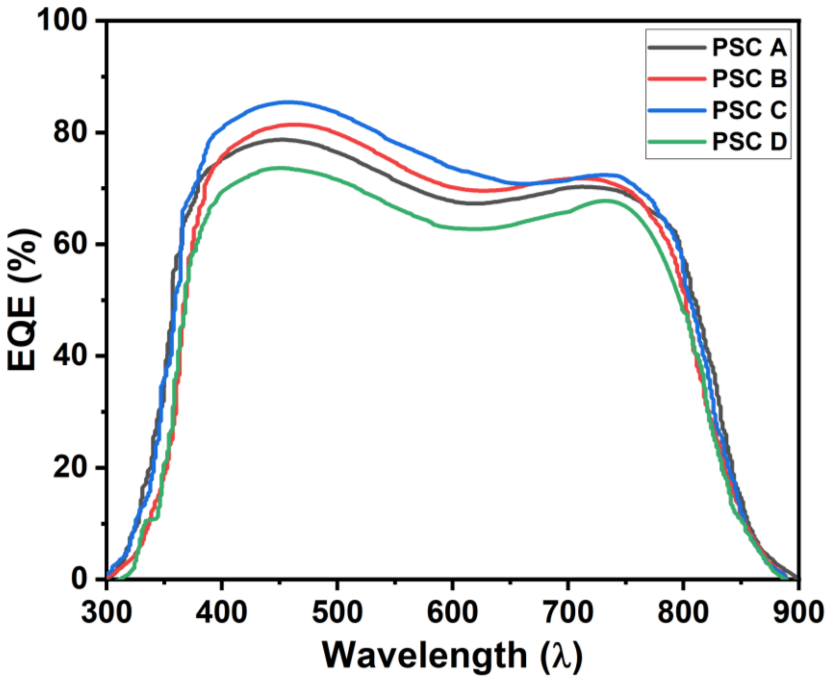

Figure 4.11: External quantum efficiency (EQE) of PSCs A, B, C, and D

4.4 Conclusion

The different types of seed layers based PSCs are fabricated and characterized for the performance improvement in the present chapter. The FTO/seed layer/ ZNRs/$CH_3NH_3PbI_3$/PTAA/Au structure is implemented on the glass substrate. The identical growth technique is used for the ZNRs in four types of seed layer based PSCs. The comparative study shows that the ZNRs grown on the ZnO QDs seed layer is more suitable for the perovskite-based solar cells. The current density (J_{SC}) of 19.14 mA/cm^2, V_{OC} of 1.01, fill factor of 0.64, and PCE of 10.69% have been achieved for ZnO QDs seed layer based PSC. The improvement in the solar parameters is attributed to the well align ZNRs grown on the seed layer with smaller particle size (ZnO QDs), directly affecting the V_{OC} and FF of the PSC. ZnO QDs based seed layer on the FTO substrate is uniform and more compact, which provides better nucleation sites for the vertically aligned ZNRs with a high surface to volume ratio.

CHAPTER 5

Effect of Doped Spiro-OMeTAD Based HTL on the Performance of FTO/ZnO Nanorods/$CH_3NH_3PbI_3$/Spiro-OMeTAD/Pd Perovskite Solar Cells*

Contents

*Part of this work has been published as:

1. Jarwal, Deepak Kumar, et al. "Fabrication and TCAD validation of ambient air-processed ZNRs/$CH_3NH_3PbI_3$/Spiro-OMeTAD solar cells." *Superlattices and Microstructures* (2020).

CHAPTER 5

Effect of Doped Spiro-OMeTAD Based HTL on the Performance of FTO/ZnO Nanorods/$CH_3NH_3PbI_3$/Spiro-OMeTAD/Pd Perovskite Solar Cells

5.1 Introduction

We have investigated the performance characteristics of FTO/ZnO Seed Layer/ZnO Nanorods/$CH_3NH_3PbI_3$/PTAA/Au where ZnO nanorods (ZNRs) have been synthesized from the four different types seed layers by hydrothermal method in Chapter-4. The ZNRs have increased mobility, easy synthesis, low-temperature processing, and high stability [115], [126], [165]. Although ZNRs based PSCs have good power conversion efficiency (PCE), some modification is required in the synthesis process of ZNRs to remove voids and traps on the surface. Son et al. [90] have reported the maximum PCE of 14.35% using $(NH_4)_2TiF_6$ treated ZNRs based ETL in the PSCs. The surface-treated ZNRs minimize the recombination for the generated charge carriers. On the other hand, the use of doping engineered hole transport layer (HTL) in the PSCs improves their efficiency, stability, and environment-friendly operations [127], [166]-[168]. It is found that the mobility/conductivity of spiro-OMeTAD can be increased by appropriate doping. The common p-type dopants to the spiro-OMeTAD are bis(trifluoromethane) sulfonamide lithium salt (Li-TFSI) and 4-tert-butylpyridine (TBP) [166]. It is observed that lithium salt helps in the oxidation process of spiro-OMeTAD, whereas TBP improves the conductivity of the active layer by dissolving in the perovskite layer [169]. In this chapter, we will investigate the effects of doped HTL based ZNRs/$CH_3NH_3PbI_3$/Spiro-OMeTAD based hybrid PSCs using LiTFSI and TBP dopants. The experimental results have been compared with the commercially available SetFos^{TM} TCAD simulation data for their validation. The outline for the rest of this chapter is as follow:

Section 5.2 describes the details of the synthesis process of ZNRs and the fabrication steps of PSCs. The simulation methodology and the factors affecting the parameters of simulated solar cells are discussed in Section 5.3. The measurement results, their comparison with simulated results, and discussion are presented in Section 5.4. Finally, Section 4.5 summarizes the finding and observations of this chapter.

5.2 Experimental Details

5.2.1 Thin Film Growth and Perovskite Solar Cells Fabrication

FTO coated glass substrate in 15 mm × 15 mm square size was cleaned ultrasonically step by step in a soap solution, acetone, and isopropanol, respectively, for 15 minutes each [170]. The wet cleaned substrates were kept in the plasma chamber for 10 minutes for dry cleaning under nitrogen and argon flow to make the surface more hydrophilic. Two types of PSCs with fixed ZnO NRs ETL and variation in HTL (undoped and spiro-OMeTAD) were fabricated on FTO coated glass substrates. First of all, the ZnO QDs solution was prepared using dissolving zinc acetate dihydrate in 2-methoxy ethanol at 60^0 C and stirred for 24 hours under an inert environment (Nitrogen gas) [171]. Further, the solution was filtered using a 0.22 um PVDF membrane to remove uncreated particles. A very thin seed layer of as-synthesized ZnO quantum dot was deposited using a spin coating on cleaned FTO substrate to make uniformly distributed ZnO nanorods. The ZnO NRs were grown on ZnO QDs coated FTO substrate using a solvothermal process [154]. In brief, the precursor solution was prepared by mixing of 500 mM zinc acetate and 500 mM HTMA in de-ionized (DI) water. The mixed precursor solution was then transferred in Teflon lined cylindrical autoclave. The ZnO coated FTO substrates were kept in an autoclave with an angle. The autoclave was moved in a digital muffle furnace at a constant temperature of 95^0 C for 4 hours to obtain ZnO NRs with an average length of 400 nm. After the growth of ZnO NRs, the samples were rinsed in DI water for removal of unreacted salts and annealed at 250^0 C for 1 hour to make a fully crystalline phase. Further, surface modification using $TiCl_4$ treatment was performed by dipping in 40 mM $TiCl_4$ solution in DI water for 30 minutes at 70^0 C [116]. The $TiCl_4$ treatment overcomes the separation between two consecutive ZnO NRs. The perovskite was deposited on grown ZnO NRs using two-step spin coating methods. The precursor solution was prepared by dissolving 462 mg lead iodide (PbI_2) and 10 mg methylammonium iodide (CH_3NH_3I) in 1 ml DMF and 1 ml isopropanol, respectively. Both the inorganic material (PbI_2) and organic material (CH_3NH_3I) were deposited on grown ZnO NRs sample using spin coater (SPM-150LC, GmbH). The precursor's solutions of PbI_2 and CH_3NH_3I were deposited at 2000 and 3000 rpm, respectively, for 30 seconds. The overall thickness of 300 nm was achieved for the perovskite film. The obtained perovskite layer (active layer) was annealed at 90°C for 30 minutes to evaporate the solvent. Further, HTL of undoped spiro-OMeTAD and doped spiro-OMeTAD (dopant are LiTFSI and TBP) were deposited separately for the identical thickness of 80 nm [172]. Finally, 100 nm Pd was deposited using a thermal evaporation coating unit (Hind High Vac, model smart coat 3.0A) at a vacuum of 2×10^{-6} mbar. The fabrication steps for the proposed PSCs have been illustrated in Figure 5.1 (a). The complete device structure (FTO/ ZNRs/Perovskite/Spiro-OMeTAD/Pd) of the fabricated PSCs is shown in Figure 5.1(b).

5.2.2 Film and Device Characterization

The surface roughness is measured by atomic force microscopy (AFM, model: NaioAFM from Nanosurf, Switzerland) in dynamic mode. The surface morphology was taken by high resolution scanning electron microscope-HRSEM (Nova Nano SEM 450, FEI, USA). The absorbance spectra were obtained using UV-VIS spectroscopy (Jesco Corp.). The current density-voltage characteristic was obtained using a parameter analyzer (KeySight, B1500A). The light of one sun (100 mW/cm^2) was obtained from a solar simulator (Model: SS50AAA, AM 1.5G Photo Emission Tech Inc, USA). The external quantum efficiency (EQE) of the PSC was measured using a digital multimeter (Agilent, 34410A) and a monochromator (Princeton Instruments, SP2150i). The optical power density of the light sources (Halogen lamp, 150 watts) was measured using a PM100D (from Thorlabs) detector.

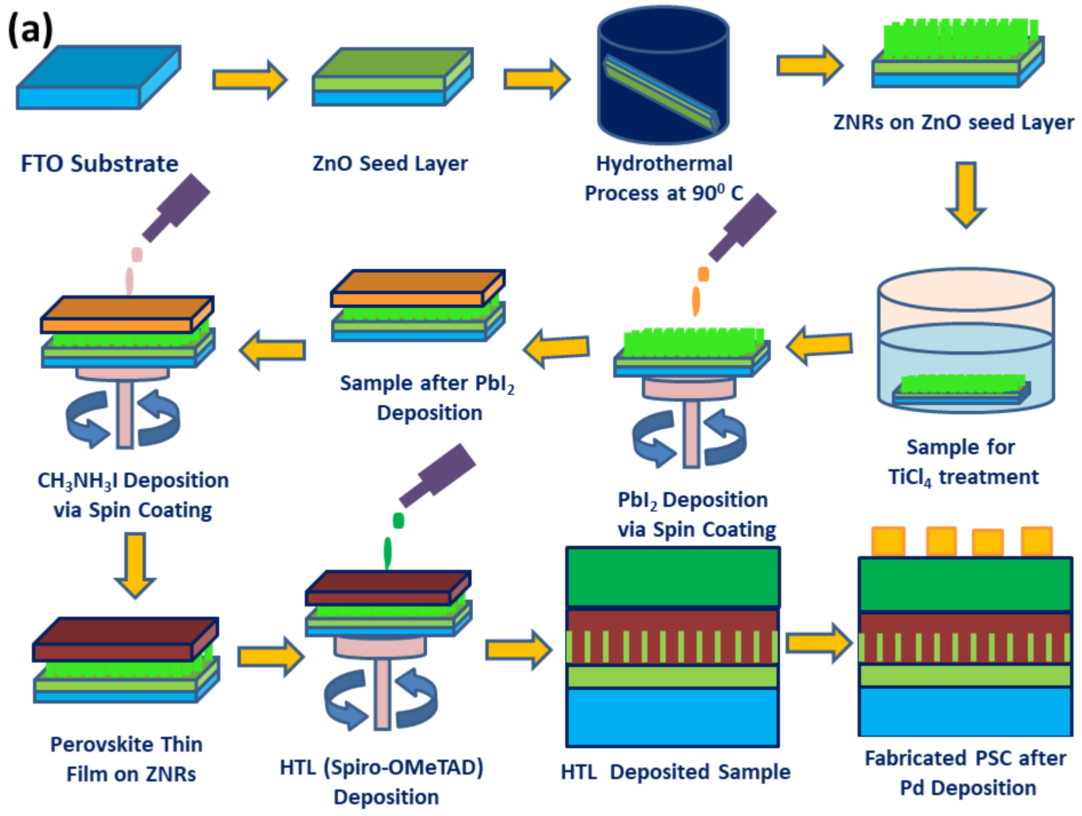

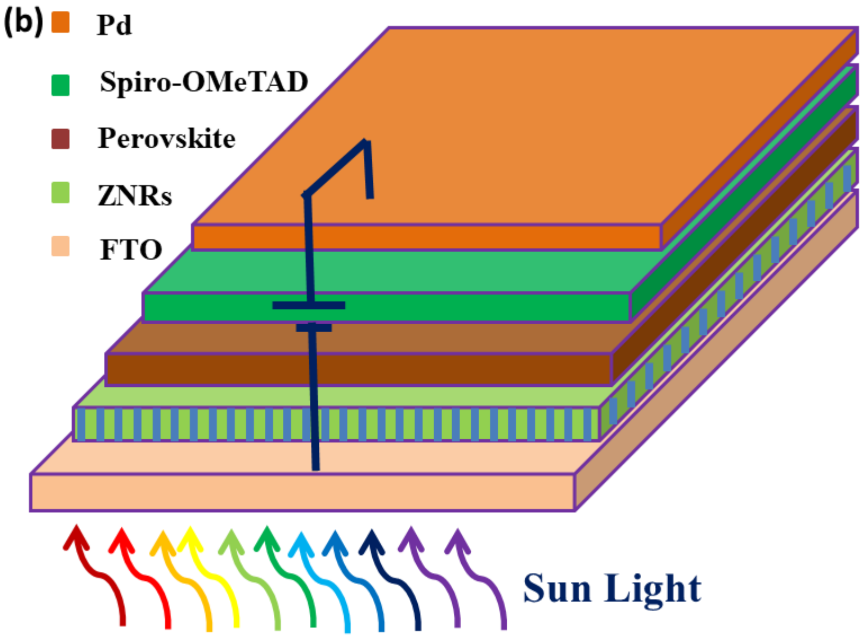

Figure 5.1: (a). Fabrication flowchart for the PSCs; (b) Complete device structure of the fabricated PSCs.

5.3 TCAD Simulation and Models

The carrier transportation in the proposed device structure is illustrated using a band diagram shown in Figure 5.2 (a). It can be observed that spiro-OMeTAD performs well as efficient HTL. The HTL efficiency improves further under doped condition. The fabricated device structure shown in Figure 5.2 has been considered for the simulation. The equivalent circuit [170] for the fabricated and simulated PSC is shown in Figure 5.2 (b). The current-voltage equation for the equivalent circuit is given as [173]:

$$J = J_0\{\exp[(q(v - JR_S))/\eta K_B T] - 1\} + \frac{V - JR_S}{R_{Sh}} - J_{ph} \tag{5.1}$$

Here, J and J_{ph} are the dark and photon current of the device. The J_0, q, η, K_B, R_S, R_{Sh} are the reverse saturation current density, carrier charge, ideality factor, Boltzmann constant, series resistance, and shunt resistance, respectively. The numerical simulation has been performed using SetFos^{TM} (from Fluxim) TCAD simulation tool. The parameters used for the device simulation of the PSC are shown in Table 5.1.

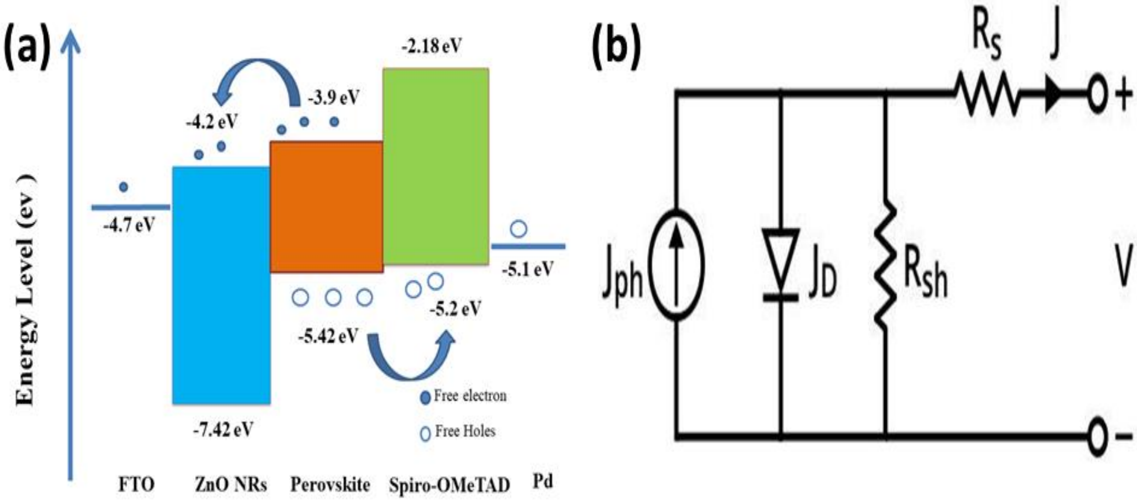

Figure 5.2: (a) Energy band diagram of perovskite solar cell and (b) Equivalent electrical circuit.

Table 5.1: Different parameters used in the simulation of PSCs.

Parameters	**ZNRs (ETL)** [126], [127], [174]	**Perovskite** [126], [127]	**Spiro-OMeTAD (HTL)** [122], [175], [176]	**Doped Spiro-OMeTAD (HTL)** [166], [169], [177]
Dielectric constant (ε_r)	9	10	3	3
Band gap (eV)	3.2	1.5	3	2.96
Electron affinity (χ)	3.9	3.85	2.45	2.45
Electron mobility (cm^2/V-s)	10	2.2	3.6×10^{-4}	1.6×10^{-3}
Hole mobility (cm^2/V-s)	2	2.2	3.6×10^{-4}	1.6×10^{-3}
VB effective DOSs (cm^{-3})	1×10^{18}	3×10^{18}	1.8×10^{19}	1.8×10^{19}
CB effective DOSs (cm^{-3})	1×10^{18}	1×10^{18}	2.2×10^{18}	2.2×10^{18}
Defect density (cm^{-3})	1×10^{14}	1×10^{15}	1×10^{13}	1×10^{13}
Acceptor concentration (cm^{-3})	0	1×10^{17}	1×10^{16}	1×10^{17}
Donor concentration (cm^{-3})	1×10^{19}	1×10^{17}	0	0

The simulation tool solves the following Poisson and continuity equation [178]:

$$\nabla^2 \varphi = \frac{q}{\varepsilon}(n - p + N_A + N_D) \tag{5.2}$$

$$\nabla . J_n = q\frac{\partial n}{\partial t} + q.R \tag{5.3}$$

$$\nabla . J_p = -q\frac{\partial p}{\partial t} - q.R \tag{5.4}$$

Where ψ, N_A, and N_D are the electrostatic potential, acceptor, and donor concentration, respectively. The parameters R, J_n, and J_p are the rate of recombination, electrons, and holes current density, respectively. The drift-diffusion mechanism for electron and hole conduction is taken in the model. Here, drift phenomena is influenced by the internal electric field and the diffusion mechanism is happened due to concentration gradient. The equations used for drift-diffusion of electrons and holes conduction are:

$$J_n = q\mu_n nE + qD_n \nabla_n \tag{5.5}$$

$$J_p = q\mu_p nE + qD_p \nabla_p \tag{5.6}$$

Where μ_n, μ_p are the mobility of electron and hole. D_P and D_n are the diffusion coefficient for holes and diffusion coefficient for electrons.

5.4 Results and Discussion

In this section, first perovskite thin film and charge transport layers are characterized, and then solar cell characteristics are presented and discussed in detail.

5.4.1 Thin Film Characterization

The performance of the perovskite solar cell is improved by controlling the diameter and length of ZnO NRs. The ZnO NRs length is a function of the growth time, synthesis temperature, and the precursor concentration. The transmittance spectra of ZnO NRs treated with $TiCl_4$ is shown in Figure 5.3 (a). The relation between transmittance and absorbance is given as [116]:

$$A(\%) = -log_{10}T$$

The characteristic plot of the optical bandgap and the absorbance coefficient has been shown in Figure 5.3 (b). The relation between the optical band gap and the absorbance coefficient is given by equation [128]:

$$\alpha h\upsilon = A(h\upsilon - E_g)^m \tag{5.7}$$

Where, h, v, E_g, A, and m are Planck constant, frequency of light, optical band gap, absorbance, and material constant. And, $\alpha = 2.33\log\left(T/d\right)$ is the absorbance coefficient; where T is transmittance and d is film thickness. The estimated bandgap of the synthesized ZnO NRs is ~3.2 eV.

The surface roughness of ZNRs without treated and with $TiCl_4$ treated has been analyzed in dynamic mode. The obtained surface images are shown in Figure 5.4 (a) and (b). The surface roughness is expressed in terms of root-mean-square (rms) roughness values. The untreated ZnO NRs surface has rms roughness of 132 nm, whereas the $TiCl_4$ treated ZnO NRs surface has rms roughness of 110 nm. On the other hand, the deposited perovskite film has minimized the roughness on the surface. The roughness of the perovskite deposited surface is shown in Figure 5.4 (c). The rms roughness is reduced to 80 nm on the perovskite deposited surface. The HRSEM image of ZnO QDs thin film (seed layer) on FTO is depicted in Figure 5.5 (a). The optimized ZnO NRs with an average length of ~450 nm and diameter of ~80 nm are synthesized as measured from the HRSEM image shown in Figure 5.5 (b).

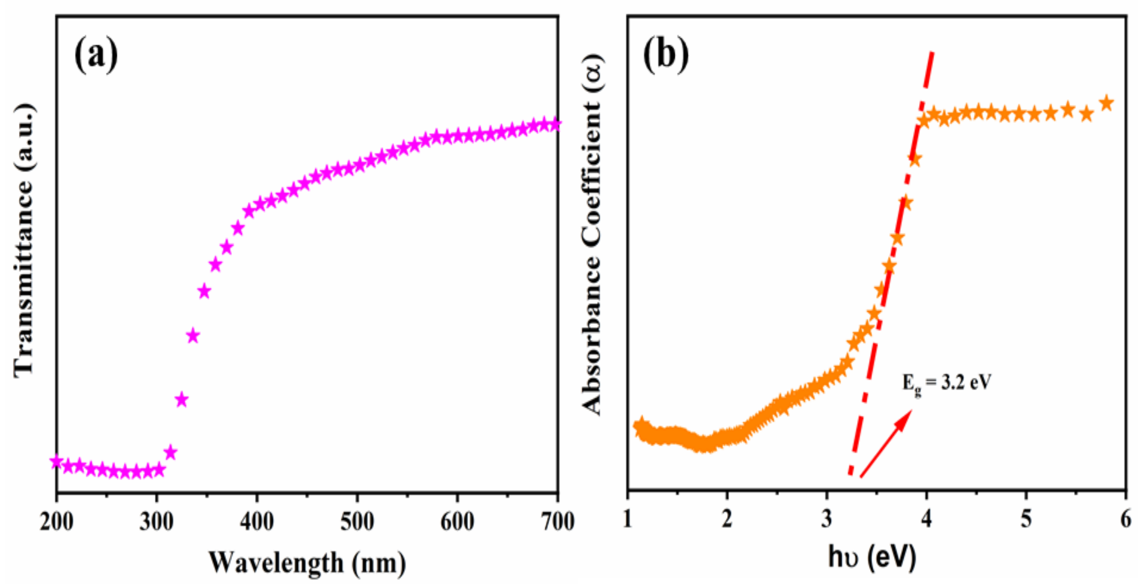

Figure 5.3: (a) Transmitance spectra of ZnO NRs and (b) Tauc plot for ZnO NRs.

The grain size and surface morphology of perovskite thin film deposited on ZnO NRs are depicted in Figure 5.5 (c). The thickness of perovskite film over ZnO NRs measured using cross-sectional HRSEM image is shown in Figure 5.5 (d).

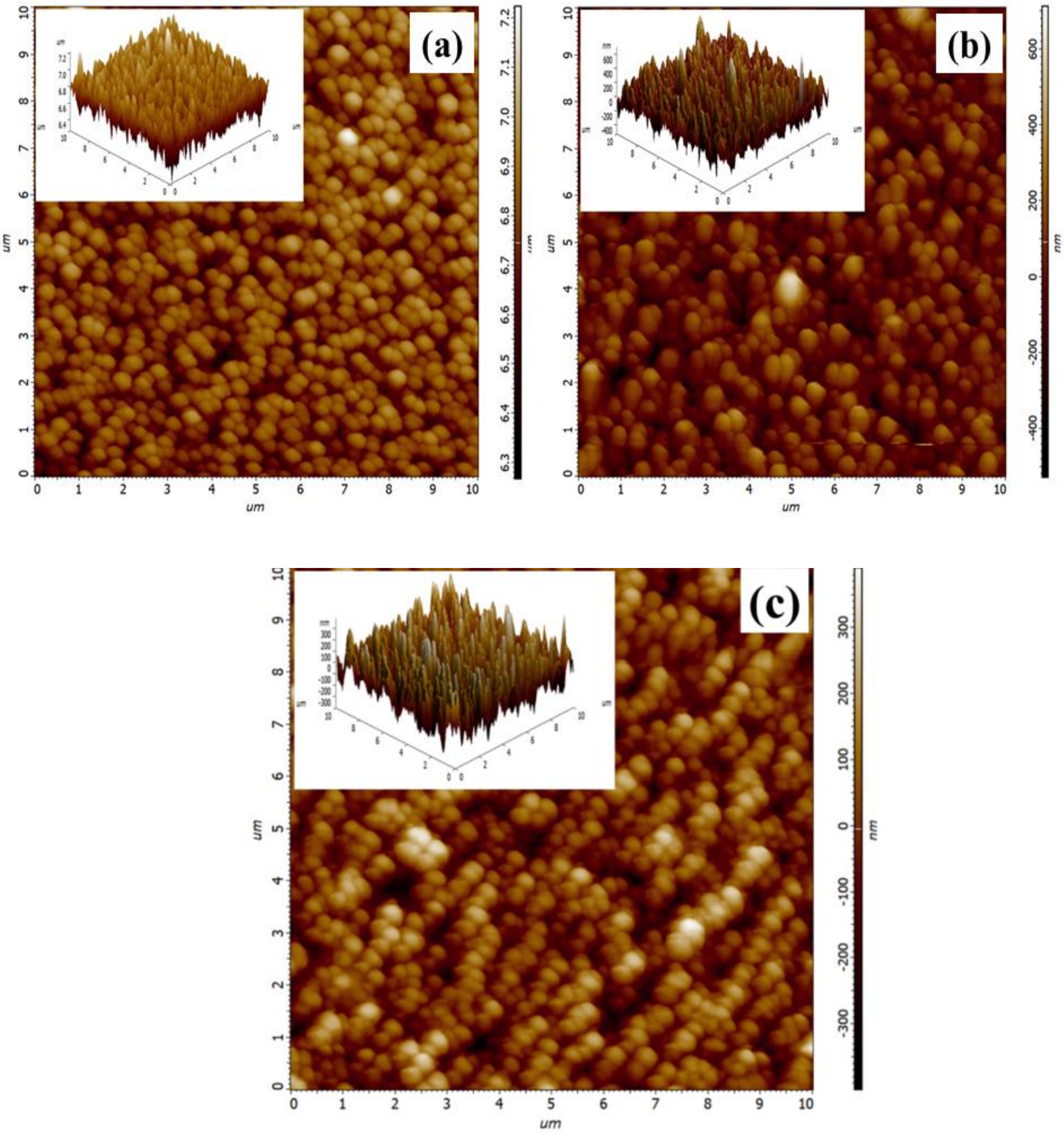

Figure 5.4: AFM image of (a) ZnO NRs without $TiCl_4$ treated, (b) ZnO NRs with $TiCl_4$ treatment, and (c) Perovskite layer on ZnO NRs

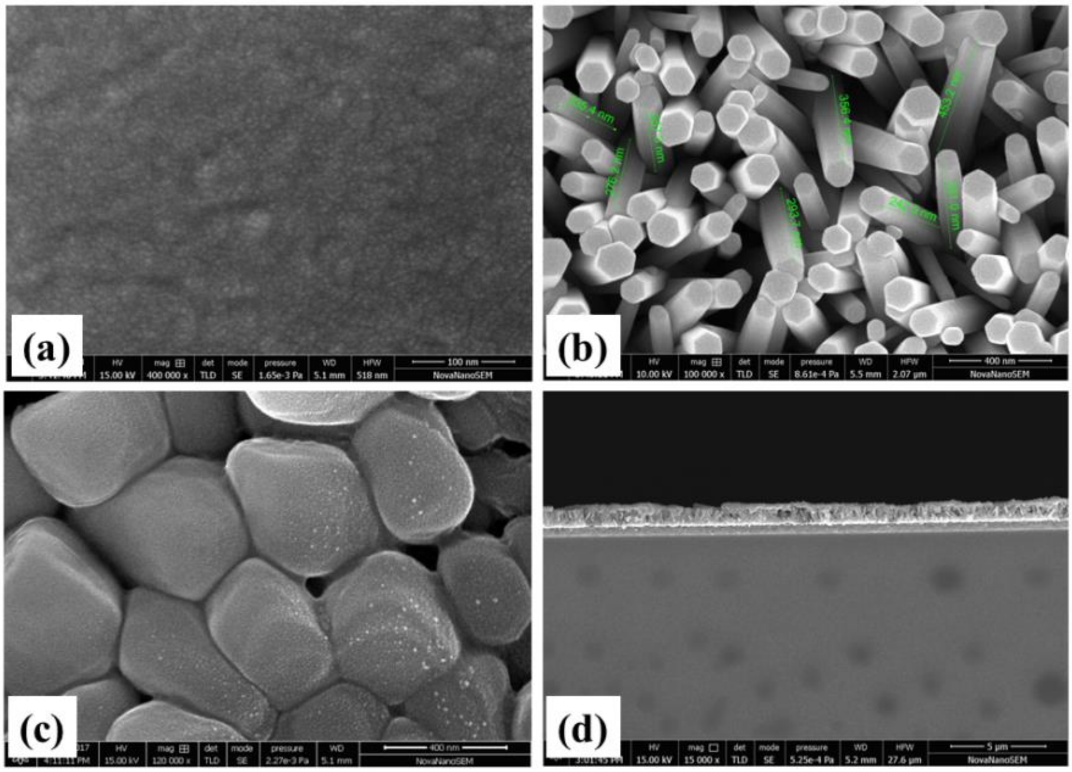

Figure 5.5: HRSEM image of (a) ZnO quantum dot, (b) Solvothermally synthesized ZnO NRs, (b) Perovskite thin film on ZnO NRs, and (d) Cross-sectional image of perovskite layer on ZnO NRs.

5.4.2 Solar Cell Characterization

The performance of PSC depends on the electrical and optical properties of HTM, ETM, and active layer materials. The film thickness for these layers has been optimized for the enhanced performance parameters of the PSCs. The ETL made of consecutive-grown ZnO NRs have some gap in the adjacent rods, and this void will lead to leakage current, which enhances the dark current. This also increases defect density, which reduces the performance of PSCs. Thus, the $TiCl_4$ treated ZnO NRs were used as ETL in the PSC structure. $TiCl_4$ treatment of ZnO NRs at an optimized temperature creates an ultrathin layer of TiO_2, which makes ZnO/TiO_2 core-cell structure [179]. The $TiCl_4$ treatment enhances the chemical stability of ZnO NRs and reduces the voids/defects. The two types of HTL (undoped spiro-OMeTAD and doped spiro-OMeTAD) based

PSCs have been characterized for their performance. It is observed that the doping reduces the impedance in the doped spiro-OMeTAD, as shown in the Nyquist plot in Figure 5.6 (a). This reduced impedance is due to increased carrier density in the doped spiro-OMeTAD, which results in improved PSC parameters. The impedance characteristics have been recorded over a frequency range of 1 kHz to 1 MHz under 100 mW/cm^2 (1.5 AM) illumination at a bias voltage of 900 mV. Based on impedance characteristics, the equivalent circuit for the PSCs having a series resistance as well as R_{rec} and C_{rec} in parallel combination along with R_{HTL} and C_{HTL} in parallel combination is shown in Figure 5.6 (b). Where series resistance (R_S) is related to contact resistance of individual layers and electrodes (Pd and FTO). The high-frequency region describes the behavior of hole diffusion in the HTL layer, which is denoted by the parallel combination of R_{HTL} and C_{HTL}. Whereas the lower frequency region shows the parallel combination of recombination resistance (R_{rec}) and capacitance (C_{rec}), which is related to the Fermi level of ETL [180]. The PSC with a doped HTL layer shows a smaller semicircle, which represents the better charge transportation compare to undoped HTL based PSCs [181]. Imaginary impedance (Z”) vs. frequency graph has been shown in Figure 5.7 (a). This graph explains about the relaxation frequency, and the relaxation frequency is inversely proportional to relaxation time, i.e. ($f_{max} \alpha 1/ \tau$). It can be seen from Figure 5.7 (a) that the relaxation frequency peak in doped HTL based PSC is shifted towards a higher frequency region in comparison to undoped HTL based PSCs, which implies a fast charge transportation rate in doped PSCs [181]. The relaxation time defines the charge transfer rate at the interface of the transport layer with the active layer. For the fast separation rate of the charge carrier, the relaxation time should be lower. Further, Figure 5.7 (b) shows the frequency-dependent real part of the impedance, which corresponds to the R_{HTL} [180]. In Figure 5.7 (b), the PSC with doped spiro-OMeTAD shows a lower value of impedance as compared to the PSC with undoped spiro-OMeTAD, which confirms the transport layer exhibit the better interface in doped spiro-OMeTAD based PSC [182] that results in better performance.

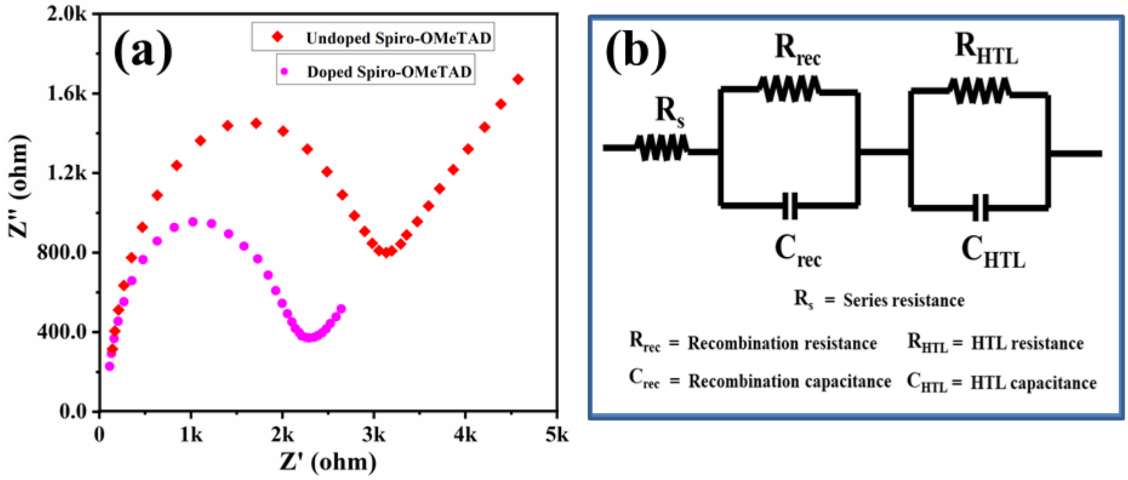

Figure 5.6: (a) Nyquist plot for fabricated PSC with undoped and doped HTL layer; (b) Equivalent circuit model employed using impedance characteristics.

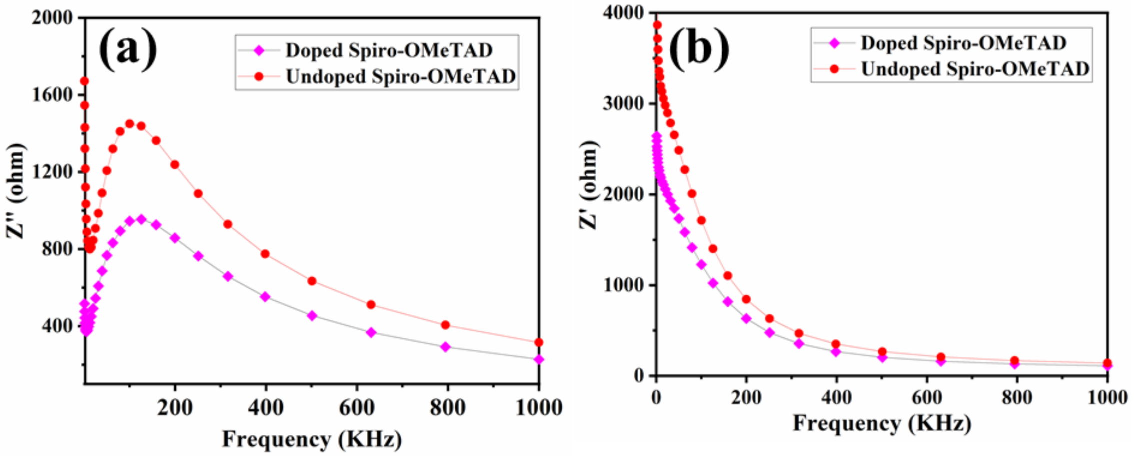

Figure 5.7: (a) Imaginary impedance vs. frequency plot, and (b) Real impedance vs. frequency plot of fabricated PSCs

The obtained electrical characteristics using the current-density vs. voltage (J-V) curve of the fabricated PSCs have been shown in Figure 5.8 (a) and 5.8 (b). Whereas the extracted parameters from the experimental finding (as shown in Table 5.1) are used in the TCAD simulation to obtain the electrical characteristic of the solar cells as in Figure 5.8 (a) and (b). It is found that the simulated results are in good agreement with the experimental for both types of PSCs. The calculated solar parameters namely V_{OC}, J_{SC}, *FF*, and *PCE* from *J-V* characteristics of Figure 5.8 (a) are 0.98 V, 15.84 mA/cm^2, 61%, and 9.51 %, respectively for fabricated, whereas 1.001 V, 15.83 mA/cm^3, 0.60%, and 10.13%, respectively for simulated undoped spiro-OMeTAD based PSC. On the other hand, V_{OC}, J_{SC}, *FF*, and *PCE* calculated from *J-V* characteristics of Figure 5.8 (b) are found as 1.01 V, 18.53 mA/cm^2, 64%, and 10.18%, respectively for fabricated, whereas 1.001 V, 17.27 mA/cm^3, 0.66%, and 11.53%, respectively for simulated doped spiro-OMeTAD based PSC. The calculated solar parameters are compared in Table 5.2. The improved solar parameters in doped spiro-OMeTAD based PSC is due to increased charge carrier density and better band alignment.

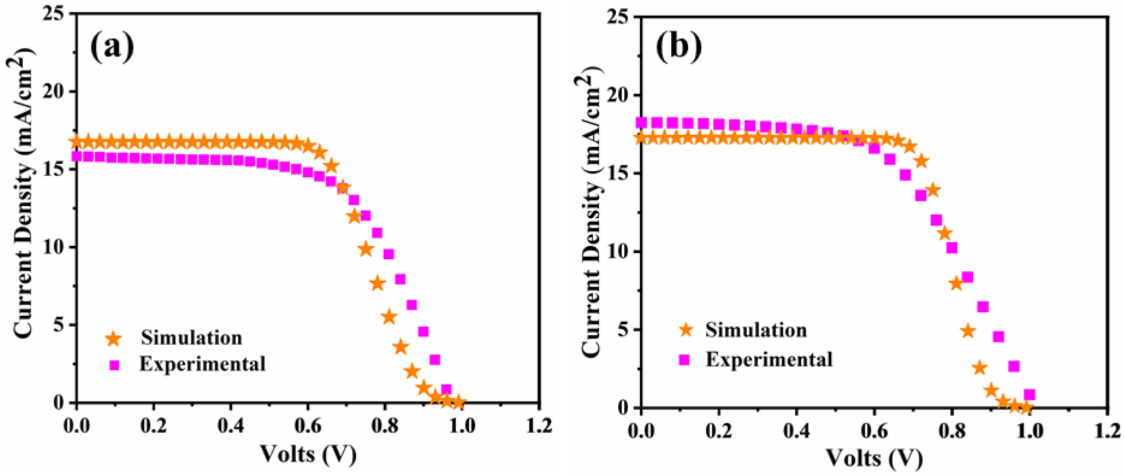

Figure 5.8: Current density vs. voltage curve for (a) Undoped spiro-OMeTAD and (b) Doped spiro-OMeTAD.

The external quantum efficiency (EQE) for both types of PSCs has been calculated from wavelength versus photocurrent characteristics. The monochromatic light of 350 nm to 800 nm is illuminated to the PSCs, and the corresponding photocurrent is measured. The ratio of obtained photocurrent and optical power of incident light is defined as the responsivity (R) for the PSCs [183]. The EQE of the PSC is calculated using the responsivity characteristics [116]. The obtained EQE characteristics for both the PSCs have been shown in Figure 5.9 (a) and (b). It is observed that the EQE is slightly improved with doping and the simulated characteristics are in good agreement with the experimental.

Table 5.2: A comparison of fabricated and simulated PSC parameters.

	Simulation (Undoped spiro-OMeTAD)	Experimental (Undoped spiro-OMeTAD)	Simulation (Doped spiro-OMeTAD)	Experimental (Doped spiro-OMeTAD)
V_{OC} (V)	1.001	0.98 ± 0.1	1.001	1.01 ± 0.1
J_{SC} (mA/cm^3)	15.83	15.84 ± 0.35	17.27	18.53 ± 0.30
FF	0.60	0.61 ± 0.1	0.66	0.64 ± 0.1
PCE (%)	10.13	9.51 ± 0.2	11.53	10.18 ± 0.2

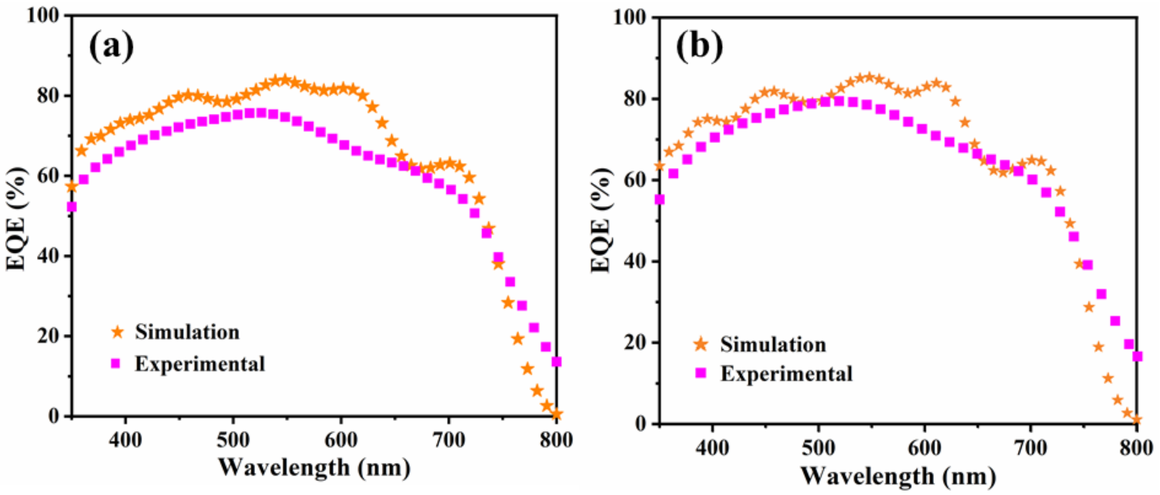

Figure 5.9: External quantum efficiency of (a) Undoped spiro-OMeTAD based PSC and (b) Doped spiro-OMeTAD based PSC.

5.5 Conclusion

In this chapter, the effect of both the undoped and doped spiro-OMeTAD HTL on the performance of a ZNRs ETL based FTO/ZNRs/Perovskite/Spiro-OMeTAD/Pd solar cell structure has been studied. The p-type dopant TBP and LiTFSI in the spiro-OMeTAD are used to improve the performance by enhancing the hole carrier density in the HTL. For undoped HTL, the proposed PSC gives an optimized *PCE* value of 10.18 % with V_{OC} of 1.01 V, J_{SC} of 18.57 mA/cm^2, and fill factor (*FF*) of 64% under ambient-air environment. However, improved performance with *PCE* of 11.53%, V_{OC} of 1.001 V, J_{SC} of 17.27 mA/cm^2, and *FF* of 0.66 are obtained for the doped spiro-OMeTAD HTL based PSC. The results have also been compared with the commercially available Set-Fos^{TM} TCAD tool for showing the reliability of the measured data. The reasonably good matching is observed between the experimental results and TCAD simulation data.

CHAPTER 6

Conclusion and Future Scope

Contents

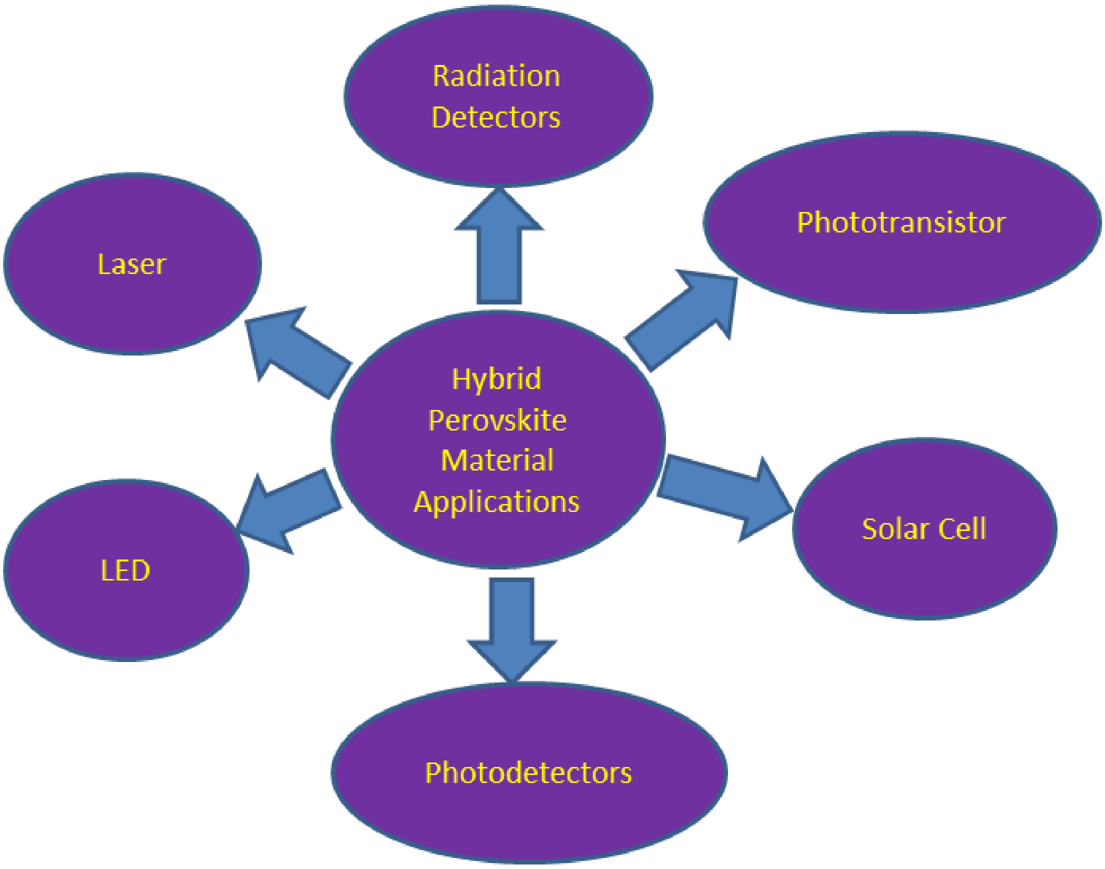

CHAPTER 6

Conclusions and Future Scope

6.1 Introduction

Perovskite materials are widely used in many optoelectronic applications, such as solar cells, photodetectors, laser, LED, electronic sensors, radiation detectors, image sensors, etc. Hybrid perovskite materials have been projected as one the most important 4th generation organic solar cell materials due to their possibility of bandgap tuning to achieve the power conversion efficiency (PCE) of more than 25%. In view of the above, the present thesis reports the fabrication, TCAD simulation and characterization of some $CH_3NH_3PbI_3$ hybrid perovskite solar cells (PSCs) with TiO_2 nanorods (TNRs)/ZnO nanorods (ZNRs) as the electron transport layer (ETL) and PTAA/ Spiro-OMeTAD hole transport layer (HTL). The major objectives of the thesis are to investigate the effects of thickness and morphological engineering of the ETL and doping engineering of the HTL on the performance optimization of the proposed PSCs in this thesis. Four types of $CH_3NH_3PbI_3$ hybrid perovskite based inverted PSC structures fabricated on the transparent fluorine doped tin oxide (FTO) substrates have been investigated in this thesis: FTO/TNRs/Perovskite/PTAA/Pd, FTO/TNRs/Perovskite/Spiro-OMeTAD/Pd, FTO/ZNRs/Perovskite/PTAA/Au and FTO/ZNRs/Perovskite/Spiro-OMeTAD/Pd. The perovskite thin film is used as an active layer (absorber layer), whereas Spiro-OMeTAD and PTAA are used as hole transport layers in solar cell structure. The fabrications and measurements have been carried out under robust open atmospheric conditions. That is why, the experimental results for FTO/TNRs/Perovskite/PTAA/Pd and FTO/ZNRs/Perovskite/Spiro-OMeTAD/Pd PSCs have been compared with the TCAD simulation data to show the deviations of the measured results under real environmental conditions from the ideal theoretical results. The present chapter summarizes the chapter-wise objectives and major findings of the thesis as described in the following:

6.2 Chapter-Wise Major Observations

Chapter-1 introduces the optoelectronic and photovoltaic properties of hybrid perovskite materials and their applications in solar cells, sensors, and LEDs. Different materials used for ETL and HTL and ETL/HTL engineering for the performance improvement of the PSCs are discussed. The optical and electrical characterization techniques such as spectrophotometry, XRD, TEM, SEM, UV-Vis spectroscopy, photoluminance spectroscopy, and impedance measurement used for the solar cells are also briefly discussed. A detailed literature survey has been carried out on the hybrid perovskite materials based solar cells. Literature surveys on various performance improvement techniques of the solar cells are also discussed. Based on the observations from the literature survey, the scopes of the thesis have been outlined at the end of this chapter.

Chapter-2 investigates the effect of ETL thickness on the electrical and optical characteristics of the FTO/TNRs/$CH_3NH_3PbI_3$/PTAA/Pd structure based perovskite solar cells (PSCs). The TNRs layer has been used for the ETL, PTAA as the HTL, and $CH_3NH_3PbI_3$ hybrid perovskite has been used for the active layer of proposed PSC. The TNRs are grown using the low-cost hydrothermal method at a temperature of 180^0 C, whereas both the $CH_3NH_3PbI_3$ active layer and HTL are deposited by the spin coating method. Both the fabrication processes and measurements are carried out in the open air condition for three proposed PSC devices with three different ETL thicknesses of 500 nm, 650 nm and 800 nm. The measured results have been compared with the TCAD simulation data to confirm the measured results with the ideal theoretical characteristics. The major observations of this chapter are listed below:

- The XRD pattern shows good crystallinity and rutile phase of the hydrothermally grown TNRs ETL.
- The effects of different ETL thicknesses on J_{SC}, V_{OC}, PCE, and EQE are compared for fabricated and simulated solar cells.
- The ETL thickness of 500 nm shows the best solar parameters for the proposed PSCs.
- The PCE of both the fabricated and simulated PSCs is decreased for ETL thickness above 500 nm.

- The optimum simulated values of V_{OC} (1.07), J_{SC} (23.71), FF (0.63) and PCE (15.69 %) against their corresponding experimentally measured values of V_{OC} (1.06), J_{SC} (22.19), FF (0.63) and PCE (15.04 %) are observed for the ETL thickness of 500 nm, perovskite thickness of 100 nm, and HTL thickness of 350 nm.

- The close proximity of the simulated electrical and optical characteristics with the experimentally measured results confirms that the TCAD tools can be effectively explored for other PSC structures.

Chapter-3 reports the effects of solvothermal etching and $TiCl_4$ treatment of the hydrothermally grown TNRs ETL of the electrical and optical characteristics of FTO/ZNRs/$CH_3NH_3PbI_3$/Spiro-OMeTAD/Pd structure based PSCs. The solvothermal etching is used to modify the surface morphology of the TNRs ETL. The performance parameters of the solvothermally etched ETL have been compared with those of PSCs with un-etched TNRs ETL. Fabrication and measurements are carried in a robust atmospheric condition with more that 60% humidity. The performance parameters of three types of PSCs have been carried out: (i) TNRs-based ETL without etching and $TiCl_4$ treatment (Device A); (ii) ETL with only $TiCl_4$ treatment but no etching of TNRs (Device B); and (iii) TNRs ETL with solvothermal etching followed by $TiCl_4$ treatment (Device C). The major observations are summarized below:

- The solvothermal etching of the TNRs ETL is shown to enhance the performance of fabricated PSC due to the increase in the effective surface-to-volume ratio of the ETL and absorption layers.
- The application of both the solvothermal etching followed by $TiCl_4$ treatment of the hydrothermally grown TNRs in "Device C" are observed to be the best among the three devices under study. This is attributed to the increased surface-to-volume ratio of the ETL by etching and increased carrier lifetime in the active layer owing to the reduced traps and voids by $TiCl_4$ treatment of the TNRs.
- The PCE, V_{OC}, J_{SC}, and FF of the fabricated champion device "C" are measured as 15.16 %, 1.04 V, 22.64 mA/cm2, and 0.64, respectively.
- The EQE of device "C" is also found to be the best among the three devices.

Chapter-4 investigates the electrical and optical performance characteristics of FTO/ZnO Seed Layer/ZNRs/$CH_3NH_3PbI_3$/PTAA/Au structure based PSCs where PTAA is used for HTL in the device. Four devices containing four different morphologies of ZNRs-ETLs grown by the hydrothermal method on four different types of seed layers (of drop-casted ZnO, spin-coated colloidal ZnO nanoparticles (NPs), spin-coated colloidal ZnO quantum dots (QDs), and hydrothermally grown ZnO NRs) were studied in this chapter. The major findings of the chapter are summarized below:

- The surface and structural morphologies of different types of ZNRs ETLs grown from different seed layers are analyzed by XRD and SEM measurements. The XRD confirms the uniform crystallinity of ZNRs while SEM confirms the growths of good quality ZNRs
- The PSC with the ZNRs-ETL grown from ZnO QDs based seed layer gives better electrical and optical performances over ZNRs-ETL based devices. The device shows improved shunt and series resistance over the other three devices.
- The values of J_{SC}, V_{OC}, FF and PCE of the ZnO QDs seed layer based PSC are 19.14 mA/cm^2, 1.01, 0.64, and 10.69% respectively.

Chapter-5 investigates the effects of doped and undoped spiro-OMeTAD based HTL on the performance of FTO/ZNRs/$CH_3NH_3PbI_3$/Spiro-OMeTAD/Pd solar cell. The hydrothermally grown ZNRs layer is used as the ETL of the device. The device parameters are compared for undoped and doped spiro-OMeTAD HTL based PSCs. The devices are fabricated and characterized in open air environment. The measured results have been compared with the numerical simulation data using Setfos^{TM} TCAD simulation tool for validating the measured data. The major observations of this chapter can be summarized as follows:

- The small molecules TBP and LiTFSI are used as additives in Spiro-OMeTAD to enhance the conductivity of the HTL layer. The doped Spiro-OMeTAD HTL based PSCs give better performance over the undoped Spiro-OMeTAD HTL based PSCs.

- For undoped HTL, the fabricated PSC gives an optimized *PCE* value of 9.51% with V_{OC} of 0.98 V, J_{SC} of 15.84 mA/cm^2, and fill factor (*FF*) of 61% under ambient-air environment. However, improved performance with *PCE* of 10.18%, V_{OC} of 1.01 V, J_{SC} of 18.57 mA/cm^2, and *FF* of 64% are obtained for the doped Spiro-OMeTAD HTL based PSC.
- The results are compared with the commercially available SetFos™ TCAD tool for showing the reliability of the measured data. Reasonably good matching is observed between the experimental results and TCAD simulation data.
- In simulated PSC, the PCE, V_{OC}, J_{SC}, and FF for undoped and doped HTL devices are observed as 10.13%, 1.001 V, 15.83 mA/cm^3, and 0.60: and 11.53%, 1.001 V, 17.27 mA/cm^3, and 0.66, respectively.

6.3 Future Scope of Work

- The PSCs based on the organic ETL and HTL can be fabricated on flexible substrates such as polyamide, PET, PEN, etc., for the flexible device.
- 2D/3D perovskite can be introduced as an active layer to make more stable PSCs.
- The introduction of perovskite quantum dots with a suitable bandgap can enhance photo absorbance in perovskite material.
- Doping of lanthanide materials can also be used to improve the device efficiency by up conversion and down conversion phenomenon.

- The blending of nanoparticles in ETL as a metamaterial can be used as an anti-reflection layer and enhanced optical properties by the plasmonic effect.

- Composites of graphene with metal oxides (ZnO, TiO_2, SnO_2, etc.) can be used as ETL in PSCs for fast charge transportation in the photovoltaic device.
- Multifunction tandem architecture could be explored to overcome the Shockley-Quiesser limit by utilizing larger spectrum absorbance.

REFERENCES

[1] "Renewable-vs-nonrenewable-energy-resources12071170@sciencing.com,"2020 . [Online]. Available: https://sciencing.com/renewable-vs-nonrenewable-energy-resources-12071170.html.

[2] Z. L. Wang and W. Wu, "Nanotechnology-enabled energy harvesting for self-powered micro-/nanosystems," *Angew. Chemie - Int. Ed.*, vol. 51, no. 47, pp. 11700–11721, 2012.

[3] "8c6657c74af31ecc277be217d899f91919d2d078@ www.renewableenergyworld.com," 2020. [Online]. Available: https://www.renewableenergyworld.com/types-of-renewable-energy/what-is-solar-energy/#gref.

[4] A. Mohammad Bagher, "Types of Solar Cells and Application," *Am. J. Opt. Photonics*, vol. 3, no. 5, p. 94, 2015.

[5] R. Williams, "Becquerel photovoltaic effect in binary compounds," *J. Chem. Phys.*, vol. 32, no. 5, pp. 1505–1514, 1960.

[6] Goleman et al., "The Action of Light on Selenium," *J. Chem. Inf. Model.*, vol. 53, no. 9, pp. 1689–1699, 2019.

[7] Latimer Clark et al., "Effect of light on selenium during the passage of an electric current," *Nature*, vol. 7, no. 173. p. 303, 1873.

[8] W. Gryllis et al., "Scientific american supplement," *Sci. Am. INC.*, vol. 492, no. 492, pp. 7854–7856, 1885.

[9] "Einstein-and-the-photoelectric-effect @ www.britannica.com." 2020.

[10] R. S. Oh, "LIGHT-SENSTIVE ELECTRIC DEVICE," *UNITED STATES Pat. Off.*, 1946.

[11] D. M. Chapin, C. S. Fuller, and G. L. Pearson, “A new silicon p-n junction photocell for converting solar radiation into electrical power [3],” *J. Appl. Phys.*, vol. 25, no. 5, pp. 676–677, 1954.

[12] C. M. Kearns D., “Photovoltaic effect and photoconductivity in laminated organic systems.,” *J.Chem.Phys.*, vol. 29, pp. 950–951, 1958.

[13] C. W. Tang, “Two-layer organic photovoltaic cell,” *Appl. Phys. Lett.*, vol. 48, no. 2, pp. 183–185, 1986.

[14] A. I. Science, “New world record for solar cell efficiency at 46%,” *Fraunhofer Inst. Sol. Energy Syst. ISE*, no. 26, pp. 1–4, 2014.

[15] Ansari et al., “Frontiers, opportunities, and challenges in perovskite solar cell: A critical review,” *J. Photochem. Photobiol. C Photochem. Chem.*, vol. 35, pp. 1–24, 2018.

[16] A. Khatibi, F. Razi Astaraei, and M. H. Ahmadi, “Generation and combination of the solar cells: A current model review,” *Energy Sci. Eng.*, vol. 7, no. 2, pp. 305–322, 2019.

[17] S. Gharibzadeh *et al.*, “Record Open-Circuit Voltage Wide-Bandgap Perovskite Solar Cells Utilizing 2D/3D Perovskite Heterostructure,” *Adv. Energy Mater.*, vol. 9, no. 21, pp. 1–10, 2019.

[18] A. S. R. Bati, M. Batmunkh, and J. G. Shapter, “Emerging 2D Layered Materials for Perovskite Solar Cells,” *Adv. Energy Mater.*, vol. 10, no. 13, pp. 1–21, 2020.

[19] A. Walsh, “Principles of Chemical Bonding and Band Gap Engineering in Hybrid Organic − Inorganic Halide Perovskites,” *J. Phys. Chem. C*, vol. 119, p. 5755−5760, 2015.

[20] “52c44350d83bfdf4f4be39fa7355698d2a3ba1e4 @ www.osa-opn.org,” 2021. [Online].Available:https://www.osaopn.org/home/articles/volume_31/november_2020/features/perovskite_photovoltaics_the_road_ahead/.

[21] A. R. Chakhmouradian and P. M. Woodward, “Celebrating 175 years of perovskite research: A tribute to Roger H. Mitchell,” *Phys. Chem. Miner.*, vol. 41, no. 6, pp. 387–391, 2014.

[22] H.L. Wells, “Cesium and Potassium Lead Halides,” *Sheff. Sci. Sch.*, pp. 121–134, 1892.

[23] E. Sandor and W. A. Wooster, “Crystal Structure and Photoconductivity of Caesium Plumbohalides,” *Nature*, vol. 1, no. 1955, p. 1958, 1958.

[24] D. Weber, “$CH_3NH_3PbX_3$, a Pb(II)-System with cubic Perowskite structure,” *Z. Naturforsch., B J. Chem. Sci.*, vol. 1445, no. August, pp. 1443–1445, 1978.

[25] Z. Yi, N. H. Ladi, X. Shai, H. Li, Y. Shen, and M. Wang, “Will organic-inorganic hybrid halide lead perovskites be eliminated from optoelectronic applications?,” *Nanoscale Adv.*, vol. 1, no. 4, pp. 1276–1289, 2019.

[26] B. A. Al-Asbahi, S. M. H. Qaid, M. Hezam, I. Bedja, H. M. Ghaithan, and A. S. Aldwayyan, “Effect of deposition method on the structural and optical properties of $CH_3NH_3PbI_3$ perovskite thin films,” *Opt. Mater. (Amst).*, vol. 103, no. March, pp. 1–9, 2020.

[27] R. Swartwout, M. T. Hoerantner, and V. Bulović, “Scalable Deposition Methods for Large-area Production of Perovskite Thin Films,” *Energy Environ. Mater.*, vol. 2, no. 2, pp. 119–145, 2019.

[28] K. Liang, D. B. Mitzi, and M. T. Prikas, “Synthesis and Characterization of Organic-Inorganic Perovskite Thin Films Prepared Using a Versatile Two-Step Dipping Technique,” *Chem. Mater.*, vol. 10, no. 1, pp. 403–411, 1998.

[29] T. Miyasaka, “Lead halide perovskites in thin film photovoltaics: Background and perspectives,” *Bull. Chem. Soc. Jpn.*, vol. 91, no. 7, pp. 1058–1068, 2018.

[30] G. E. Eperon, S. D. Stranks, C. Menelaou, M. B. Johnston, L. M. Herz, and H. J. Snaith, “Formamidinium lead trihalide: A broadly tunable perovskite for efficient planar heterojunction solar cells,” *Energy Environ. Sci.*, vol. 7, no. 3, pp. 982–

988, 2014.

[31] L. Peng, A. Tang, C. Yang, and F. Teng, “Size-controlled synthesis of highly luminescent organometal halide perovskite quantum dots,” *J. Alloys Compd.*, vol. 687, pp. 506–513, 2016.

[32] P. Fan *et al.*, “High-performance perovskite $CH_3NH_3PbI_3$ thin films for solar cells prepared by single-source physical vapour deposition,” *Sci. Rep.*, vol. 6, no. July, pp. 1–9, 2016.

[33] M. T. Neukom, “Charge Carrier Dynamics of Methylammonium Lead-Iodide Perovskite Solar Cells,” Albert-Ludwigs-University Freiburg, 2016.

[34] S. Agarwal and P. R. Nair, “Device engineering of perovskite solar cells to achieve near ideal efficiency,” *Appl. Phys. Lett.*, vol. 107, no. 12, 2015.

[35] H. Hu, “The fabrication, characterization and simulation of inverted perovskite solar cells,” 2019.

[36] A. Dubey *et al.*, “A strategic review on processing routes towards highly efficient perovskite solar cells,” *J. Mater. Chem. A*, vol. 6, no. 6, pp. 2406–2431, 2018.

[37] J. Burschka *et al.*, “Sequential deposition as a route to high-performance perovskite-sensitized solar cells,” *Nature*, vol. 499, no. 7458, pp. 316–319, 2013.

[38] D. Zhou, T. Zhou, Y. Tian, X. Zhu, and Y. Tu, “Perovskite-Based Solar Cells: Materials, Methods, and Future Perspectives,” *J. Nanomater.*, vol. 2018, 2018.

[39] M. Konstantakou, D. Perganti, P. Falaras, and T. Stergiopoulos, “Anti-solvent crystallization strategies for highly efficient perovskite solar cells,” *Crystals*, vol. 7, no. 10, pp. 1–21, 2017.

[40] A. E. Shalan, “Challenges and approaches towards upscaling the assembly of hybrid perovskite solar cells,” *Mater. Adv.*, vol. 1, no. 3, pp. 292–309, 2020.

[41] J. Albero, A. M. Asiri, and H. García, “Influence of the composition of hybrid perovskites on their performance in solar cells,” *J. Mater. Chem. A*, vol. 4, no.

12, pp. 4353–4364, 2016.

[42] T. Zhang, N. Guo, G. Li, X. Qian, L. Li, and Y. Zhao, "A general non-CH3NH3X (X = I, Br) one-step deposition of $CH_3NH_3PbX_3$ perovskite for high performance solar cells," *J. Mater. Chem. A*, vol. 4, no. 9, pp. 3245–3248, 2016.

[43] B. Cai, W. H. Zhang, and J. Qiu, "Solvent engineering of spin-coating solutions for planar-structured high-efficiency perovskite solar cells," *Cuihua Xuebao/Chinese J. Catal.*, vol. 36, no. 8, pp. 1183–1190, 2015.

[44] N. J. Jeon, J. H. Noh, Y. C. Kim, W. S. Yang, S. Ryu, and S. Il Seok, "Solvent engineering for high-performance inorganic-organic hybrid perovskite solar cells," *Nat. Mater.*, vol. 13, no. 9, pp. 897–903, 2014.

[45] R. Wei, "Modelling of Perovskite Solar Cells," Queensland University of Technology, 2018.

[46] J. Kang and J. H. Cho, "Organic-inorganic hybrid perovskite electronics," *Phys. Chem. Chem. Phys.*, vol. 22, no. 24, pp. 13347–13357, 2020.

[47] A. Kojima, "Novel Photoelectrochemical Cell with Mesoscopic Electrodes Sensitized by Lead-halide Compounds (11)," *ECS Meet. Abstr.*, no. 5, 2008.

[48] A. Kojima, K. Teshima, Y. Shirai, and T. Miyasaka, "Organometal halide perovskites as visible-light sensitizers for photovoltaic cells," *J. Am. Chem. Soc.*, vol. 131, no. 17, pp. 6050–6051, 2009.

[49] Z. Chu *et al.*, "Impact of grain boundaries on efficiency and stability of organic-inorganic trihalide perovskites," *Nat. Commun.*, vol. 8, no. 1, pp. 1–8, 2017.

[50] W. T. Wang, S. K. Das, and Y. Tai, "Fully Ambient-Processed Perovskite Film for Perovskite Solar Cells: Effect of Solvent Polarity on Lead Iodide," *ACS Appl. Mater. Interfaces*, vol. 9, no. 12, pp. 10743–10751, 2017.

[51] S. H. Turren-Cruz *et al.*, "Enhanced charge carrier mobility and lifetime suppress hysteresis and improve efficiency in planar perovskite solar cells," *Energy*

Environ. Sci., vol. 11, no. 1, pp. 78–86, 2018.

[52] N. Arora *et al.*, “Perovskite solar cells with CuSCN hole extraction layers yield stabilized efficiencies greater than 20%,” *Science (80-.).*, vol. 358, no. 6364, pp. 768–771, 2017.

[53] “Cell-Efficiency@Www.Nrel.Gov,” 2020. [Online]. Available: https://www.nrel.gov/pv/cell-efficiency.html.

[54] E. C. S. M. Abstracts, “Novel Photoelectrochemical Cell with Mesoscopic Electrodes Sensitized by Lead-halide Compounds (11),” *ECS Meet. Abstr.*, no. 11, 2008.

[55] J. A. Chang *et al.*, “High-performance nanostructured inorganicâ-organic heterojunction solar cells,” *Nano Lett.*, vol. 10, no. 7, pp. 2609–2612, 2010.

[56] J. H. Im, C. R. Lee, J. W. Lee, S. W. Park, and N. G. Park, “6.5% Efficient Perovskite Quantum-Dot-Sensitized Solar Cell,” *Nanoscale*, vol. 3, no. 10, pp. 4088–4093, 2011.

[57] H. S. Kim *et al.*, “Lead iodide perovskite sensitized all-solid-state submicron thin film mesoscopic solar cell with efficiency exceeding 9%,” *Sci. Rep.*, vol. 2, pp. 1–7, 2012.

[58] M. Liu, M. B. Johnston, and H. J. Snaith, “Efficient planar heterojunction perovskite solar cells by vapour deposition,” *Nature*, vol. 501, no. 7467, pp. 395–398, 2013.

[59] Bisquert, Juan and V. et al. Gonzalez-pedro, “General Working Principles of CH 3 NH 3 PbX 3 Perovskite Solar Cells,” *Nano Lett.*, vol. 14, pp. 2–5, 2013.

[60] A. K. Jena, A. Kulkarni, and T. Miyasaka, “Halide Perovskite Photovoltaics: Background, Status, and Future Prospects,” *Chem. Rev.*, vol. 119, no. 5, pp. 3036–3103, 2019.

[61] J. H. Im *et al.*, “Nanowire perovskite solar cell,” *Nano Lett.*, vol. 15, no. 3, pp.

2120–2126, 2015.

[62] V. E. Madhavan *et al.*, “CuSCN as Hole Transport Material with 3D/2D Perovskite Solar Cells,” *ACS Appl. Energy Mater.*, vol. 3, no. 1, pp. 114–121, 2020.

[63] G. Niu, X. Guo, and L. Wang, “Review of recent progress in chemical stability of perovskite solar cells,” *J. Mater. Chem. A*, vol. 3, no. 17, pp. 8970–8980, 2015.

[64] Z. Ning *et al.*, “Quantum-dot-in-perovskite solids,” *Nature*, vol. 523, no. 7560, pp. 324–328, 2015.

[65] H. S. Jung and N. G. Park, “Perovskite solar cells: From materials to devices,” *Small*, vol. 11, no. 1, pp. 10–25, 2015.

[66] G. Yang, H. Tao, P. Qin, W. Ke, and G. Fang, “Recent progress in electron transport layers for efficient perovskite solar cells,” *J. Mater. Chem. A*, vol. 4, no. 11, pp. 3970–3990, 2016.

[67] Jhong-Ciao Ke et al., “Effect of temperature annealing treatments and acceptors in CH3NH3PbI3 perovskite solar cell fabrication,” *J. Alloys Compd.*, pp. 2453–2457, 2017.

[68] C. Zhang, L. Gao, S. Hayase, and T. Ma, “Current advancements in material research and techniques focusing on lead-free perovskite solar cells,” *Chem. Lett.*, vol. 46, no. 9, pp. 1276–1284, 2017.

[69] F. Anwar, R. Mahbub, S. S. Satter, and S. M. Ullah, “Effect of Different HTM Layers and Electrical Parameters on ZnO Nanorod-Based Lead-Free Perovskite Solar Cell for High-Efficiency Performance,” *Int. J. Photoenergy*, vol. 2017, 2017.

[70] W. S. Li *et al.*, “Effect of substrate preheating on the photovoltaic performance of ZnO nanorod-based perovskite solar cells,” *Jpn. J. Appl. Phys.*, vol. 57, no. 6, 2018.

[71] P. S. Chandrasekhar, A. Dubey, and Q. Qiao, “High efficiency perovskite solar cells using nitrogen-doped graphene/ZnO nanorod composite as an electron transport layer,” *Sol. Energy*, vol. 197, no. December 2019, pp. 78–83, 2020.

[72] S. Zheng, G. Wang, T. Liu, L. Lou, S. Xiao, and S. Yang, “Materials and structures for the electron transport layer of efficient and stable perovskite solar cells,” *Sci. China Chem.*, vol. 62, no. 7, pp. 800–809, 2019.

[73] K. Mahmood, S. Sarwar, and M. T. Mehran, “Current status of electron transport layers in perovskite solar cells: materials and properties,” *RSC Adv.*, vol. 7, no. 28, pp. 17044–17062, 2017.

[74] Y. Wang, J. Wan, J. Ding, J. S. Hu, and D. Wang, “A Rutile TiO2 Electron Transport Layer for the Enhancement of Charge Collection for Efficient Perovskite Solar Cells,” *Angew. Chemie - Int. Ed.*, vol. 58, no. 28, pp. 9414–9418, 2019.

[75] Q. Jiang, X. Sheng, Y. Li, X. Feng, and T. Xu, “Rutile TiO2 nanowire-based perovskite solar cells,” *Chem. Commun.*, vol. 50, no. 94, pp. 14720–14723, 2014.

[76] H. Y. Yang, W. Y. Rho, S. K. Lee, S. H. Kim, and Y. B. Hahn, “TiO 2 nanoparticles/nanotubes for efficient light harvesting in perovskite solar cells,” *Nanomaterials*, vol. 9, no. 3, 2019.

[77] D. Huh, K. S. Oh, M. Kim, H. J. Choi, D. S. Kim, and H. Lee, “Selectively patterned TiO2 nanorods as electron transport pathway for high performance perovskite solar cells,” *Nano Res.*, vol. 12, no. 3, pp. 601–606, 2019.

[78] J. Choi, S. Song, M. T. Hörantner, H. J. Snaith, and T. Park, “Well-Defined Nanostructured, Single-Crystalline TiO_2 Electron Transport Layer for Efficient Planar Perovskite Solar Cells,” *ACS Nano*, vol. 10, no. 6, pp. 6029–6036, 2016.

[79] A. Alberti *et al.*, “Structural and Optical Behaviour of $MAPbI_3$ Layers in Nitrogen and Humid Air: (Hybrid perovskite stability can be improved?),” *IEEE 4th Int. Forum Res. Technol. Soc. Ind. RTSI 2018 - Proc.*, pp. 2–6, 2018.

[80] O. A. Lozhkina *et al.*, "Invalidity of Band-Gap Engineering Concept for Bi3+ Heterovalent Doping in CsPbBr3 Halide Perovskite," *J. Phys. Chem. Lett.*, vol. 9, no. 18, pp. 5408–5411, 2018.

[81] J. Wan *et al.*, "Hydrothermal etching treatment to rutile TiO_2 nanorod arrays for improving the efficiency of CdS-sensitized TiO_2 solar cells," *Nanoscale Res. Lett.*, vol. 11, no. 1, pp. 1–9, 2016.

[82] A. Priyadarshi *et al.*, "A large area (70 cm2) monolithic perovskite solar module with a high efficiency and stability," *Energy Environ. Sci.*, vol. 9, no. 12, pp. 3687–3692, 2016.

[83] L. L. Gao, C. X. Li, C. J. Li, and G. J. Yang, "Large-area high-efficiency perovskite solar cells based on perovskite films dried by the multi-flow air knife method in air," *J. Mater. Chem. A*, vol. 5, no. 4, pp. 1548–1557, 2017.

[84] B. S. Witkowski, "Applications of ZnO nanorods and nanowires — A review," *Acta Phys. Pol. A*, vol. 134, no. 6, pp. 1226–1246, 2018.

[85] M. S. Selim, A. M. Elseman, and Z. Hao, "ZnO Nanorods: An Advanced Cathode Buffer Layer for Inverted Perovskite Solar Cells," *ACS Appl. Energy Mater.*, 2020.

[86] Y. Zhang, M. K. Ram, E. K. Stefanakos, and D. Y. Goswami, "Synthesis, characterization, and applications of ZnO nanowires," *J. Nanomater.*, vol. 2012, 2012.

[87] Y. Xu *et al.*, "Preparation and photovoltaic properties of perovskite solar cell based on ZnO nanorod arrays," *Appl. Surf. Sci.*, vol. 388, no. 3, pp. 89–96, 2016.

[88] V. Siva *et al.*, "Mapping the structural, electrical, and optical properties of hydrothermally grown phosphorus-doped zno nanorods for optoelectronic device applications," *Nanoscale Res. Lett.*, vol. 14, 2019.

[89] M. B. Agarwal, M. Malaidurai, A. Sharma, and R. Thangavel, "Effect of Al doping on hydrothermal growth and physical properties of doped ZnO

nanoarrays for optoelectronic applications," *Mater. Today Proc.*, vol. 21, pp. 1781–1786, 2020.

[90] D. Y. Son, K. H. Bae, H. S. Kim, and N. G. Park, "Effects of seed layer on growth of ZnO nanorod and performance of perovskite solar cell," *J. Phys. Chem. C*, vol. 119, no. 19, pp. 10321–10328, 2015.

[91] K. Mahmood, B. S. Swain, and H. S. Jung, "Controlling the surface nanostructure of ZnO and Al-doped ZnO thin films using electrostatic spraying for their application in 12% efficient perovskite solar cells," *Nanoscale*, vol. 6, no. 15, pp. 9127–9138, 2014.

[92] X. Dong, H. Hu, B. Lin, J. Ding, and N. Yuan, "The effect of ALD-Zno layers on the formation of CH3NH3PbI3 with different perovskite precursors and sintering temperatures," *Chem. Commun.*, vol. 50, no. 92, pp. 14405–14408, 2014.

[93] Shirazi Narzieh, Dariani, Reza, and M. R. Toroghinejad, "Efficiency enhancement of hole-conductor-free perovskite solar cell based on ZnO nanostructure by Al doping in ZnO," *J. Alloys Compd.*, vol. 692, pp. 492–502, 2017.

[94] P. Sahoo, A. Sharma, and R. Thangavel, "Hydrothermal synthesis, structural and optical investigations of undoped and Mg doped ZnO nanorods," *AIP Conf. Proc.*, vol. 2100, no. April, 2019.

[95] P. Wang, J. Zhao, W. Liu, Z. Liu, L. Guan, and G. Cao, "Stabilization of organometal halide perovskite films by SnO2 coating with inactive surface hydroxyl groups on nanorods," *J. Power Sources*, no. 339, pp. 51–60, 2017.

[96] J. Zhang, E. J. Juárez-Pérez, I. Mora-Seró, B. Viana, and T. Pauporté, "Fast and low temperature growth of electron transport layers for efficient perovskite solar cells," *J. Mater. Chem. A*, vol. 3, no. 9, pp. 4909–4915, 2015.

[97] J. Zhang and T. Pauporté, "Effects of Oxide Contact Layer on the Preparation and Properties of $CH_3NH_3PbI_3$ for Perovskite Solar Cell Application," *J. Phys.*

Chem. C, vol. 119, no. 27, pp. 14919–14928, 2015.

[98] Z. Qiu *et al.*, “The Influence of Physical Properties of ZnO Films on the Efficiency of Planar ZnO/Perovskite/P3HT Solar Cell,” *J. Am. Ceram. Soc.*, vol. 100, no. 1, pp. 176–184, 2017.

[99] M. M. Tavakoli, R. Tavakoli, Z. Nourbakhsh, A. Waleed, U. S. Virk, and Z. Fan, “High Efficiency and Stable Perovskite Solar Cell Using ZnO/rGO QDs as an Electron Transfer Layer,” *Adv. Mater. Interfaces*, vol. 3, no. 11, pp. 1–10, 2016.

[100] F. J. Ramos *et al.*, “Perovskite solar cells based on nanocolumnar plasma-deposited ZnO thin films,” *ChemPhysChem*, vol. 15, no. 6, pp. 1148–1153, 2014.

[101] A. Dualeh, N. Tétreault, T. Moehl, P. Gao, M. K. Nazeeruddin, and M. Grätzel, “Effect of annealing temperature on film morphology of organic-inorganic hybrid pervoskite solid-state solar cells,” *Adv. Funct. Mater.*, vol. 24, no. 21, pp. 3250–3258, 2014.

[102] H. Zhou *et al.*, “Low-temperature processed and carbon-based ZnO/$CH_3NH_3PbI_3$/C planar heterojunction perovskite solar cells,” *J. Phys. Chem. C*, vol. 119, no. 9, pp. 4600–4605, 2015.

[103] J. You *et al.*, “Improved air stability of perovskite solar cells via solution-processed metal oxide transport layers,” *Nat. Nanotechnol.*, vol. 11, no. 1, pp. 75–81, 2016.

[104] M. H. Kumar, N. Yantara, S. Dharani, M. Graetzel, P. P. Boix, and N. Mathews, “Flexible, low-temperature, solution processed ZnO-based perovskite solid state solar cells,” *Chem. Commun.*, vol. 49, no. 94, pp. 11089–11091, 2013.

[105] K. H. Solangi, M. R. Islam, R. Saidur, N. A. Rahim, and H. Fayaz, “A review on global solar energy policy,” *Renew. Sustain. Energy Rev.*, vol. 15, pp. 2149–2163, 2011.

[106] A. Mhamdi, W. Boukhili, M. Raissi, M. Mahdouani, L. Vignau, and R. Bourguiga, “Simulation and optimization of the performance of organic

photovoltaic cells based on capped copolymers for bulk heterojunctions," *Superlattices and Microstructures*, vol. 96. pp. 241–252, 2016.

[107] Z. Li *et al.*, "Scalable fabrication of perovskite solar cells," *Nat. Rev. Mater.*, vol. 3, pp. 1–20, 2018.

[108] C. Zuo, H. J. Bolink, H. Han, J. Huang, D. Cahen, and L. Ding, "Advances in perovskite solar cells," *Adv. Sci.*, vol. 3, no. 7, pp. 1–16, 2016.

[109] A. Hima, N. Lakhdar, B. Benhaoua, A. Saadoune, I. Kemerchou, and F. Rogti, "An optimized perovskite solar cell designs for high conversion efficiency," *Superlattices and Microstructures*, vol. 129. pp. 240–246, 2019.

[110] W. J. Yin, T. Shi, and Y. Yan, "Unique properties of halide perovskites as possible origins of the superior solar cell performance," *Adv. Mater.*, vol. 26, no. 27, pp. 4653–4658, 2014.

[111] V. D'Innocenzo *et al.*, "Excitons versus free charges in organo-lead tri-halide perovskites," *Nat. Commun.*, vol. 5, pp. 1–6, 2014.

[112] A. M. Askar and K. Shankar, "Exciton Binding Energy in Organic–Inorganic Tri-Halide Perovskites," *J. Nanosci. Nanotechnol.*, vol. 16, no. June, pp. 1–12, 2016.

[113] Y. Wang, M. Zhong, and L. Chai, "Effects of the concentration of PbI2 and CH3NH3I on the perovskite films and the performance of perovskite solar cells based on ZnO-TiO2 nanorod arrays," *Superlattices and Microstructures*, vol. 123. pp. 189–200, 2018.

[114] R. K. Upadhyay, S. Member, A. P. Singh, and D. Upadhyay, "BiFeO3 /$CH_3NH_3PbI_3$ Perovskite Heterojunction Based Near-Infrared Photodetector," *IEEE Electron Device Lett.*, vol. 40, no. 12, pp. 1961–1964, 2019.

[115] R. K. Upadhyay, A. P. Singh, D. Upadhyay, S. Ratan, C. Kumar, and S. Jit, "High-Performance Photodetector Based on Organic – Inorganic Perovskite," *IEEE Photonics Technol. Lett.*, vol. 31, no. 14, pp. 1151–1154, 2019.

[116] D. K. Jarwal *et al.*, "Efficiency Improvement of TiO_2 Nanorods Electron Transport Layer Based Perovskite Solar Cells by Solvothermal Etching," *IEEE J. Photovoltaics*, vol. PP, pp. 1–9, 2019.

[117] K. G. Stamplecoskie, J. S. Manser, and P. V. Kamat, "Dual nature of the excited state in organic-inorganic lead halide perovskites," *Energy Environ. Sci.*, vol. 8, no. 1, pp. 208–215, 2015.

[118] A. Kumar, S. Ratan, D. K. Jarwal, A. K. Mishra, and C. Kumar, "Effect of PQT-12 interface layer on the performance of PCDTBT : PCBM bulk heterojunction solar cells Effect of PQT-12 interface layer on the performance of PCDTBT : PCBM bulk heterojunction solar cells," *Mater. Res. Express*, vol. 6, no. 115514, pp. 1–9, 2019.

[119] U. Mandadapu, S. V. Vedanayakam, and K. Thyagarajan, "Simulation and Analysis of Lead based Perovskite Solar Cell using SCAPS-1D," *Indian J. Sci. Technol.*, vol. 10, no. 11, pp. 1–8, 2017.

[120] X. Sun, R. Asadpour, W. Nie, A. D. Mohite, and M. A. Alam, "A Physics-Based Analytical Model for Perovskite Solar Cells," *IEEE J. Photovoltaics*, vol. 5, no. 5, pp. 1389–1394, 2015.

[121] X. Wei *et al.*, "Numerical simulation and experimental validation of inverted planar perovskite solar cells based on NiOx hole transport layer," *Superlattices Microstruct.*, vol. 112, pp. 383–393, 2017.

[122] T. Minemoto and M. Murata, "Device modeling of perovskite solar cells based on structural similarity with thin film inorganic semiconductor solar cells," *J. Appl. Phys.*, vol. 116, no. 054505, pp. 1–5, 2014.

[123] A. Mebadi, M. Houshmand, M. H. Zandi, and N. E. Gorji, "Numerical Analysis of TiO_2/Cu_2ZnSnS_4 Nanostructured PV Using SCAPS-1D," *Nano Hybrids*, vol. 8, pp. 27–38, 2014.

[124] S.Farzad and N.Mina, "Optimization of Structure of Solar Cells Based on Lead

Perovskites (CH3NH3PbX3, X: I, Br) Via Numerical Simulation," *J. Sol. Energy Res.*, vol. 24, no. 1, pp. 315–321, 2017.

[125] D. B. Khadka, Y. Shirai, M. Yanagida, J. W. Ryan, and K. Miyano, "Exploring the effects of interfacial carrier transport layers on device performance and optoelectronic properties of planar perovskite solar cells," *J. Mater. Chem. C*, vol. 5, no. 34, pp. 8819–8827, 2017.

[126] F. Anwar, R. Mahbub, S. S. Satter, and S. M. Ullah, "Effect of Different HTM Layers and Electrical Parameters on ZnO Nanorod-Based Lead-Free Perovskite Solar Cell for High-Efficiency Performance," *Int. J. Photoenergy*, vol. 2017, pp. 1–9, 2017.

[127] L. Lin, L. Jiang, Y. Qiu, and Y. Yu, "Modeling and analysis of HTM-free perovskite solar cells based on ZnO electron transport layer," *Superlattices and Microstructures*, vol. 104. pp. 167–177, 2017.

[128] M. Sreemany and S. Sen, "A simple spectrophotometric method for determination of the optical constant and band gap energy of multiple layer TiO2 thin films," *Mater. Chem. Phys.*, vol. 83, pp. 169–177, 2004.

[129] O. A. Jaramillo-Quintero *et al.*, "Recombination reduction on lead halide perovskite solar cells based on low temperature synthesized hierarchical TiO2 nanorods," *Nanoscale*, vol. 8, no. 12, pp. 6271–6277, 2016.

[130] U. K. Thakur, A. M. Askar, R. Kisslinger, B. D. Wiltshire, P. Kar, and K. Shankar, "Halide perovskite solar cells using monocrystalline TiO2 nanorod arrays as electron transport layers: Impact of nanorod morphology," *Nanotechnology*, vol. 28, no. 27, 2017.

[131] C. Liu *et al.*, "Investigation of high performance TiO2 nanorod array perovskite solar cells," *J. Mater. Chem. A*, vol. 5, no. 30, pp. 15970–15980, 2017.

[132] G. Niu, X. Guo, and L. Wang, "Review of recent progress in chemical stability of perovskite solar cells," *J. Mater. Chem. A*, vol. 3, pp. 8970–8980, 2015.

[133] S. M. H. Al-Jawad, O. N. Salman, and N. A. Yousif, “Influence of growth time on structural optical and electrical properties of TiO2 nanorod arraya deposited by hydrothermal method,” *Surf. Rev. Lett.*, vol. 26, no. 3, pp. 1–9, 2019.

[134] P. Zhao *et al.*, “Device simulation of inverted CH 3 NH 3 PbI 3−x Cl x perovskite solar cells based on PCBM electron transport layer and NiO hole transport layer,” *Sol. Energy*, vol. 169, no. April, pp. 11–18, 2018.

[135] A. Fakharuddin, F. Di Giacomo, I. Ahmed, Q. Wali, T. M. Brown, and R. Jose, “Role of morphology and crystallinity of nanorod and planar electron transport layers on the performance and long term durability of perovskite solar cells,” *J. Power Sources*, vol. 283, pp. 61–67, 2015.

[136] J. Joo *et al.*, “Large-scale synthesis of TiO2 nanorods via nonhydrolytic sol-gel ester elimination reaction and their application to photocatalytic inactivation of E. coli,” *J. Phys. Chem. B*, vol. 109, no. 32, pp. 15297–15302, 2005.

[137] M. Y. Liao, L. Fang, C. L. Xu, F. Wu, Q. L. Huang, and M. Saleem, “Materials Science in Semiconductor Processing Effect of seed layer on the growth of rutile TiO 2 nanorod arrays and their performance in dye-sensitized solar cells,” vol. 24, pp. 1–8, 2014.

[138] J. Qin, Z. Zhang, W. Shi, Y. Liu, H. Gao, and Y. Mao, “The optimum titanium precursor of fabricating TiO2 compact layer for perovskite solar cells,” *Nanoscale Res. Lett.*, vol. 1, no. 12, p. 640, 2017.

[139] G. Rawat, D. Somvanshi, H. Kumar, Y. Kumar, C. Kumar, and S. Jit, “Ultraviolet Detection Properties of p-Si/n-TiO2 Heterojunction Photodiodes Grown by Electron-Beam Evaporation and Sol–Gel Methods: A Comparative Study,” *IEEE Trans. Nanotechnol.*, vol. 15, no. 2, pp. 193–200, 2016.

[140] J. Wan *et al.*, “Hydrothermal Etching Treatment to Rutile TiO2 Nanorod Arrays for Improving the Efficiency of CdS-Sensitized TiO2 Solar Cells,” *Nanoscale Res. Lett.*, vol. 10, no. 1, pp. 1–9, 2016.

[141] B. El Cohen and L. Etgar, “Parameters that control and influence the organo-metal halide perovskite crystallization and morphology,” *Front. Optoelectron.*, vol. 9, no. 1, pp. 44–52, 2016.

[142] M. M. Lee, J. Teuscher, T. Miyasaka, T. N. Murakami, and H. J. Snaith, “Efficient Hybrid Solar Cells Based on Meso-Superstructured Organometal Halide Perovskites,” no. October, pp. 1–6, 2012.

[143] M. Sreemany and S. Sen, “A simple spectrophotometric method for determination of the optical constants and band gap energy of multiple layer TiO2 thin films,” *Mater. Chem. Phys.*, vol. 83, no. 1, pp. 169–177, 2004.

[144] M. Kim, B. Kim, and J. Kim, “Effective Variables To Control the Fill Factor of Organic Photovoltaic Cells,” vol. 1, no. 6, pp. 1–6, 2009.

[145] H. Kumar *et al.*, “Heating Effects of Colloidal ZnO Quantum Dots (QDs) on ZnO QD/CdSe QD/MoOx Photodetectors,” *IEEE Trans. Nanotechnol.*, vol. 16, no. 6, pp. 1073–1080, Nov. 2017.

[146] H. Kim *et al.*, “High Efficiency Solid-State Sensitized Solar Cell-Based on Submicrometer Rutile TiO2 Nanorod and CH3NH3PbI3 Perovskite Sensitizer,” *Nano Lett.*, vol. 13, no. 6, p. 2412−2417, 2013.

[147] C. S. Shim, H. K. Park, J. Heo, P. S. Patil, and C. K. Hong, “Ultrathin Atomic Layer Deposited TiO2 for Surface Passivation of Hydrothermally Grown 1D TiO2 Nanorod Arrays for Efficient Solid- State Perovskite Solar Cells,” *Chem. Mater.*, vol. 27, p. 1541−1551, 2015.

[148] G. S. Han *et al.*, “Reduced Graphene Oxide / Mesoporous TiO2 Nanocomposite Based Perovskite Solar Cells,” *ACS Appl. Mater. Interfaces*, vol. 7, p. 23521−23526, 2015.

[149] J. Hu *et al.*, “TiO_2 nanotube/TiO_2 nanoparticle hybrid photoanode for hole-conductor-free perovskite solar cells based on carbon counter electrodes,” *Opt. Mater. Express*, vol. 7, no. 9, p. 3322, 2017.

[150] X. Sun *et al.*, “Influence of the Porosity of the TiO2 Film on the Performance of the Perovskite Solar Cell,” *Int. J. Photoenergy*, vol. 2017, p. 4935265, 2017.

[151] L. Li, C. Shi, X. Deng, Y. Wang, and L. Ni, “High-crystallinity and large-grain CH3NH3PbI3 thin films for efficient TiO2 nanorod array perovskite solar cells,” *Micro Nano Lett.*, vol. 13, no. 1, pp. 131–134, 2017.

[152] W. Ye, J. Xiang, F. Huang, and D. Zhong, “Towards large-area perovskite solar cells : the influence of compact and mesoporous TiO2 electron transport layers,” *Mater. Res. Express*, vol. 5, p. 085506, 2018.

[153] A. Imanah, P. Ekanayake, A. Wakamiya, H. Nakajima, and ming chee lim, “Enhanced performance of CH3NH3PbI3-based perovskite solar cells by tuning the electrical and structural properties of mesoporous TiO2 layer via Al and Mg doping,” *Sol. Energy*, vol. 177, pp. 374–381, 2019.

[154] D. Y. Son, J. H. Im, H. S. Kim, and N. G. Park, “11% efficient perovskite solar cell based on ZnO nanorods: An effective charge collection system,” *J. Phys. Chem. C*, vol. 118, no. 30, pp. 16567–16573, 2014.

[155] A. Mahesh, “Photovoltaic performance of ZnO nanosheets solar cell sensitized with beta-substituted porphyrin,” *J. Nanomater.*, vol. 2011, no. 9, pp. 1787–1793, 2011.

[156] V. Consonni, J. Briscoe, E. Kärber, X. Li, and T. Cossuet, “ZnO nanowires for solar cells: A comprehensive review,” *Nanotechnology*, vol. 30, no. 36, 2019.

[157] E. Peksu and H. Karaagac, “Synthesis of ZnO Nanowires and Their Photovoltaic Application: ZnO Nanowires/AgGaSeThin Film Core-Shell Solar Cell,” *J. Nanomater.*, vol. 2015, 2015.

[158] L. Li *et al.*, “High-yield synthesis of single-crystalline zinc oxide nanobelts and their applications in novel Schottky solar cells,” *Chem. Commun.*, vol. 47, no. 29, pp. 8247–8249, 2011.

[159] D. Cao, S. Gong, X. Shu, D. Zhu, and S. Liang, “Preparation of ZnO

Nanoparticles with High Dispersibility Based on Oriented Attachment (OA) Process,” *Nanoscale Res. Lett.*, vol. 14, 2019.

[160] H. R. Ghorbani, F. P. Mehr, H. Pazoki, and B. M. Rahmani, “Synthesis of ZnO nanoparticles by precipitation method,” *Orient. J. Chem.*, vol. 31, no. 2, pp. 1219–1221, 2015.

[161] Y. Kumar *et al.*, “Colloidal ZnO quantum dots based spectrum selective ultraviolet photodetectors,” *IEEE Photonics Technol. Lett.*, vol. 29, no. 4, pp. 361–364, 2017.

[162] Z. Liu, J. Ya, and E. Lei, “Effects of substrates and seed layers on solution growing ZnO nanorods,” *J. Solid State Electrochem.*, vol. 14, no. 6, pp. 957–963, 2010.

[163] M. Sreemany and S. Sen, “A simple spectrophotometric method for determination of the optical constants and band gap energy of multiple layer TiO2 thin films,” *2004*, vol. 83, pp. 169–177.

[164] H. Kumar *et al.*, “Heating Effects of Colloidal ZnO Quantum Dots Heating Effects of Colloidal ZnO Quantum Dots,” *Ieee Trans. Nanotechnol.*, vol. 16, no. 6, pp. 1073–1080, 2017.

[165] G. Rawat, D. Somvanshi, Y. Kumar, H. Kumar, C. Kumar, and S. Jit, “Electrical and Ultraviolet-A Detection Properties of E-Beam Evaporated n-TiO2 Capped p-Si Nanowires Heterojunction Photodiodes,” *IEEE Trans. Nanotechnol.*, vol. 16, no. 1, pp. 49–57, 2017.

[166] T. H. Schloemer, J. A. Christians, J. M. Luther, and A. Sellinger, “Doping strategies for small molecule organic hole-transport materials: impacts on perovskite solar cell performance and stability,” *Chem. Sci.*, vol. 10, no. 7, pp. 1904–1935, 2019.

[167] S. R. Meher, L. Balakrishnan, and Z. C. Alex, “Analysis of Cu2ZnSnS4/CdS based photovoltaic cell: A numerical simulation approach,” *Superlattices*

Microstruct., vol. 100, pp. 703–722, 2016.

[168] X. Deng, Y. Wang, Z. Cui, L. Li, and C. Shi, “Y-doping TiO2 nanorod arrays for efficient perovskite solar cells,” *Superlattices Microstruct.*, vol. 117, pp. 283–287, 2018.

[169] H. Xi *et al.*, “Performance Enhancement of Planar Heterojunction Perovskite Solar Cells through Tuning the Doping Properties of Hole-Transporting Materials,” *ACS Omega*, vol. 2, no. 1, pp. 326–336, 2017.

[170] D. K. Jarwal *et al.*, “Fabrication and TCAD simulation of TiO2 nanorods electron transport layer based perovskite solar cells,” *Superlattices Microstruct.*, vol. 140, p. 106463, 2020.

[171] H. Kumar *et al.*, “Heating Effects of Colloidal ZnO Quantum Dots (QDs) on ZnO QD/CdSe QD/MoOx Photodetectors,” *IEEE Trans. Nanotechnol.*, vol. 16, no. 6, pp. 1073–1080, 2017.

[172] S. Wang *et al.*, “Unveiling the Role of tBP-LiTFSI Complexes in Perovskite Solar Cells,” *J. Am. Chem. Soc.*, vol. 140, no. 48, pp. 16720–16730, 2018.

[173] A. Kumar *et al.*, “Effect of PQT-12 interface layer on the performance of PCDTBT: PCBM bulk heterojunction solar cells,” *Mater. Res. Express*, vol. 6, no. 11, 2019.

[174] M. Fathi, M. Abderrezek, F. Djahli, and M. Ayad, “Study of Thin Film Solar Cells in High Temperature Condition,” *Energy Procedia*, vol. 74, pp. 1410–1417, 2015.

[175] M. A. Cappelletti, G. A. Casas, A. P. Cédola, E. L. Peltzer y Blancá, and B. Marí Soucase, “Study of the reverse saturation current and series resistance of p-p-n perovskite solar cells using the single and double-diode models,” *Superlattices and Microstructures*, vol. 123. pp. 338–348, 2018.

[176] E. Karimi and S. M. B. Ghorashi, “Investigation of the influence of different hole-transporting materials on the performance of perovskite solar cells,” *Optik*,

vol. 130. pp. 650–658, 2017.

[177] W. J. Chi, P. P. Sun, and Z. S. Li, "How to regulate energy levels and hole mobility of spiro-type hole transport materials in perovskite solar cells," *Phys. Chem. Chem. Phys.*, vol. 18, no. 39, pp. 27073–27077, 2016.

[178] H. Dixit, D. Punetha, and S. K. Pandey, "Improvement in performance of lead free inverted perovskite solar cell by optimization of solar parameters," *Optik (Stuttg).*, vol. 179, no. October 2018, pp. 969–976, 2019.

[179] N. Sakai, T. Miyasaka, and T. N. Murakami, "Efficiency enhancement of ZnO-based dye-sensitized solar cells by low-temperature TiCl4 treatment and dye optimization," *J. Phys. Chem. C*, vol. 117, no. 21, pp. 10949–10956, 2013.

[180] J. A. Christians, R. C. M. Fung, and P. V. Kamat, "An inorganic hole conductor for Organo-lead halide perovskite solar cells. improved hole conductivity with copper iodide," *J. Am. Chem. Soc.*, vol. 136, no. 2, pp. 758–764, 2014.

[181] S. K. Dwivedi *et al.*, "Fabrication and properties of P3HT: PCBM/Cu2SnSe3 (CTSe)nanocrystals based inverted hybrid solar cells," *Sol. Energy*, vol. 187, no. May, pp. 167–174, 2019.

[182] Y. Li *et al.*, "Efficient inorganic solid solar cells composed of perovskite and PbS quantum dots," *Nanoscale*, vol. 7, no. 21, pp. 9902–9907, 2015.

[183] C. Kumar, G. Rawat, H. Kumar, Y. Kumar, R. Prakash, and S. Jit, "Electrical and Optical Characteristics of PQT-12-Based Organic TFTs Fabricated by Floating-Film Transfer Method," *IEEE Trans. Nanotechnol.*, vol. 17, no. 6, pp. 1111–1117, 2018.

AUTHOR’S RELEVANT PUBLICATIONS

Journals:

1. **Deepak Kumar Jarwal**., Amit Kumar, Ashwini Kumar Mishra, Smrity Ratan, Kumar, C., Upadhyay, D., Mukherjee, B. and Jit, S. Efficiency Improvement of TiO_2 Nanorods Electron Transport Layer Based Perovskite Solar Cells by Solvothermal Etching. IEEE Journal of Photovoltaics, vol. 9(6), pp.1699-1707, 2019.
2. **Deepak Kumar Jarwal**, Ashwini Kumar Mishra, Amit Kumar, Smrity Ratan, Abhinav Pratap Singh, Chandan Kumar, Bratindranath Mukherjee, and Satyabrata Jit, “Fabrication and TCAD Simulation of TiO_2 Nanorods Electron Transport Layer Based Perovskite Solar Cells,” Superlattice and Microstructure, vol. 140, pp. 106463, 2020.
3. **Deepak Kumar Jarwal**, Amit Kumar, Ashwini Kumar Mishra, Smrity Ratan, Rishibrind Kumar Upadhyay, Chandan Kumar, Bratindranath Mukherjee, and Satyabrata Jit, “ Fabrication and TCAD validation of ambient air-processed ZnO NRs/$CH_3NH_3PbI_3$/Spiro-OMeTAD solar cells,” Superlattice and Microstructure, vol. 143, pp. 106540, 2020.

Conferences:

1. **Deepak Kumar Jarwal**, Ashwini Kumar Mishra, Amit Kumar, Smrity Rtan, Manas Ranjan Tripathy, Nitin Kumar Suyan, Bratindranath Mukherjee and Satyabrata Jit’ “Performance Analysis and Experimental Validation of ZnO Nanorods ETL based Hybrid Perovskite Solar Cell,” ICONRER-2019, Jaipur, India, 2019.
2. **Deepak Kumar Jarwal**, Ashwini Kumar Mishra, Amit Kumar, Smrity Rtan, Rishibrind Upadyay, Bratindranath Mukherjee and Satyabrata Jit’ “Thickness

variation effect of different layer of perovskire solar cell on the performance of solar cell" ICONN-2021, Chennai, India, 2021.